



UCGE Reports

Number 20280

Department of Geomatics Engineering

**Parameterization of GPS L1 Multipath Using a Dual
Polarized RHCP/LHCP Antenna**

(URL: <http://www.geomatics.ucalgary.ca/links/GradTheses.html>)

by

Ashkan Izadpanah

January 2009

SCHULICH
School of Engineering



UNIVERSITY OF CALGARY

Parameterization of GPS L1 Multipath Using a Dual Polarized
RHCP/LHCP Antenna

by

Ashkan Izadpanah

A THESIS

SUBMITTED TO THE FACULTY OF GRADUATE STUDIES
IN PARTIAL FULFILMENT OF THE REQUIREMENTS FOR THE
DEGREE OF MASTER OF SCIENCE

DEPARTMENT OF GEOMATICS ENGINEERING

CALGARY, ALBERTA

January, 2009

© Ashkan Izadpanah 2009

Abstract

Multipath is a phenomenon where different replicas of the transmitted signal arrive at the receiver with different delays relative to the Line-Of-Sight (LOS) signal causing a bias in the estimate of the received signal's code phase. The GPS signal polarization may change upon reflection from right hand circular polarization (RHCP) to left hand circular polarization (LHCP). Since the characteristics of the signal such as amplitude, phase and polarization depend on the reflector type, the reflected GPS signal (multipath) gives valuable information about the characteristics of the multipath environment.

In this thesis, different multipath parameterization techniques will be presented and investigated using real signals. A multipath parameterization method based on the Extended Kalman filter (EKF) is developed in the tracking loops and then verified in simulated and actual outdoor multipath environments. The tracking loop in this algorithm has a multi-correlator structure. A specific real data setup consisting of a dual polarized RHCP/LHCP antenna is also proposed for characterizing and analyzing the multipath environment. Signal to multipath ratio (SMR) values obtained from the Kalman multipath (KMP) algorithm along with fading patterns, autocorrelation functions, K factors and pseudorange multipath errors derived from dual polarization multipath parameterization techniques are measured and estimated for the signals received by both RHCP and LHCP antennas. The multipath parameters extracted from these two data sets are then used for studying the effect of antenna polarization on the level of multipath power absorption in the received signal and consequently on position performance.

Acknowledgements

My sincerest thanks are due to my supervisors, Professor Gerard Lachapelle and Dr. Cillian O'Driscoll, for their tenacious dedication and support offered during my graduate studies, research and dissertation work. Their wide knowledge and logical way of thinking have been of great value for me. Their understanding, encouraging and personal guidance have provided a good basis for the present thesis.

Professor Ron Johnston of the Department of Electrical and Computer Engineering is also acknowledged for his useful comments on the polarization analyses.

I greatly appreciate research engineers and my colleagues in the PLAN group who helped me to acquire this professional experience. I owe special thanks to Professor Mark Petovello, Dr Surendran K. Shanmugam and Dr. Daniele Borio for their efforts and patience to make technical comments on my research work. I also thank all my colleagues in the PLAN group, specifically Pejman Kazemi, Ali Broumandan, Saloome Abbasian Nik, Ahmadreza Moghaddam, Tao Lin, Jared Bancroft, Richard Ong, Aiden Morrison and Debu Sun, for their valuable assistance.

My deepest gratitude goes to my family for their unflagging love and support throughout my life; this dissertation would have been simply impossible without them. Their continuous support gave me the strength, motivation, and willingness to continue my research.

Finally, I would like to thank everybody who was important to the successful realization of thesis, as well as expressing my apology that I could not mention personally one by one.

Table of Contents

APPROVAL PAGE.....	III
ABSTRACT	III
ACKNOWLEDGEMENTS.....	IV
TABLE OF CONTENTS.....	VI
LIST OF TABLES	IX
LIST OF FIGURES	IX
LIST OF SYMBOLS.....	XIII
LIST OF ABBREVIATIONS.....	XVI
CHAPTER ONE: INTRODUCTION.....	1
1.1 BACKGROUND	1
<i>1.1.1 GPS error sources</i>	<i>1</i>
<i>1.1.2 Multipath signal polarization</i>	<i>2</i>
1.2 MULTIPATH PARAMETERIZATION TECHNIQUES OVERVIEW	3
1.3 RESEARCH OVERVIEW	5
<i>1.3.1 Motivation.....</i>	<i>5</i>
<i>1.3.2 Objectives and Intended contributions.....</i>	<i>5</i>
1.4 THESIS OUTLINE	9
CHAPTER TWO: BACKGROUND.....	11
2.1 SIGNAL POLARIZATION	11
2.2 REFLECTED GPS SIGNAL POLARIZATION ANALYSES	14
<i>2.2.1 Decomposition of elliptical polarization into right and left handed circular polarization.....</i>	<i>16</i>

2.2.2 Signal propagation analysis in a simple multipath scenario	19
2.3 MULTIPATH SIGNAL RECEPTION BY RHCP AND LHCP ANTENNAS.....	21
2.3.1 Total received signal power at RHCP and LHCP antennas.....	24
2.4 RHCP/LHCP DATA ANALYSES ALONG THE SIGNAL PROCESSING CHAIN	25
2.5 CORRELATOR OUTPUTS FOR THE RHCP DATA.....	29
2.5.1 Correlator outputs for the general multipath scenario.....	31
CHAPTER THREE: REVIEW OF TECHNIQUES USED.....	35
3.1 STANDARD TRACKING LOOP STRUCTURE.....	35
3.2 KALMAN FILTER THEORY	37
3.2.1 Extended Kalman Filter (EKF).....	40
3.2.2 Innovation statistics	43
3.3 KPLL STRUCTURE.....	43
3.3.1 KPLL implementation.....	45
3.4 KPDLL (KLOS) STRUCTURE	50
3.4.1 KLOS implementation.....	53
3.4.2 KLOS verification using the real data	56
3.5 RECEIVED GPS SIGNAL MODELING IN A SPECULAR MULTIPATH ENVIRONMENT	62
3.6 RAKE-LIKE MULTI-CORRELATOR STRUCTURE (KMP STRUCTURE).....	64
3.6.1 KMP implementation	65
3.7 PRIMARY-SECONDARY STRUCTURE FOR RHCP/LHCP DATA	68
3.7.1 Primary-secondary implementation in the GSNRx™ software.....	69
3.7.2 Verifying the primary-secondary structure with real data.....	71
3.8 SUMMARY	75
CHAPTER FOUR: ANALYSIS OF THE KMP TECHNIQUE	76
4.1 KMP VERIFICATION USING A GPS HARDWARE SIMULATOR	76
4.1.1 First scenario.....	77

4.1.2 <i>Second scenario</i>	83
4.1.3 <i>Third scenario</i>	89
4.2 REAL MULTIPATH ENVIRONMENT	93
4.2.1 <i>Data collection scheme</i>	95
4.2.2 <i>KMP analysis</i>	98
4.3 SUMMARY	108
CHAPTER FIVE: DUAL POLARIZATION TECHNIQUES ANALYSES.....	109
5.1 AUTOCORRELATION FUNCTION ANALYSIS	109
5.1.1 <i>PRN 31 RHCP/LHCP Autocorrelation functions</i>	111
5.1.2 <i>PRN 14 RHCP/LHCP Autocorrelation functions</i>	113
5.2 POWER DISTRIBUTION ANALYSIS	115
5.2.1 <i>K factor concept</i>	115
5.2.2 <i>K factor analysis</i>	118
5.3 PSEUDORANGE MULTIPATH	122
5.4 U-BLOX RECEIVER ANALYSES.....	125
5.4.1 <i>Position solutions for the RHCP and LHCP antennas</i>	131
5.5 SUMMARY	135
CHAPTER SIX: CONCLUSIONS AND RECOMMENDATIONS	136
6.1 CONCLUSIONS	136
6.2 RECOMMENDATIONS FOR FUTURE WORK.....	139
REFERENCES	141

List of Tables

Table 3.1: Phase bias between primary and secondary channels.....	74
Table 4.1: SMR estimate statistics for the first scenario	79
Table 4.2: Relative code delay estimates statistics for the first scenario.....	80
Table 4.3: Initial values for the error standard deviations	81
Table 4.4: SMR statistics for the second scenario	86
Table 4.5: Relative code delay statistics for the second scenario	87
Table 4.6 : SMR statistics for the third scenario.....	91
Table 4.7: Relative code delay statistics for the third scenario.....	93
Table 5.1: RHCP and LHCP K factor for PRN 14 and 31	121
Table 5.2: RHCP/LHCP absolute maximum multipath errors for PRN 14 and 31	125
Table 5.3: RHCP and LHCP mean absolute multipath errors (m) for PRN 14 and 31 ..	125
Table 5.4: RMS position errors for the RHCP and LHCP antennas.....	134

List of Figures

Figure 2.1 : E vectors in a) linear b) circular c) elliptical polarization.....	12
Figure 2.2 : Incoming and reflected signals.....	15
Figure 2.3: Reflected signal polarization (Yang & Porter 2005b).....	16
Figure 2.4: RHCP (grey) and LHCP (blue) E vectors	18
Figure 2.5: Resulting elliptical polarization.....	18
Figure 2.6: Multipath scenario.....	19

Figure 2.7: RHCP antenna power patterns for RHCP and LHCP signals (Yang & Porter 2005b)	21
Figure 2.8: Multipath scenario	22
Figure 2.9: Multipath scenario	26
Figure 2.10: Correlation and accumulation process	30
Figure 3.1: Standard carrier tracking loop	37
Figure 3.2: Standard code tracking loop	37
Figure 3.3: KPLL carrier tracking loop structure	45
Figure 3.4: KPDLL (KLOS) code and carrier tracking loop structure	51
Figure 3.5: I and Q values in the KLOS loop structure	57
Figure 3.6: I and Q distributions in the KLOS loop structure	58
Figure 3.7: Kalman gain for PRN 07 amplitude estimate	59
Figure 3.8: Amplitude estimation error variance	60
Figure 3.9: 4 Kalman states estimation error variance	61
Figure 3.10: Multi-correlator with EKF structure	64
Figure 3.11: Primary-secondary structure	69
Figure 3.12: Primary-secondary implementation scheme in the GSNRx™ software	71
Figure 3.13: Data collection scheme for verifying the primary-secondary structure	72
Figure 3.14: Primary and secondary correlator outputs (First trial)	73
Figure 3.15: Primary and secondary correlator outputs (Second trial)	73
Figure 4.1: Data collection scheme	76
Figure 4.2: Correlator spacing	77
Figure 4.3: LOS and Multipath amplitude for the first scenario	78
Figure 4.4: SMR for the first scenario	79
Figure 4.5: Multipath relative code delay (chips) for the first scenario	80

Figure 4.6: Estimated LOS and multipath amplitude error standard deviations.....	82
Figure 4.7: Estimated multipath relative code delay error standard deviations.....	82
Figure 4.8: LOS and Multipath amplitude for the second scenario	84
Figure 4.9: SMR for the second scenario.....	85
Figure 4.10: Multipath relative code delay (chips) for the second scenario	87
Figure 4.11: Estimated LOS and multipath estimate error standard deviations	88
Figure 4.12: Estimated multipath relative code delay estimate standard deviations	89
Figure 4.13: LOS and Multipath amplitude for the third scenario	90
Figure 4.14: SMR for the third scenario	91
Figure 4.15: Multipath relative code delay (chips) for the third scenario	93
Figure 4.16: Real multipath environment schematic	94
Figure 4.17: Real multipath environment (west and south view).....	94
Figure 4.18: Real multipath environment (east view)	95
Figure 4.19: Real scenario data collection scheme.....	96
Figure 4.20: Real scenario data collection setup	97
Figure 4.21: GPS constellation observed by U-blox receiver.....	98
Figure 4.22: PRN 31's LOS and multipath amplitude for real data scenario	100
Figure 4.23: PRN 31's multipath relative code delay (chips) for real data scenario	100
Figure 4.24: PRN 31's multipath amplitude and relative code delay normalized cross correlation function	101
Figure 4.25: PRN 14's LOS and multipath amplitude for real data scenario	104
Figure 4.26: PRN 14's multipath relative code delay (chips) for real data scenario	104
Figure 4.27: PRN 14's multipath amplitude and relative code delay normalized cross correlation function	105
Figure 4.28: RHCP C/N_0 values for PRN 14 and 31	107

Figure 4.29: PRN 14 and 31 estimated SMR values for the RHCP antenna	107
Figure 4.30: PRN 14 and 31 multipath pseudorange errors for the RHCP antenna	108
Figure 5.1: Ideal autocorrelation function	110
Figure 5.2: PRN 31 Normalized autocorrelation functions for RHCP and LHCP data at time 11:13:06 (t1)	112
Figure 5.3: PRN 31 Normalized autocorrelation functions for RHCP and LHCP data at time 11:13:31(t2)	112
Figure 5.4: C/No values for PRN 31 received by RHCP and LHCP antennas.....	113
Figure 5.5: PRN 14 Normalized autocorrelation functions for RHCP and LHCP data at time 11:13:06(t1).....	114
Figure 5.6: PRN 14 Normalized autocorrelation functions for RHCP and LHCP data at time 11:14:23(t2).....	114
Figure 5.7: C/No values for PRN 14 received by RHCP and LHCP antennas.....	115
Figure 5.8: Rician distribution (constant sigma).....	117
Figure 5.9: Rician distribution (constant ν)	117
Figure 5.10: PRN 31 power distribution and corresponding Rician distribution for RHCP antenna.....	119
Figure 5.11: PRN 31 power distribution and its corresponding Rician distribution for LHCP antenna.....	120
Figure 5.12: PRN 14 power distribution and corresponding Rician distribution for RHCP antenna.....	121
Figure 5.13: PRN 14 power distribution and corresponding Rician distribution for LHCP antenna.....	122
Figure 5.14: PRN 31 multipath errors for RHCP and LHCP antennas	123
Figure 5.15: PRN 14 multipath errors for RHCP and LHCP antennas	124
Figure 5.16: PRN 14 and PRN 31 absolute multipath error values for the RHCP and LHCP antenna.....	124
Figure 5.17: GPS satellite geometry observed by the RHCP antenna.....	127

Figure 5.18: GPS satellite geometry observed by the LHCP antenna	127
Figure 5.19: RHCP and LHCP C/No levels for PRN 12	129
Figure 5.20: RHCP and LHCP C/No levels for PRN 32	130
Figure 5.21: RHCP and LHCP C/No levels for PRN 31	130
Figure 5.22: DOP values for the RHCP and LHCP antennas	132
Figure 5.23: RHCP antenna horizontal position errors	133
Figure 5.24: LHCP antenna horizontal position errors	133

List of Symbols

E	Electric field intensity vector
H	Magnetic field intensity vector
$\mathbf{E}_h(z)$	Horizontal electric vector
$\mathbf{E}_v(z)$	Vertical electric vector
$\mathbf{E}_{rhcp}(z)$	RHCP electric vector
$\mathbf{E}_{lhcp}(z)$	LHCP electric vector
θ_g	Grazing angle
Ψ_B	Brewster angle
θ_{LOS}	LOS angle
θ_{MP}	Multipath angle
MP _{EP}	Elliptically polarized reflected multipath signal
Γ	Reflection coefficient

β	Same-polarization gain
\mathcal{E}	Cross-polarization loss
MP_R	Multipath signal power measured at the RHCP antenna
$MP_{R_{RHCP}}$	RHCP power measured at the RHCP antenna
$MP_{R_{LHCP}}$	LHCP power collected by the RHCP antenna
MP_L	Multipath signal power collected by the LHCP antenna
$Received_R$	Total received signal power for the RHCP antenna
$Received_L$	Total received signal power for the LHCP antenna
LOS_L	Received LOS component for the LHCP antenna
$MP_{L_{RHCP}}$	RHCP power measured at the LHCP antenna
$MP_{L_{LHCP}}$	LHCP power measured at the LHCP antenna
$P(t)$	Signal power
d_{NAV}	Navigation bit
f_{GHz}	GPS signal carrier frequency
$PRN(t)$	C/A code sequence
$\delta\tau$	Code phase offset
δf	Frequency error
R	Autocorrelation function
$\delta\phi_0$	Carrier phase offset
\mathcal{T}_{LOS}	LOS code delay

I	In-phase correlator output
Q	Quadrature-phase correlator output
\mathbf{X}_k	State vector
\mathbf{Z}_k	Measurement vector
Φ_{k-1}	Dynamic coefficient matrix
\mathbf{H}_k	Measurement sensitivity matrix
\mathbf{W}_k	Plant and observation noises
\mathbf{V}_k	Observation noises
$\Delta(k-j)$	Kronecker delta function
$\mathbf{P}_{k k-1}$	Priori covariance matrix
\mathbf{K}_k	Kalman gain
$\mathbf{P}_{k k}$	Posteriori covariance matrix
$I_p^{\text{primary}}, Q_p^{\text{primary}}$	In-phase and Quadrature phase correlator outputs for the primary loop
$I_p^{\text{secondary}}, Q_p^{\text{secondary}}$	In-phase and Quadrature phase correlator outputs for the secondary loop
$R_G(\tau)$	Autocorrelation function of the GPS C/A code signal
T_{CA}	C/A code chipping period
$R_{RHCP}(\tau)$	RHCP autocorrelation function
$R_{LHCP}(\tau)$	LHCP autocorrelation function
$MP^{\text{Pseudorange}}$	Pseudorange multipath error
$C^3\text{NAVIG}^2\text{TM}$	Combined Code and Carrier Phase for Navigation using GPS

	and GLONASS
C/N ₀	Carrier-to-Noise Ratio
GSRN _x TM	GNSS Software Navigation Receiver

List of Abbreviations

AR	Auto Regressive
CCIT	Calgary Centre for Innovative Technology
EKF	Extended Kalman Filter
DLL	Delay Lock Loop
DOP	Dilution of Precision
DRC	Doppler Removal and Correlation
GDOP	Geometric Dilution of Precision
GNSS	Global Navigation Satellites System
GPS	Global Positioning System
ICT	Information and Communications Technology
IF	Intermediate Frequency
IFFT	Inverse Fast Fourier Transform
KPDLL	Kalman Phase and Delay Lock Loop
KPLL	Kalman Phase Lock Loop
KLOS	Kalman Line-Of-Sight
KMP	Kalman Multipath
LHCP	Left Hand Circularly Polarized
LNA	Low Noise Amplifier

LOS	Line-Of-Sight
MEDLL	Multipath Estimating Delay Lock Loop
MP	Multipath
MUSIC	MULTiple SIGNAL Classification
NCO	Numerically Controlled Oscillator
PLAN	Position, Location And Navigation
PLL	Phase Lock Loop
PRN	Pseudo Random Noise
RF	Radio Frequency
RHCP	Right Hand Circularly Polarized
RMSE	Root Mean Square Error
SMR	Signal to Multipath Ratio
SNR	Signal-to-Noise Ratio
USB	Universal Serial Bus

Chapter One: INTRODUCTION

RF multipath is a phenomenon where different replicas of the transmitted signal arrive at the receiver with different delays relative to the Line-of-Sight signal (LOS), causing a bias in the estimate of the received signal's code phase. Specific characteristics of the multipath make the development of multipath mitigation techniques one of the most challenging and demanding fields in GPS receiver design.

1.1 Background

1.1.1 GPS error sources

Pseudorange measurements, which are also called code-phase measurements, are affected by different types of errors. These error sources are the ionospheric delay, tropospheric delay, receiver clock and satellite ephemeris errors, receiver dynamic error, multipath and thermal noise. In GPS receivers operating in single point processing mode, most of these errors can be mitigated or completely eliminated depending on the receiver type. For example, the ionospheric error can be reduced by approximately 50% on average in mid-latitudes by using the broadcasted ionospheric corrections. Dual-frequency receivers can theoretically eliminate the ionospheric delay completely (Braasch 2001).

Differential techniques give even better positioning performance by eliminating all error sources that are common to both receivers for short baselines and fast differential update rates. The ionospheric delay, tropospheric delay, satellite clock and ephemeris errors are

common errors that can be nearly eliminated. Thermal noise and receiver dynamic tracking errors can also be minimized through designing tracking loops with minimum required noise bandwidth. Multipath errors at the reference and remote receivers are not correlated, and hence multipath errors cannot be eliminated through differential algorithms. This makes multipath the dominant error source especially in high precision GPS applications.

1.1.2 Multipath signal polarization

The GPS signal has a right hand circular polarization (RHCP). In a RHCP signal, the electric field vector describes a helix of a right hand screw along the direction of transmission. The signal's polarization may change upon reflection depending on the reflector type (reflection coefficient) and the grazing angle (the angle at which the signal reaches the reflector). In the case of GPS signals, the polarization may change from RHCP to left hand circular polarization (LHCP) if the grazing angle is greater than the Brewster angle (Yang & Porter 2005a). Since the characteristics of the signal such as amplitude, phase and polarization depend on the reflector type, the reflected GPS signal (multipath) gives valuable information about the characteristics of the multipath environment. This information extracted from the GPS reflected signals can be used in remote sensing applications like soil moisture estimation (Manandhar et al 2004). Hence, in general, the analysis of reflected signal can be helpful in characterizing the multipath environment.

1.2 Multipath parameterization techniques overview

Parametric during-correlation multipath mitigation techniques can be categorized as a class of multipath parameterization techniques in which the multipath components embedded in the composite signal are estimated and then removed. These methods are implemented in the tracking loops before the range measurements are obtained. This parametric class includes the Multipath Estimating Delay Locked Loop (MEDLL) (Van Nee 1992), Kalman filter-based joint estimation of code phase and multipath parameters (Iltis 1990), and frequency domain techniques such as Inverse Fast Fourier Transform (IFFT) and Multiple Signal Classification (MUSIC) (Yang & Porter 2005b). The MEDLL decomposes the received composite signal into LOS and non-line-of-sight (NLOS) components. Using the LOS component, unbiased measurements of code and carrier phase can be made. In the MEDLL structure several (6-10) correlators are employed to estimate multipath and LOS parameters (amplitude, phase and relative code delay) using maximum likelihood criteria. Finally, a standard correlator is applied to the LOS component for estimating the code phase tracking error. The Kalman filtering technique is another parametric approach that applies Kalman filter theory for LOS and NLOS parameter estimation. In the frequency-domain multipath estimation techniques, the GPS signal transfer function is introduced as the division between the incoming composite signal's spectrum and the local replica signal's spectrum. Multipath parameter estimation becomes the determination of distinct tones of complex exponentials from a noisy channel transfer function samples. IFFT and MUSIC are two well-known estimation methods among the frequency-domain multipath parameterization techniques (Yang & Porter 2005).

Communication link quality is a major factor in the performance of a wireless system such as GPS. Therefore, a number of quality factors such as Signal-to-Noise ratio (SNR) and Rician K factor have been proposed to characterize and measure the communication link quality (Beaulieu et al 2000 , Doukas & Kalivas 2006). In multipath environments where extra paths are added to the LOS signal, the time-varying envelope of the received signal can be described by a Rician distribution with a Rician K factor (Doukas & Kalivas, 2006). These methods can be viewed as another class of multipath parameterization techniques which measure the level of multipath fading in the received composite signal.

Multipath GPS signals are mostly considered as noise and are eliminated or mitigated when applying multipath mitigation techniques. These reflected signals contain information about the reflecting object. Although this information may not be useful for accurate positioning, it can be used to identify the reflecting object itself and characterize the multipath environment (Manandhar et al 2004). Since signal polarization may change after reflection, using a dual polarized RHCP and LHCP antenna makes it possible to analyze both RHCP and LHCP multipath components. This class of multipath parameterization techniques utilizes antennas with different polarizations in order to characterize RHCP as well as LHCP multipath components (Manandhar 2004, Yang & Porter 2005).

1.3 Research Overview

1.3.1 Motivation

The Kalman filter is a linear optimum estimator which estimates the states of a system from noisy input measurements (Grewal & Andrews 2001). The key characteristic of the Kalman filter that has made it very popular as a state estimation technique is its implementation procedure. Since the Kalman filter is a recursive algorithm, state estimation is made based on just the previous time step states and the current measurements. This makes the Kalman filtering technique a suitable candidate for real time applications. Although the Kalman filter is an optimum estimator for linear dynamic systems, it can be extended for nonlinear applications (Grewal & Andrews 2001). The usual procedure is to linearise the nonlinear system at the current estimate, leading to the extended Kalman filter (EKF). This is the motivation for this work to use the EKF technique for resolving multipath components by estimating multipath parameters in the composite signal. The Kalman filtering technique combined with a dual polarized RHCP and LHCP antenna yields a powerful tool to determine different multipath parameterization factors such as signal to multipath ratios (SMR), RHCP/LHCP autocorrelation functions, fading patterns and Rician K factors. These parameters can be used to characterize the multipath especially in urban canyon environments. This specific approach will be described in detail in the following chapters.

1.3.2 Objectives and Intended contributions

In this thesis a parametric method based on the EKF technique is designed and implemented to test the Kalman filter technique feasibility in GPS L1 C/A code tracking,

particularly in moderate outdoor multipath scenarios. This multipath estimation technique is then used to process the signal collected from a dual polarized RHCP/LHCP antenna. Other multipath parameterization factors such as estimated K values, RHCP/LHCP autocorrelation functions obtained from the primary-secondary structure and measured pseudorange multipath errors are then generated for both RHCP and LHCP data sets in order to characterize the multipath environment. To achieve the described objectives, the following tasks are performed:

1- Implementing KLOS algorithm in a GNSS software receiver:

In the first phase, an EKF-based code tracking technique in a non-multipath environment is designed and implemented in GSNRxTM. The University of Calgary PLAN group's C++ based GNSS software receiver). Since this model assumes only LOS components in the received signal, it is called Kalman LOS (KLOS).

2- Verifying KLOS tracking performance with GPS real data:

The KLOS model is then tested with real static data collected from the CCIT building's roof pillar antennas. The real data is collected using the PLAN group's RF front-end in the form of digital IF samples. The KLOS tracking performance is compared to the standard tracking performance in high to moderate Carrier-to-Noise Ratio (C/N_0) levels.

3- Implementing the KMP algorithm in the GSNRxTM software and verifying its tracking and multipath estimation performance using known simulated data:

Due to the complexity of real multipath environments, the algorithm first is tested with a hardware simulator in moderate multipath scenarios. The EKF is extended to model a single multipath component in addition to the LOS component. To verify the KMP model, a simple multipath scenario consisting of a LOS signal plus one multipath signal is simulated using the PLAN group's Spirent GPS hardware simulator. The hardware simulator helps to verify the KMP model performance under different multipath component characteristics such as the number of the paths, multipath relative amplitudes and code delays.

4- Adding a multiple-channel tracking ability to the KMP algorithm and verifying its tracking performance in real multipath scenarios:

In the next phase, the KMP model is applied to real multipath data. The real data is collected in a moderate outdoor multipath environment using a dual polarized RHCP/LHCP antenna. In order to show the KMP tracking and positioning performance, it is necessary to implement a KMP algorithm for each channel. So, the KMP module first verified for a single satellite is extended and modified to enable the software receiver to track multiple satellites simultaneously.

5- Implementing Primary-Secondary structure in GSNRx™ for LHCP data analyses:

Using a dual polarized antenna gives two sets of collected data, RHCP and LHCP signals. In order to analyze the LHCP signal and compare multipath signal parameters from the RHCP and LHCP data sets, it is necessary to process both data sets with a

common locally generated reference signal. This illustrates why a primary-secondary structure should be implemented for RHCP/LHCP data analyses.

6- Parameterization of the real multipath environment by the KMP algorithm, primary-secondary structure, and K factor estimation technique using RHCP/LHCP data sets:

Since the characteristics of the signal such as amplitude, phase and polarization depends on the reflector type, the reflected GPS signal contains valuable information about the reflecting object. Using the primary-secondary structure along with the KMP algorithm helps to extract this information from the GPS reflected (multipath) signals. Hence, the analysis of reflected signal can be helpful in characterizing the GPS multipath in different multipath environments. RHCP and LHCP K factors for different satellites are also estimated which provides another technique for analyzing and comparing the multipath environment observed by the RHCP and LHCP antennas.

7- Comparing RHCP and LHCP antennas' positioning performance

Since signals received by the RHCP and LHCP antennas have different characteristics, the signals' tracking performances are quite different for the RHCP and LHCP data sets. It causes the GPS satellite geometries, Dilution of Precision (DOP) values and pseudorange measurements to be different for two similar receivers connected to the RHCP and LHCP antennas. The positioning performances of two similar U-blox receivers connected to the RHCP and LHCP antennas are then

analyzed and compared in order to investigate the effect of antenna polarization's type in the GPS positioning performance.

1.4 Thesis outline

Chapter 2 focuses on multipath theory starting from GPS signal propagation to signal polarization change upon reflection and multipath signal formation. It then describes multipath polarization decomposition and multipath signal reception by RHCP and LHCP antennas. It shows in detail different LOS and multipath components for each of RHCP and LHCP data sets. Formulation of different signal processing procedures that are applied to these RHCP and LHCP multipath data are gathered at the end of this chapter. It clarifies how the multipath components should be modeled in the EKF algorithm.

Chapter 3 starts with a description of the standard code and carrier tracking loop structures. The proposed technique for multipath parameterization and mitigation is illustrated in the next section. It starts with Kalman filter theory and its application in tracking. Combination of the tracking loop and Kalman filter theories that were explained in the previous sections helps the reader to fully understand the Kalman-based tracking loop structure. After introducing enough background, the signal model for EKF-based code tracking loops in non-multipath environments (KLOS model) is illustrated. It then describes how multipath signal components (amplitude, carrier phase and relative code delay) can be modeled in the system dynamics. KLOS is then extended to model multipath signals as well as LOS signals. Formulations and implementation issues for this extended model (KMP) are addressed next in this chapter. A specific tracking loop

design, called a primary-secondary structure, is then proposed and explained in the last section of the chapter.

Chapter 4 is divided into two sections. In the first section the KMP algorithm implemented in GSNRx™ is tested using data simulated with a GPS hardware simulator. The simulated data helps to verify the KMP algorithm under different multipath channel characteristics such as different number of paths, different levels of SMR and various multipath relative code delays. The second section deals with real multipath scenarios and investigates the KMP algorithm performance in outdoor multipath environments.

Chapter 5 deals with some multipath parameterization techniques based on a dual polarized antenna. The test setup used for the real data collection enables one to analyze signals collected from RHCP and LHCP antennas. These dual polarization techniques are investigated in the real outdoor multipath environment in order to parameterize the multipath components. The primary-secondary structure is used for LHCP signal processing and multipath monitoring. RHCP/LHCP analyses for multipath characterization using this structure and K factor analyses are then reported in this chapter. Investigation of antenna's polarization type in the GPS positioning performance is conducted in the last section of the chapter.

Conclusions, recommended future works, and a brief summary on this thesis research work are given in Chapter 6.

Chapter Two: BACKGROUND

GPS signals are transmitted in the form of RF electromagnetic waves. The signals can be fully characterized by their amplitude, phase, wavelength, and polarization. Amplitude, phase, and wavelength values bear information about the GPS navigation message, spread spectrum code delay, and Doppler frequency of the signal, and hence they are fully studied and formulated in the literature. Signal polarization is one characteristic of the signal that is of less concern in the GPS signal processing. In multipath environments where the signal undergoes a series of non-line-of-sight (NLOS) propagations such as absorption, refraction, diffraction, and reflection, signal polarization is susceptible to different changes. Hence, signal polarization becomes an interesting topic to study under these conditions. In this chapter, signal polarization, especially GPS signal polarization in multipath environments, will be studied in detail.

2.1 Signal polarization

“The polarization of a uniform wave describes the time-varying behaviour of the electric field intensity vector at a given point in space” (Cheng 1993). Signals can be linearly, circularly or elliptically polarized. In a linearly polarized wave, the electric field intensity vector (\mathbf{E}) is oriented in a fixed direction perpendicular to the magnetic field intensity vector (\mathbf{H}) and the direction of propagation. In circular and elliptical polarizations, the direction of \mathbf{E} at a given point changes with time so the tip of \mathbf{E} traces out a circle or an ellipse in the plane accordingly. Figure 2.1 shows these three types of signal

polarizations. The \mathbf{E} vector can be decomposed into two components, namely one perpendicular (E_v) and another one parallel (E_h) to the surface plane.

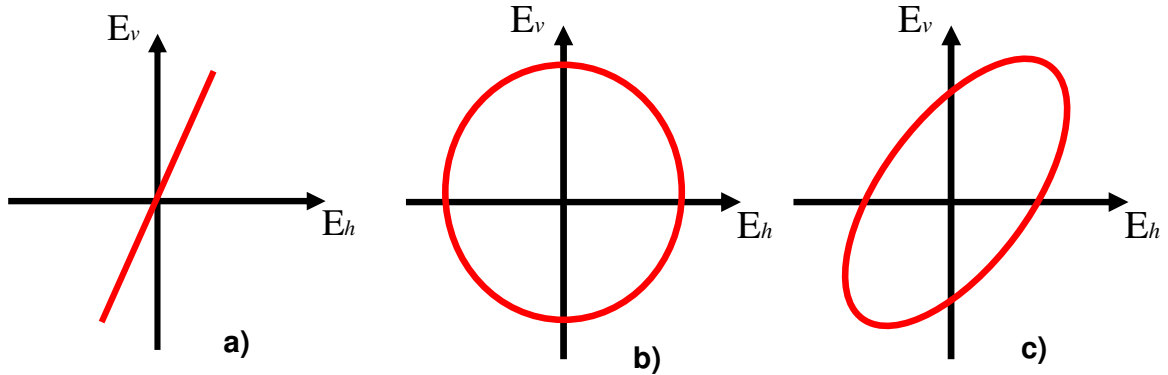


Figure 2.1 : E vectors in a) linear b) circular c) elliptical polarization

Circular and elliptical polarizations can be decomposed into two linear polarizations. The total electric intensity vector ($\mathbf{E}(z)$) can be decomposed into $\mathbf{E}_h(z)$ (horizontal vector) and $\mathbf{E}_v(z)$ (vertical vector) components, where \mathbf{a}_h and \mathbf{a}_v are the horizontal and vertical unit vectors respectively, and the signal is assumed to be propagated along the Z axis:

$$\mathbf{E} = \mathbf{E}_h(z) + \mathbf{E}_v(z) = \mathbf{a}_h E_h e^{-jkz} \pm \mathbf{a}_v E_v e^{-jkz} \quad (2.1)$$

When Eq. 2.1 is multiplied by the time component and the real part of the resultant value, one obtains:

$$\begin{aligned} \mathbf{E}(z,t) &= \Re\{[\mathbf{a}_h E_h e^{-jkz} \pm \mathbf{a}_v E_v e^{-jkz}] e^{j\omega t}\} \\ &= \mathbf{a}_h E_h \cos(\omega t - kz) \pm \mathbf{a}_v E_v \cos(\omega t - kz - \frac{\pi}{2}), \end{aligned} \quad (2.2)$$

where k (rad/m) is the wave number and ω (rad/sec) is the angular frequency. As is clear from Eq. 2.2, the horizontal and vertical components are functions of z and t , which means that their values change with time when they are propagating along the z axis. This makes the total \mathbf{E} vector spin clockwise or counter clockwise within a circle or an ellipse. If E_h and E_v are equal to each other, \mathbf{E} rotates over time and makes a circle (circular polarization). \mathbf{E} rotates around an ellipse and makes an elliptical polarization if E_h and E_v are not equal to each other.

Left and right-handed polarization depends on the direction of the electric vector (\mathbf{E}) rotation. If \mathbf{E} rotates in a counter clockwise direction, the polarization is called right-hand (positive), and if it rotates clockwise the polarization is called left-hand (negative). Right-hand and left-hand polarizations can be represented as

$$\mathbf{E}_{rhcp}(z) = \mathbf{a}_h E_h e^{-jkz} - j\mathbf{a}_v E_v e^{-jkz} \quad (2.3)$$

$$\mathbf{E}_{lhcp}(z) = \mathbf{a}_h E_h e^{-jkz} + j\mathbf{a}_v E_v e^{-jkz} \quad (2.4)$$

Hence, the E_h and E_v values and \pm (summation or subtraction) determines the polarization type.

A linearly polarized plane wave can also be decomposed into a left-hand circularly polarized (LHCP) wave and a right-hand circularly polarized (RHCP) wave (Cheng

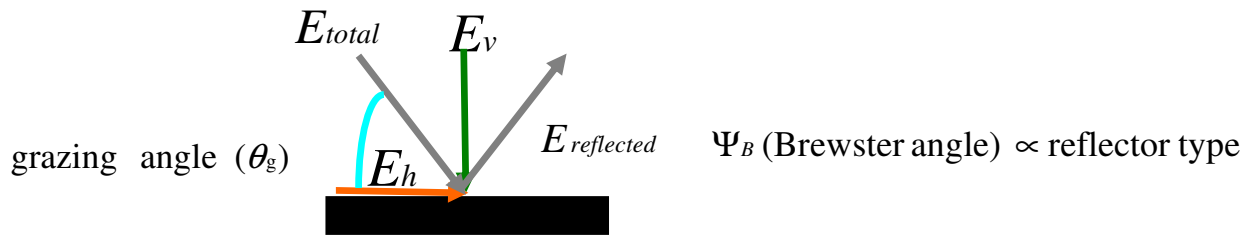
1983). The decomposition scheme where $\mathbf{E}(z)$ is a horizontally polarized signal, and $\mathbf{E}_{rhcp}(z)$, $\mathbf{E}_{lhcp}(z)$ are its corresponding RHCP and LHCP components can be written as

$$\begin{aligned}\mathbf{E}(z) &= \mathbf{a}_h E_h e^{-jkz} = \mathbf{E}_{rhcp}(z) + \mathbf{E}_{lhcp}(z) \\ \mathbf{E}_{rhcp}(z) &= \frac{E_h}{2} (\mathbf{a}_h - j\mathbf{a}_v) e^{-jkz} \\ \mathbf{E}_{lhcp}(z) &= \frac{E_h}{2} (\mathbf{a}_h + j\mathbf{a}_v) e^{-jkz}\end{aligned}\tag{2.5}$$

2.2 Reflected GPS Signal polarization analyses

The GPS signal has a right hand circular polarization (RHCP), but its polarization may change upon reflection depending on the reflector type (reflection coefficient) and the grazing angle (the angle at which the signal reaches the reflector). In this section, factors which determine the reflected signal polarization are discussed. Suppose that a GPS signal reaches the reflector with a grazing angle θ_g . Its corresponding \mathbf{E} vector can be decomposed into horizontal and vertical components as shown in Figure 2.2. Since GPS is a RHCP wave, vertical and horizontal components have the same absolute values before reflection, but the reflector's attenuation factor is not the same for these two components. As a result, the absolute values of vertical and horizontal components will not be the same after the reflection, which results in an elliptical polarization of the reflected signal. This elliptical polarization can be left hand or right hand depending on the grazing angle (θ_g) and the Brewster angle (Ψ_B). The Brewster angle (also called the polarization angle) is a property of the reflector type that has typically small values for metallic reflectors (less than 5 degrees). The horizontal component's phase always

changes 180 degrees after the reflection, but the vertical component's phase changes 180 degrees only if the grazing angle is greater than the Brewster angle.



- if $\theta_g < \Psi_B$ E_v changes its phase by 0 \Rightarrow Right - handed Elliptically polarized(RHEP)
 $\theta_g = \Psi_B$ $\Gamma_h = 0 \Rightarrow$ Vertical linearly polarized(VLP)
 $\theta_g > \Psi_B$ E_v changes its phase by 180 \Rightarrow Left - handed Elliptically polarized(LHEP)

Figure 2.2 : Incoming and reflected signals

It can be concluded that for grazing angles less than the Brewster angle, only the horizontal component changes its polarity (equivalent to a 180 degree phase change) and the signal is kept right hand, but for grazing angles greater than the Brewster angle, both horizontal and vertical components change their polarity and this makes the resultant \mathbf{E} vector to have left hand polarization. Figure 2.3 summarizes the reflected signal polarization analysis (Yang & Porter 2005b).

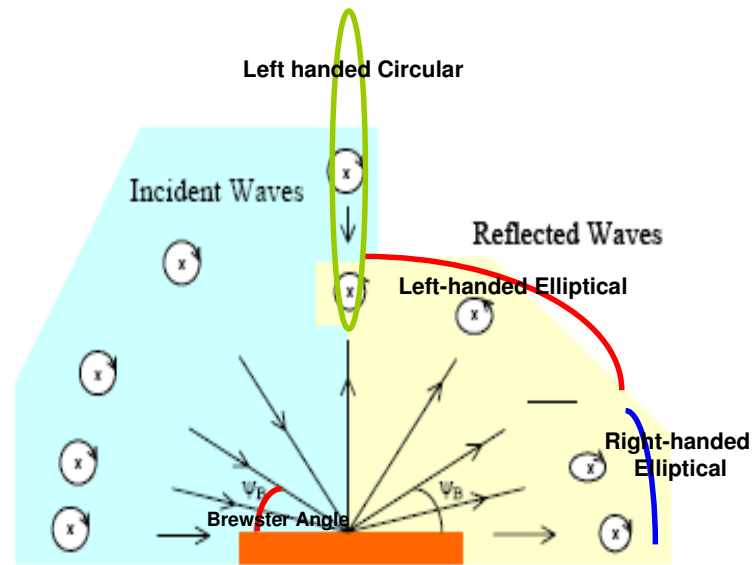


Figure 2.3: Reflected signal polarization (Yang & Porter 2005b)

2.2.1 Decomposition of elliptical polarization into right and left handed circular polarization

In this work, reflected signals are collected through a dual polarized RHCP and LHCP antenna. Each of these antennas has two power reception patterns for RHCP and LHCP received signals, but as was explained in the previous section the received reflected signal is neither RHCP nor LHCP. It was also mentioned in the previous section that a linear polarization can be decomposed into a right and left hand circular polarization. All the aforementioned concepts motivate one to analyze if an elliptical polarization can be decomposed into right and left hand circular polarizations. This section deals with elliptical polarization decomposition which can be led into a method to formulate the signals collected from RHCP and LHCP antennas. As was described in Section 2.1, a linear polarization can be decomposed into two circular polarizations, left and right handed, both with the same absolute \mathbf{E} vector values. Figure 2.4 suggests that an elliptical

polarization can also be decomposed into two circular polarizations, but with different absolute \mathbf{E} vector values for the right and left hand circular polarization. It shows two circular polarizations that have electric intensity vectors with different absolute values. The grey vector is the electric intensity vector for the RHCP signal which rotates clockwise around the grey circle (assuming the direction of propagation is pointed into the page). The LHCP electric intensity vector and its correspondent rotation circle (in blue) are sketched in two different snapshots. In the first snapshot (t_1), the RHCP and LHCP electric vectors are aligned to each other and have the same direction. The resultant vector, which is constructed by adding these two vectors, is shown in red and is called an elliptical vector. As both RHCP and LHCP vectors are added in phase, the elliptical vector is maximum for this snapshot. t_2 is the second snapshot when both RHCP and LHCP vectors have rotated 90 degrees. The RHCP electric field vector has rotated 90 degrees clock-wise while the LHCP vector has rotated 90 degrees counter-clockwise which results in the RHCP and LHCP electric vectors having a 180 degrees offset with respect to each other. Since these vectors are subtracted from each other in this snapshot, the resultant elliptical vector is minimum. Once the minimum and maximum electric vectors are found for the resultant elliptical signal, major and minor axes for the rotating ellipse can be easily found. This ellipse is shown in Figure 2.5 where major and minor axes belong to the t_1 and t_2 snapshots respectively. This elliptical polarization can be left or right hand depending on which of the RHCP and LHCP components is dominant. If the RHCP electric absolute value is dominant, the resultant elliptical polarization is right handed. The same deduction can also be made for the left

hand elliptical polarization. Hence, we conclude that a right or left hand elliptical polarization can be decomposed into RHCP and LHCP signals.

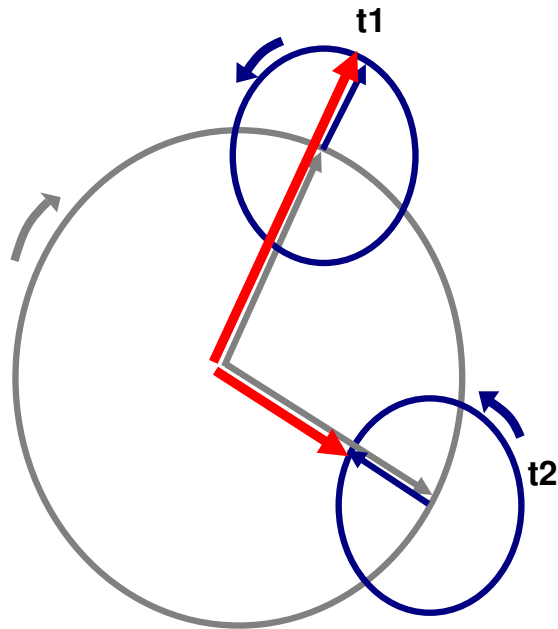
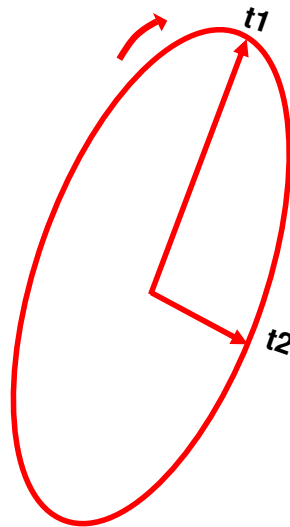


Figure 2.4: RHCP (grey) and LHCP (blue) E vectors



$$t1: E_{\text{Elliptical}_{\max}} = E_{\text{RHCP}} + E_{\text{LHCP}}$$

$$t2: E_{\text{Elliptical}_{\min}} = E_{\text{RHCP}} - E_{\text{LHCP}}$$

Figure 2.5: Resulting elliptical polarization

2.2.2 Signal propagation analysis in a simple multipath scenario

In this section a simple multipath scenario is introduced. Figure 2.6 shows this multipath scenario in which two rays are coming towards the receiving antenna. The first ray (LOS) is directly received by the antenna at the angle θ_{LOS} (LOS angle), while the second ray (LOS2) is first reflected by an object and then received by the antenna at an angle θ_{MP} (multipath angle).

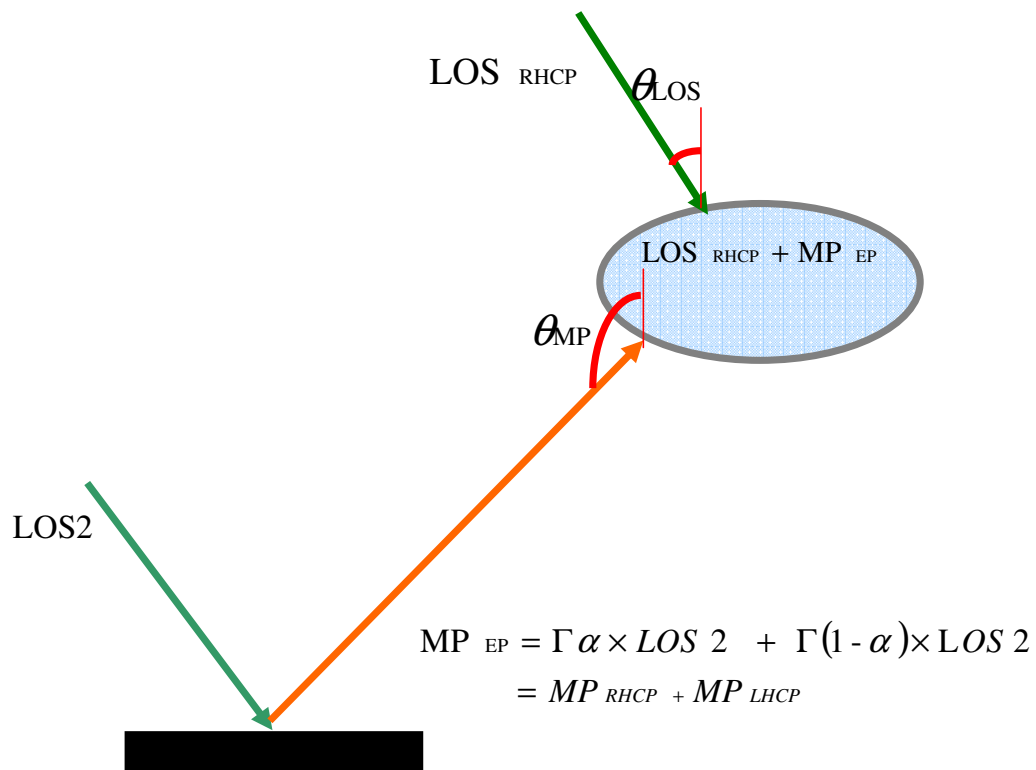


Figure 2.6: Multipath scenario

As was discussed in Section 2.2, a reflected GPS signal is generally elliptically polarized, which can be viewed as a combination of RHCP and LHCP signals. This reflected signal (multipath signal) is called MP_{EP} therefore the total signal reaching the antenna is $LOS_{RHCP} + MP_{EP}$. It is also well known that the signal is attenuated after reflection.

So, the LOS2 signal becomes attenuated by a factor Γ and its power will be split between the RHCP and LHCP components after the reflection. This phenomenon can be expressed as

$$P_{\text{Elliptical}} = \Gamma(P_{\text{LHCP}} + P_{\text{RHCP}}) = |\Gamma|^2 \alpha \times P_{\text{Elliptical}} + |\Gamma|^2 (1 - \alpha) \times P_{\text{Elliptical}}$$

$$\alpha = \left(\frac{|E_{\text{LHCP}}|}{|E_{\text{total}}|} \right)^2 \propto \text{grazing angle, Reflector type}$$

$$\Gamma \propto \text{Reflector type} \quad (2.6)$$

where α is a factor which shows the percentage of RHCP power as a function of total multipath power, and Γ is the reflection attenuation factor which is a property of the reflecting object.

The RHCP antenna can receive both RHCP and LHCP signals, but the RHCP antenna gain is not the same for the two signals. The RHCP antenna receives the RHCP signal with considerably higher gain than the LHCP signal. Let us express the RHCP antenna gain for RHCP signal as the “same-polarization gain (β)”, and the RHCP antenna gain for LHCP signal as the “cross-polarization loss (ϵ)”. Figure 2.7 shows the RHCP antenna power patterns for both RHCP (blue line) and LHCP (green line) signals. The same-polarization gain and cross-polarization loss are evaluated in LOS and multipath angles $\{\beta(\theta_{\text{LOS}}), \beta(\theta_{\text{MP}}), \epsilon(\theta_{\text{LOS}}), \epsilon(\theta_{\text{MP}})\}$. The attenuation and gain factors in Figure 2.7 are in units of dB.

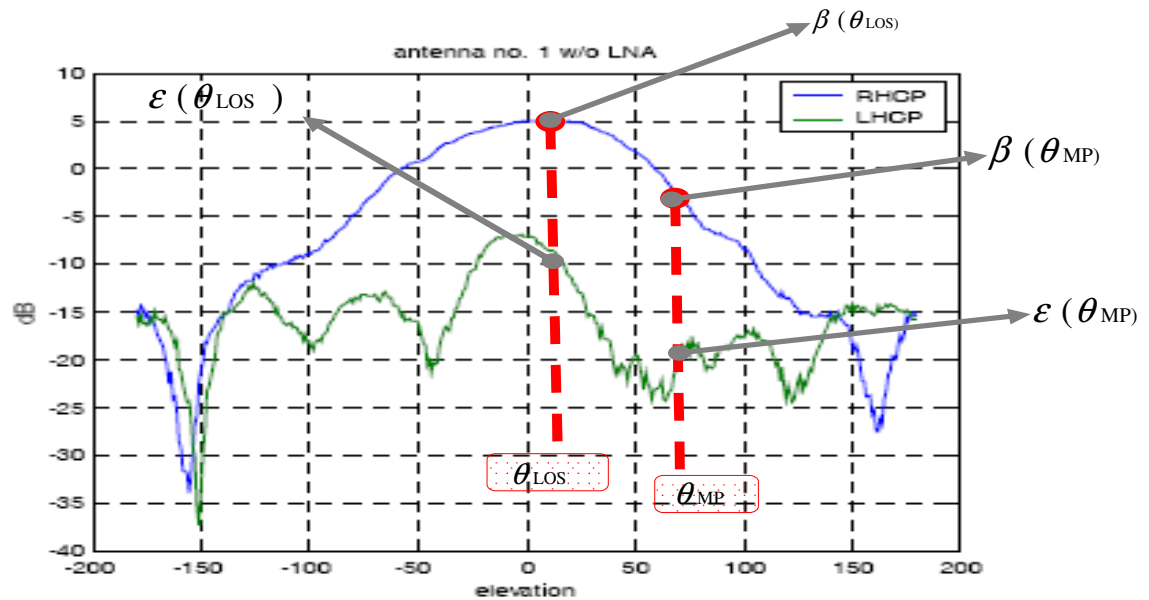


Figure 2.7: RHCP antenna power patterns for RHCP and LHCP signals (Yang & Porter 2005b)

2.3 Multipath signal reception by RHCP and LHCP antennas

Figure 2.8 shows the previous multipath scenario in which the received composite signal is comprised of a LOS signal (LOS_{RHCP}) and one multipath signal (MP_{EP}). This signal is collected by a dual polarized RHCP/LHCP antenna.

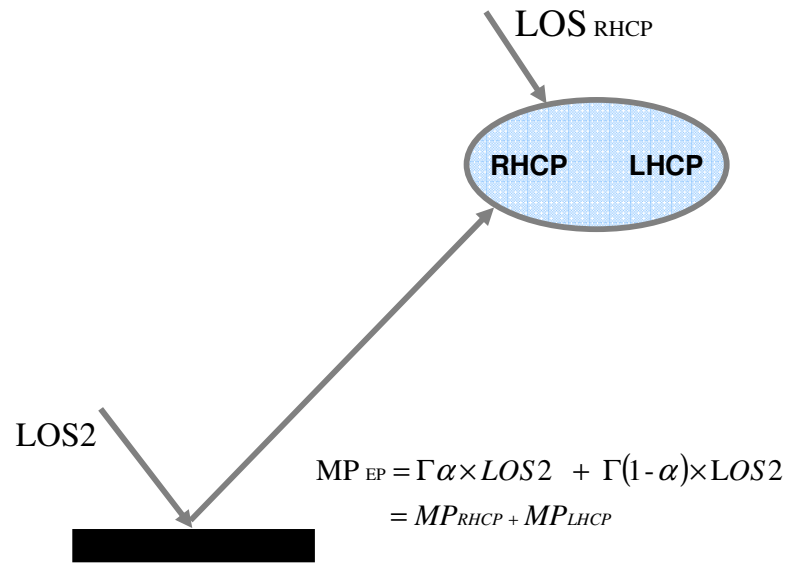


Figure 2.8: Multipath scenario

The following assumptions have been made in the rest of this chapter for the sake of simplicity

1-The multipath environment consists of one reflector, and the signal is reflected once (one extra path).

2- The RHCP antenna same-polarization gain = LHCP antenna same-polarization gain = β

3-The RHCP antenna cross-polarization loss = LHCP antenna cross-polarization loss = ϵ

4- The antenna gain at multipath angle is less than LOS angle { $\beta(\theta_{MP}) < \beta(\theta_{LOS})$ }.

5- The Cross-polarization gain is considerably less than the same-polarization gain { $\epsilon(\theta) \ll \beta(\theta)$ }.

In the equations described below, the LOS component is ignored and just multipath signals are considered. The multipath signal power measured at the RHCP antenna (MP_R) can be written as

$$\begin{aligned} MP_R &= MP_{R_{RHCP}} + MP_{R_{LHCP}} = \beta(\theta_{MP}) \times MP_{RHCP} + \mathcal{E}(\theta_{MP}) \times MP_{LHCP} \\ &= \beta(\theta_{MP}) |\Gamma|^2 \alpha \times LOS2 + \mathcal{E}(\theta_{MP}) |\Gamma|^2 (1 - \alpha) \times LOS2 \end{aligned} \quad (2.7)$$

MP_R has two components, $MP_{R_{RHCP}}$ and $MP_{R_{LHCP}}$. $MP_{R_{RHCP}}$ is the RHCP power measured at the RHCP antenna while $MP_{R_{LHCP}}$ is the LHCP power collected by the RHCP antenna. $LOS2$ is the second LOS ray before the reflection (Figure 2.8). This equation shows how the signal ($LOS2$) has undergone different changes during the reception. These signal deformations are formulated as different parameters such as β , Γ , α and \mathcal{E} . The $MP_{R_{RHCP}}$ component is generated after $LOS2$ has been attenuated by a factor of Γ (reflection coefficient), and then received at the RHCP antenna with a gain of $\beta(\theta_{MP})$. The factor α shows the proportion of the signal power that has kept its right-hand polarization after the reflection. The $MP_{R_{LHCP}}$ component is also constructed after $LOS2$ has been attenuated by the factor Γ (reflection coefficient), and then received by the RHCP antenna with a gain of $\mathcal{E}(\theta_{MP})$. The factor $(1 - \alpha)$ shows the proportion of the signal power that has changed its polarization to the left-hand polarization after reflection.

The multipath signal power collected by the LHCP antenna (MP_L) can be written as

$$\begin{aligned}
MP_L &= MP_{L_{RHCP}} + MP_{L_{LHCP}} = \mathcal{E}(\theta_{MP}) \times MP_{RHCP} + \beta(\theta_{MP}) \times MP_{LHCP} \\
&= \mathcal{E}(\theta_{MP}) |\Gamma|^2 \alpha \times LOS2 + \beta(\theta_{MP}) |\Gamma|^2 (1 - \alpha) \times LOS2
\end{aligned} \tag{2.8}$$

The RHCP component is received by the cross-polarization loss factor of $\mathcal{E}(\theta_{MP})$, and the LHCP component is received by the same-polarization gain factor of $\beta(\theta_{MP})$.

2.3.1 Total received signal power at RHCP and LHCP antennas

The previous section focused on deriving equations for the received multipath signal power while this section illustrates the equations for the total received power (LOS + multipath components). It also discusses the dominant signal power components for the RHCP and LHCP antennas. The total received signal power for the RHCP antenna ($Received_R$) can be formulated as

$$\begin{aligned}
Received_R &= LOS_R + MP_R = \beta(\theta_{LOS}) \times LOS + MP_{R_{RHCP}} + MP_{R_{LHCP}} \\
&= \beta(\theta_{LOS}) \times LOS + \beta(\theta_{MP}) \times MP_{RHCP} + \mathcal{E}(\theta_{MP}) \times MP_{LHCP} \\
&= \beta(\theta_{LOS}) \times LOS + \beta(\theta_{MP}) |\Gamma|^2 \alpha \times LOS2 + \mathcal{E}(\theta_{MP}) |\Gamma|^2 (1 - \alpha) \times LOS2
\end{aligned} \tag{2.9}$$

$Received_R$ is comprised of three components: RHCP multipath ($MP_{R_{RHCP}}$), and LHCP multipath ($MP_{R_{LHCP}}$) parts which were explained previously, and the LOS (LOS_R) component. The LOS ray (Figure 2.6) is received by the RHCP antenna with a gain of $\beta(\theta_{LOS})$ which is denoted as LOS_R . This equation shows how LOS and $LOS2$ rays have changed into the aforementioned three signal power components. Since $\mathcal{E}(\theta_{MP}) \ll \beta(\theta_{MP})$, the $MP_{R_{LHCP}}$ can be assumed to be considerably smaller than the other two components.

Hence, LOS_R and MP_{RHCP} are the dominant power components in the total received power for the RHCP antenna.

The total received signal power for the LHCP antenna ($Received_L$) can be written as

$$\begin{aligned}
 Received_L &= LOS_L + MP_L = LOS_L + MP_{L_{RHCP}} + MP_{L_{LHCP}} \\
 &= \varepsilon(\theta_{LOS}) \times LOS + \varepsilon(\theta_{MP}) \times MP_{RHCP} + \beta(\theta_{MP}) \times MP_{LHCP} \\
 &= \varepsilon(\theta_{LOS}) \times LOS + \varepsilon(\theta_{MP}) |\Gamma|^2 \alpha \times LOS 2 \\
 &\quad + \beta(\theta_{MP}) |\Gamma|^2 (1 - \alpha) \times LOS 2
 \end{aligned} \tag{2.10}$$

MP_L is the received multipath power component by the LHCP antenna which consists of the $MP_{L_{RHCP}}$ and $MP_{L_{LHCP}}$ parts. LOS_L is the received LOS component for the LHCP antenna. LOS_L and $MP_{L_{RHCP}}$ have been attenuated from their original signals by a factor of ε . $MP_{L_{RHCP}}$ has the second attenuation factor Γ . Therefore, it can be concluded that LOS_L and $MP_{L_{RHCP}}$ make negligible contributions to the total received power and $MP_{L_{LHCP}}$ should be the dominant signal power component for the LHCP antenna.

2.4 RHCP/LHCP data analyses along the signal processing chain

In this section, different signal processing procedures that are applied to the received RHCP and LHCP data are described and the signal outputs from each step are formulated. Again, one reflector and one reflection are assumed in the multipath scenario illustrated in Figure 2.9.

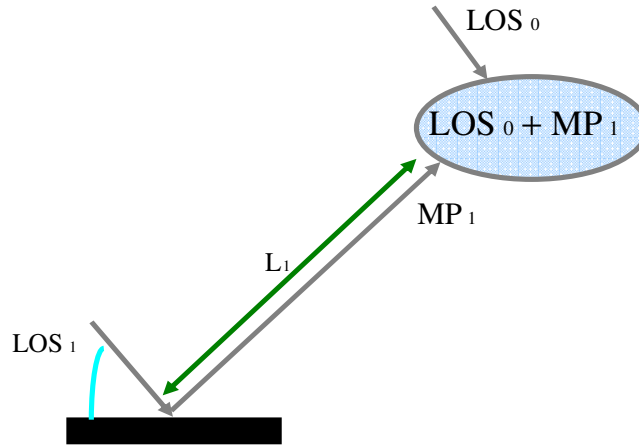


Figure 2.9: Multipath scenario

$LOS_0(t)$ is the first ray arriving directly at the antennas while $LOS_1(t)$ is the second ray reaching the reflector, and is then reflected towards the antenna. The reflected ray is the multipath signal denoted as $MP_1(t)$. $LOS_0(t)$ and $MP_1(t)$ are therefore two GPS signals which are received by the antennas. The noise term in each signal is dropped for the sake of simplicity. $LOS_0(t)$ and $LOS_1(t)$ are formulated in detail as

$$\begin{aligned} |LOS_0(t)| &= \sqrt{2P(t)} d_{NAV}(t) \cos(2\pi ft + \theta'_0) PRN(t - \tau_{LOS}) \\ |LOS_1(t)| &= \sqrt{2P(t)} d_{NAV}(t) \cos(2\pi ft + \theta'_1) PRN(t - \tau_{LOS} - \tau'_{MP}) \end{aligned} \quad (2.11)$$

where $P(t)$ is the signal power, d_{NAV} is the navigation bit, f is the GPS signal carrier frequency, and $PRN(t)$ is the C/A code sequence. θ'_0 is the $LOS_0(t)$ signal carrier phase arriving at the antenna, and θ'_1 is the signal carrier phase for the second ray $\{LOS_1(t)\}$. τ_{LOS} is the $LOS_0(t)$ code delay and τ'_{MP} is the $LOS_1(t)$ code delay relative to $LOS_0(t)$. $MP_1(t)$ traverses the path of L_1 to reach the antenna. This path length adds τ''_{MP} chips to the signal's code phase. Therefore, The total $MP_1(t)$ code delay relative to

the $LOS_0(t)$ signal is $\tau_{MP} = \tau'_{MP} + \tau''_{MP}$. The RHCP antenna's gain and the reflection coefficient factor embedded in the RHCP and LHCP multipath components can be factorized and denoted as χ^R . The reflection coefficient is a complex parameter ($\Gamma = |\Gamma|e^{j\angle\Gamma}$) that changes the amplitude and phase of the receiving signal. The RHCP antenna itself also introduces some phase changes in the received signal which is also included in the χ^R factor. Therefore, generally speaking, χ^R is a complex value which models all amplitude, and phase changes in the multipath signal $\{MP_1(t)\}$ due to the multipath reception. Hence, the received signal can be written as

$$\begin{aligned}
Received_r(t) &= \beta(\theta_{LOS}) \times LOS_0(t) + MP_1 \\
&= \beta(\theta_{LOS}) \times LOS_0(t) + \beta(\theta_{MP}) \Gamma \alpha \times LOS_1(t) + \varepsilon(\theta_{MP}) \Gamma(1-\alpha) \times LOS_1(t) \\
&= \beta(\theta_{LOS}) \times LOS_0(t) + [\beta(\theta_{MP}) \Gamma \alpha + \varepsilon(\theta_{MP}) \Gamma(1-\alpha)] \times LOS_1(t) \\
&= \beta(\theta_{LOS}) \times LOS_0(t) + \chi^R \times LOS_1(t)
\end{aligned} \tag{2.12}$$

$$\chi^R = |\chi^R| e^{j\angle\chi^R} = \beta(\theta_{MP}) \Gamma \alpha + \varepsilon(\theta_{MP}) \Gamma(1-\alpha) \tag{2.13}$$

If one substitutes Eq. 2.11 into Eq. 2.12, the received signal for the RHCP antenna can be shown as

$$\begin{aligned}
Received_r(t) &= |\beta(\theta_{LOS})| \times \sqrt{2P(t)} d_{NAV}(t) \cos(2\pi f t + \theta_0) PRN(t - \tau_{LOS}) \\
&\quad + |\chi^R| \sqrt{2P(t)} d_{NAV}(t) \cos(2\pi f t + \theta'_1 + \angle\chi^R) PRN(t - \tau_{LOS} - \tau'_{MP} - \tau''_{MP})
\end{aligned} \tag{2.14}$$

The first term in Eq.2.14 is the LOS signal component, and the second term is due to the combined RHCP and LHCP multipath signal components. Since the antenna itself

introduces phase changes in the received signal, θ'_0 has changed into θ_0 to include antenna's effect in the LOS signal $\{ \text{LOS}_0(t) \}$ carrier phase. The multipath signal phase is also changed from θ'_1 into $\theta'_1 + \angle\chi_r$ to include $\text{LOS}_1(t)$ signal phase change due to the reflection, extra path length L_1 , and RHCP antenna gain. The extra code phase delay (τ''_{MP}) introduced in the second ray is also considered in Eq. 2.14 which was not considered before in Eq. 2.11. By defining the following parameters

$$\begin{aligned}
 A_{\text{LOS}_L}(t) &= |\beta(\theta_{\text{LOS}})| \times \sqrt{2P(t)} \\
 A_{\text{MP}_R}(t) &= |\chi_r| \sqrt{2P(t)} \\
 \theta_{1R} &= \theta'_1 + \angle\chi_r \\
 \tau_{MP} &= \tau'_{MP} + \tau''_{MP}
 \end{aligned} \tag{2.15}$$

Eq. 2.14 can be simplified as (Jee et al 2002)

$$\begin{aligned}
 \text{Received}_R(t) &= A_{\text{LOS}_R}(t) \times d_{\text{NAV}}(t) \text{Cos}(2\pi ft + \theta_0) \text{PRN}(t - \tau_{\text{LOS}}) \\
 &\quad + A_{\text{MP}_R}(t) \times d_{\text{NAV}}(t) \text{Cos}(2\pi ft + \theta_{1R}) \text{PRN}(t - \tau_{\text{LOS}} - \tau_{MP})
 \end{aligned} \tag{2.16}$$

The same formulas for the LHCP antenna can be shown as

$$\begin{aligned}
 \text{Received}_L(t) &= \varepsilon(\theta_{\text{LOS}}) \times \text{LOS}_0(t) + \varepsilon(\theta_{\text{MP}}) \Gamma \alpha \times \text{LOS}_1(t) + \beta(\theta_{\text{MP}}) \Gamma(1 - \alpha) \times \text{LOS}_1(t) \\
 &= \varepsilon(\theta_{\text{LOS}}) \times \text{LOS}_0(t) + [\varepsilon(\theta_{\text{MP}}) \Gamma \alpha + \beta(\theta_{\text{MP}}) \Gamma(1 - \alpha)] \times \text{LOS}_1(t) \\
 &= \beta(\theta_{\text{LOS}}) \times \text{LOS}_0(t) + \chi_L \times \text{LOS}_1(t)
 \end{aligned} \tag{2.17}$$

$$\chi_L = |\chi| e^{j\angle\chi} = \varepsilon(\theta_{\text{MP}}) \Gamma \alpha + \beta(\theta_{\text{MP}}) \Gamma(1 - \alpha) \tag{2.18}$$

$$\begin{aligned}
 \text{Received}_L(t) &= |\varepsilon(\theta_{\text{LOS}})| \times \sqrt{2P(t)} d_{\text{NAV}}(t) \text{Cos}(2\pi ft + \theta_0) \text{PRN}(t - \tau_{\text{LOS}}) \\
 &\quad + |\chi| \sqrt{2P(t)} d_{\text{NAV}}(t) \text{Cos}(2\pi ft + \theta'_1 + \angle\chi_L) \text{PRN}(t - \tau_{\text{LOS}} - \tau'_{MP} - \tau''_{MP})
 \end{aligned} \tag{2.19}$$

$$\begin{aligned}
A_{LOS_L}(t) &= |\varepsilon(\theta_{LOS})| \times \sqrt{2P(t)} \\
A_{MP_L}(t) &= |\chi_L| \sqrt{2P(t)} \\
\theta_{1L} &= \theta'_1 + \angle \chi_L \\
\tau_{MP} &= \tau'_{MP} + \tau''_{MP}
\end{aligned} \tag{2.20}$$

$$\begin{aligned}
Received_L(t) &= A_{LOS_L}(t) \times d_{NAV}(t) \cos(2\pi f t + \theta_0) PRN(t - \tau_{LOS}) \\
&\quad + A_{MP_L}(t) \times d_{NAV}(t) \cos(2\pi f t + \theta_{1L}) PRN(t - \tau_{LOS} - \tau_{MP}) .
\end{aligned} \tag{2.21}$$

Eqs. 2.16 and 2.21 are the received composite signals for the RHCP and LHCP antennas. These two equations will be used in the next section to derive I and Q values for the RHCP and LHCP data sets.

2.5 Correlator outputs for the RHCP data

In this section, correlator outputs (I and Q) for the RHCP data will be computed. A similar analysis can be made for deriving correlator outputs for the LHCP data. Correlator outputs are generated after the received signal is correlated with the locally generated signal. Assume the replica signal, which is generated in the receiver and given by

$$Local_R(t) = A_{Local} \cos(2\pi f_{local} t + \theta_{local}) PRN(t - \tau_{local}), \tag{2.22}$$

where f_{local} and θ_{local} are obtained from the carrier tracking loop (PLL) and τ_{local} is obtained from the code tracking loop (DLL). A_{Local} depends on the receiver's design architecture. In the GSNRXTM software receiver, A_{Local} depends on the pre-defined

quantization level. A quantization level of 2^2 means there are two bits per each generated sample, therefore $A_{Local} = \pm 1, \pm 2$.

The locally generated signal (Eq. 2.22) is correlated with the incoming signal (Eq. 2.16), and then accumulated for T_{COH} ms. This accumulation introduces an integration gain which increases the signal to noise ratio (SNR). Figure 2.10 shows this correlation and the accumulation process.

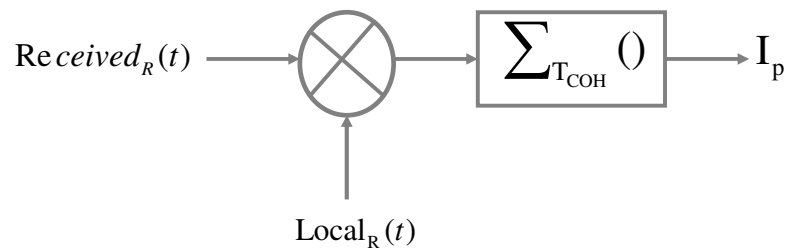


Figure 2.10: Correlation and accumulation process

By defining the parameters

$$A_{LOS} = N A_{local} A_{LOS\mathbb{R}} \quad (2.23)$$

and

$$A_{MP} = N A_{local} A_{MP\mathbb{R}}, \quad (2.24)$$

the accumulated correlator outputs can be formulated as (Jee et al 2002)

$$\begin{aligned} I_p = & d_{NAV} A_{LOS} R(\tau - \delta\tau) \text{Sinc}(\delta\mathcal{I}T) \text{Cos}(\delta\hat{\Phi}_0) \\ & + d A_{MP} R(\tau - \delta\tau - \tau_{MP}) \text{Sinc}(\delta\mathcal{I}T) \text{Cos}(\delta\hat{\Phi}_1) \\ Q_p = & d_{NAV} A_{LOS} R(\tau - \delta\tau) \text{Sinc}(\delta\mathcal{I}T) \text{Sin}(\delta\hat{\Phi}_0) \\ & + d A_{MP} R(\tau - \delta\tau - \tau_{MP}) \text{Sinc}(\delta\mathcal{I}T) \text{Sin}(\delta\hat{\Phi}_1) \end{aligned} \quad (2.25)$$

where N is the numbers of samples in the integration period T , R is the autocorrelation function of the ranging code, $\delta\tau$ is the code phase offset between locally generated code and the incoming LOS signal, and δf is the frequency error between locally generated and the incoming signal. It should be noted that $\delta\Phi_0$ and $\delta\Phi_1$ are the average phase errors over the integration interval for the $LOS_0(t)$ and $LOS_1(t)$ signal components. These average phase errors are modeled as

$$\delta\hat{\Phi}_0 = \delta\phi_0 + \frac{1}{2} \delta T \delta f + \frac{1}{6} \delta T^2 \delta \alpha \quad ; \quad \delta\phi_0 = \theta_0 - \theta_{local} = \theta_0 - \hat{\theta}_0 \quad (2.26)$$

$$\delta\hat{\Phi}_1 = \delta\phi_1 + \frac{1}{2} \delta T \delta f + \frac{1}{6} \delta T^2 \delta \alpha \quad ; \quad \delta\phi_1 = \theta_{1R} - \theta_{local} = \theta_{1R} - \hat{\theta}_0 \quad (2.27)$$

where $\delta\phi_0$ is the carrier phase offset between locally estimated phase ($\theta_{local} = \hat{\theta}_0$) and the $LOS_0(t)$ incoming signal carrier phase at the start of the integration time, and $\delta\phi_1$ is the carrier phase bias between locally estimated phase ($\theta_{local} = \hat{\theta}_0$) and the $LOS_1(t)$ incoming signal carrier phase at the start of the integration time (Psiaki 2001, Petovello & Lachapelle 2006). The same Doppler frequency and Doppler frequency rate are assumed for both $LOS_0(t)$ and $LOS_1(t)$ signals, which is a reasonable assumption for a static scenarios.

2.5.1 Correlator outputs for the general multipath scenario

Eq. 2.27 was derived for a specific multipath case where one reflector and one reflection were assumed in the multipath environment. It can easily be generalized to a multipath

scenario with L reflectors and L reflections (one reflection per each reflector). The received composite signal by the RHCP antenna for such multipath scenarios can be written as

$$Re\ ceived_R(t) = \beta(\theta_{LOS}) \times LOS_0(t) + \chi_1 \times LOS_1(t) + \dots + \chi_L \times LOS_L(t) \quad (2.28)$$

$$LOS_0(t) = \sqrt{2P(t)} d_{NAV}(t) \cos(2\pi f t + \theta'_0) PRN(t - \tau_{LOS}) \quad (2.29)$$

$$LOS_i(t) = \sqrt{2P(t)} d_{NAV}(t) \cos(2\pi f t + \theta'_i) PRN(t - \tau_{LOS} - \tau'_{MP_i}) \quad ; i = 1, \dots, L$$

$LOS_0(t)$ is the LOS ray which is directly collected by the RHCP antenna while $LOS_i(t)$ ($1 \leq i \leq L$) is the i-th ray reaching the i-th reflector, and then reflected towards the antenna. τ_{LOS} is the $LOS_0(t)$ code delay and τ'_{MP_i} is the $LOS_i(t)$ ($i = 1, \dots, L$) code delay relative to $LOS_0(t)$. χ^i is the complex value which models all amplitude and phase changes in the reflected signal due to the reflection, extra path length between the i-th reflector and antenna, and the RHCP antenna gain. If one also considers τ''_{MP_i} chips code delay corresponding to the path length that the i-th ray should transverse between the i-th reflector and the antenna, substitution of Eq. 2.29 into 2.28 gives

$$\begin{aligned} Re\ ceived_R(t) = & \beta(\theta_{LOS}) \times \sqrt{2P(t)} d_{NAV}(t) \cos(2\pi f t + \theta'_0) PRN(t - \tau_{LOS}) \\ & + \chi_1 \times \sqrt{2P(t)} d_{NAV}(t) \cos(2\pi f t + \theta'_1) PRN(t - \tau_{LOS} - \tau'_{MP_1} - \tau''_{MP_1}) \\ & \cdot \\ & \cdot \\ & + \chi_L \times \sqrt{2P(t)} d_{NAV}(t) \cos(2\pi f t + \theta'_L) PRN(t - \tau_{LOS} - \tau'_{MP_L} - \tau''_{MP_L}) \end{aligned} \quad (2.30)$$

Equation 2.30 can be further simplified by defining the following parameters:

$$\begin{aligned}
A_{LOS}(t) &= |\beta(\theta_{LOS})| \times \sqrt{2P(t)} \\
A_{MP_i}(t) &= |\chi_i| \times \sqrt{2P(t)} \\
\theta_i &= \theta'_i + \angle \chi_i \\
\tau_{MP_i} &= \tau'_{MP_i} + \tau''_{MP_i}
\end{aligned} \tag{2.31}$$

Therefore, Eq. 2.30 can be re-written as

$$\begin{aligned}
Received_r(t) &= A_{LOS}(t) \times d_{NAV}(t) \cos(2\pi f t + \theta_0) PRN(t - \tau_{LOS}) \\
&+ \sum_{i=1}^L A_{MP_i}(t) \times d_{NAV}(t) \cos(2\pi f t + \theta_i) PRN(t - \tau_{LOS} - \tau_{MP_i})
\end{aligned} \tag{2.32}$$

Finally, the accumulated correlator outputs can be formulated as

$$\begin{aligned}
I_p &= d_{NAV} A_0 R(\tau - \delta\tau) \text{Sinc}(\delta f T) \cos(\delta\hat{\Phi}_0) \\
&+ \sum_{i=1}^L d_{NAV} A_i R(t - \delta\tau - \tau_{MP_i}) \text{Sinc}(\delta f T) \cos(\delta\hat{\Phi}_i) \\
Q_p &= d_{NAV} A_0 R(\tau - \delta\tau) \text{Sinc}(\delta f T) \sin(\delta\hat{\Phi}_0) \\
&+ \sum_{i=1}^L d_{NAV} A_i R(t - \delta\tau - \tau_{MP_i}) \text{Sinc}(\delta f T) \sin(\delta\hat{\Phi}_i),
\end{aligned} \tag{2.33}$$

where A_i and $\delta\hat{\Phi}_i$ ($0 \leq i \leq L$) are defined as

$$\begin{aligned}
A_0 &= N A_{local} A_{LOS}(t) \\
A_i &= N A_{local} A_{MP_i}(t) \quad 1 \leq i \leq L
\end{aligned} \tag{2.34}$$

$$\begin{aligned}
\delta\hat{\Phi}_0 &= \delta\phi_0 + \frac{1}{2} \delta\Gamma \delta f + \frac{1}{6} \delta\Gamma^2 \delta\alpha & ; \delta\phi_0 = \theta_0 - \theta_{Local} = \theta_0 - \hat{\theta}_0 \\
\delta\hat{\Phi}_i &= \delta\phi_i + \frac{1}{2} \delta\Gamma \delta f + \frac{1}{6} \delta\Gamma^2 \delta\alpha & ; \delta\phi_i = \theta_i - \theta_{Local} = \theta_i - \hat{\theta}_0
\end{aligned} \tag{2.35}$$

The next chapter describes the extended Kalman filter (EKF) technique for multipath parameter' estimations based on the correlator outputs .The equations derived for the correlator outputs in this chapter are used in the next chapter to design the Kalman multipath (KMP) algorithm.

Chapter Three: REVIEW OF TECHNIQUES USED

This chapter describes the major techniques used in this thesis for analyzing and parameterizing multipath signals. The results generated from these techniques along with other multipath analyses are presented in the next chapter. This chapter starts with providing the required background for introducing Kalman-based tracking loop structures by describing first the standard tracking loop structure, and then the Kalman filter theory. The Kalman PLL (KPLL) as the first tracking loop structure is then introduced in Section 3.3. The chapter continues by extending KPLL to the general Kalman-based tracking loop structure which can be used in a non-multipath environment. This model (Kalman LOS) is described in detail in Section 3.4. Section 3.5 and 3.6 explain how the Kalman LOS (KLOS) model can be further extended to a more general case to account for the multipath components as well as the LOS components embedded in the received composite signal. A primary-secondary structure is another proposed structure which is developed and described in Section 3.7 for analyzing GPS signals collected by a dual RHCP/LHCP antenna.

3.1 Standard tracking loop structure

The standard tracking loop scheme consists of two separate loops. The loop which tracks the signal's carrier phase is called Phase Lock Loop (PLL), and the second loop which tracks the signal's ranging code is called Delay Lock Loop (DLL). Standard PLL and

DLL structures are sketched in Figures 3.1 and 3.2, respectively. The implementation scheme which is already developed in GSNRxTM will be illustrated in this section.

In the PLL, a discriminator and loop filter are used to estimate the carrier phase and Doppler from the I and Q measurements. The overall discriminator and loop filter can be considered as the optimal estimator for the carrier Doppler. The output of the discriminator is an estimate of the instantaneous carrier phase error (error between local and incoming signal). The loop filter takes this phase error signal as an input, and estimates the corresponding carrier Doppler. This carrier Doppler accounts for the carrier phase bias and also the phase rate due to the Doppler effect (relative motion between the receiver and satellite). Hence, the carrier Doppler is set as a command for the carrier NCO.

The DLL discriminator and loop filter are also used to estimate code phase and code Doppler from the I and Q measurements. The overall code discriminator and loop filter are considered as the optimal estimator for the code Doppler. The output of the code discriminator is the code phase error (phase error between local and incoming signal). The code loop filter accepts this code phase error as its input and estimates the corresponding code Doppler. The generated code Doppler accounts for the code delay between local and incoming signals and also the code phase rate due to the carrier Doppler effect. In the standard DLL structure, just the code Doppler is set as a command for the carrier NCO. In the carrier-aided DLL, the total code Doppler is obtained from two parts. The first part comes from the PLL (carrier aiding) to account for the code

Doppler due to the carrier Doppler, and the second part comes from the code loop filter, which accounts for the code bias between local and the incoming code phases.

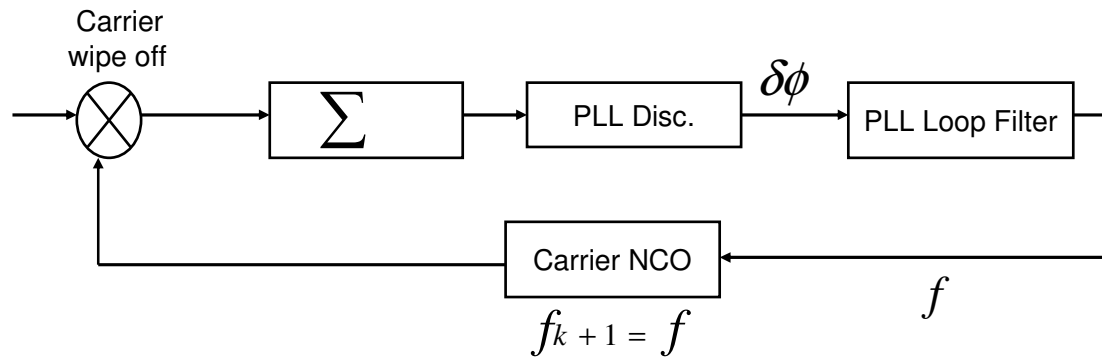


Figure 3.1: Standard carrier tracking loop

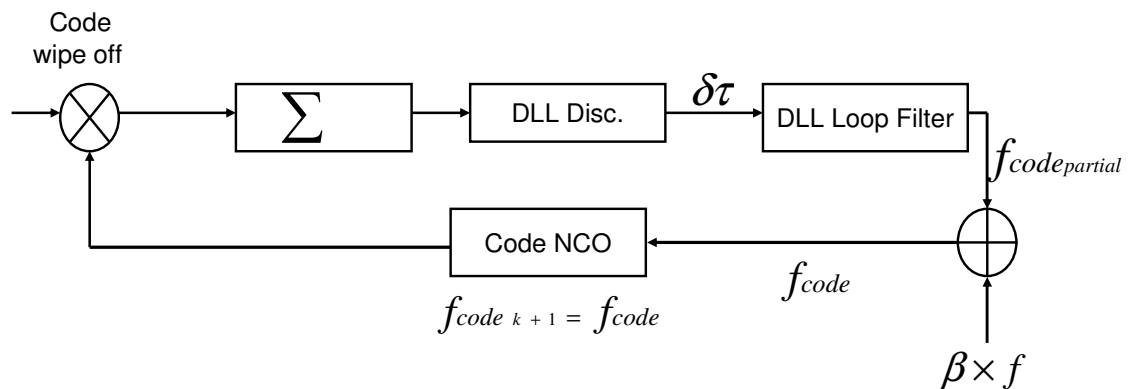


Figure 3.2: Standard code tracking loop

3.2 Kalman filter theory

The Kalman filter is a linear optimal estimator which addresses the problem of estimating the states of a dynamic system perturbed by white noise. This optimal estimator uses the current measurements corrupted by white noise and the estimated states from the

previous time step to derive the current states' estimate. No history of observations and/or states is required. This recursive nature of the Kalman filter has made it a practical and popular technique in the statistical estimation theory (Grewal & Andrews 2001).

It is assumed that the states and measurements dynamics can be modeled as plant and observation models respectively. The plant and measurement models in a discrete time system can be written as

$$\mathbf{X}_k = \Phi_{k-1} \mathbf{X}_{k-1} + \mathbf{W}_{k-1} \quad (3.1)$$

$$\mathbf{Z}_k = \mathbf{H}_k \mathbf{X}_k + \mathbf{V}_k \quad (3.2)$$

where \mathbf{X}_k is the $n \times 1$ state vector, and \mathbf{Z}_k is the $m \times 1$ measurement vector. Φ_{k-1} ($n \times n$) and \mathbf{H}_k ($n \times m$) are dynamic coefficient and measurement sensitivity matrices. The measurement vector \mathbf{Z}_k is assumed to be a linear function of the state vector \mathbf{X}_k .

The plant and observation noises (\mathbf{W}_k and \mathbf{V}_k) are assumed to be uncorrelated zero mean Gaussian processes with

$$E\{\mathbf{W}_k\} = 0 \quad (3.3)$$

$$E\{\mathbf{W}_k \mathbf{W}_j^T\} = \delta(k-j) \mathbf{Q}_k$$

$$E\{\mathbf{V}_k\} = 0 \quad (3.4)$$

$$E\{\mathbf{V}_k \mathbf{V}_j^T\} = \delta(k-j) \mathbf{R}_k$$

$$E\{\mathbf{V}_k \mathbf{W}_j^T\} = 0 \text{ for all } k \text{ and } j \quad (3.5)$$

where $\delta(k-j)$ is the Kronecker delta function.

The Kalman filter produces the estimate of the state vector \mathbf{X}_k ($\hat{\mathbf{X}}_k$) from the measurement vector \mathbf{Z}_k by minimizing the mean square error e_k as

$$e_k = E\{(\mathbf{X}_k - \hat{\mathbf{X}}_k)^T (\mathbf{X}_k - \hat{\mathbf{X}}_k)\}. \quad (3.6)$$

The computational steps in each filter iteration can be summarized as follows (Grewal & Andrews 2001):

1- The a priori state estimate at time step k ($\hat{\mathbf{X}}_{k|k-1}$) is first computed using Φ_{k-1} , and $\hat{\mathbf{X}}_{k-1|k-1}$.

$$\hat{\mathbf{X}}_{k|k-1} = \Phi_{k-1} \hat{\mathbf{X}}_{k-1|k-1} \quad (3.7)$$

2- The a priori covariance matrix at time k ($\mathbf{P}_{k|k-1}$), which is the error covariance matrix before the measurement update, is then computed from $\mathbf{P}_{k-1|k-1}$, Φ_{k-1} , and \mathbf{Q}_{k-1} . $\mathbf{P}_{k-1|k-1}$ is the posteriori matrix at time $k-1$ and the error covariance matrix after the measurement update at $k-1$ is given as follows:

$$\mathbf{P}_{k|k-1} = \Phi_{k-1} \mathbf{P}_{k-1|k-1} \Phi_{k-1}^T + \mathbf{Q}_{k-1} \quad (3.8)$$

3- The Kalman gain (\mathbf{K}_k) is then computed from $\mathbf{P}_{k|k-1}$ (step 2), \mathbf{H}_k , and \mathbf{R}_k as

$$\mathbf{K}_k = \mathbf{P}_{k|k-1} \mathbf{H}_k^T (\mathbf{H}_k \mathbf{P}_{k|k-1} \mathbf{H}_k^T + \mathbf{R}_k)^{-1} \quad (3.9)$$

4- The posteriori matrix at time k ($\mathbf{P}_{k|k}$) is then calculated using Steps 2 and 3 as

$$\mathbf{P}_{k|k} = (\mathbf{I} - \mathbf{K}_k \mathbf{H}_k) \mathbf{P}_{k|k-1} \quad (3.10)$$

5- The a posteriori state estimate ($\hat{\mathbf{X}}_{k|k}$), which is the state vector estimate after the measurement update is derived using \mathbf{K}_k , initial states vector $\hat{\mathbf{X}}_0$, and the input data \mathbf{Z}_k is

$$\hat{\mathbf{X}}_{k|k} = \hat{\mathbf{X}}_{k|k-1} + \mathbf{K}_k (\mathbf{Z}_k - \mathbf{H}_k \hat{\mathbf{X}}_{k|k-1}) \quad (3.11)$$

Joseph form:

In order to have a well-conditioned solution, the covariance error matrices in each iteration ($\mathbf{P}_{k|k-1}, \mathbf{P}_{k|k}$) should be symmetric and positive-definite. Assuming a symmetric positive definite plant noise matrix (\mathbf{Q}_k), the matrix $\mathbf{P}_{k|k-1}$ computed in Step 2 has the desired characteristics. In order to overcome ill-conditioning in the $\mathbf{P}_{k|k}$ derivation, $\mathbf{P}_{k|k}$ can be computed in an alternative way called Joseph form as

$$\mathbf{P}_{k|k} = (\mathbf{I} - \mathbf{K}_k \mathbf{H}_k) \mathbf{P}_{k|k-1} (\mathbf{I} - \mathbf{K}_k \mathbf{H}_k)^T + \mathbf{K}_k \mathbf{R}_k \mathbf{K}_k^T \quad (3.12)$$

The Joseph form expression is the summation of two symmetric and nonnegative matrices which ensures that $\mathbf{P}_{k|k}$ is also symmetric and positive definite.

3.2.1 Extended Kalman Filter (EKF)

The Kalman filter described in the previous section is a linear estimator. In many applications, the plant and measurement models are non-linear and the system dynamics and measurements are non-linearly dependent on the states. Kalman filter theory can be extended to such non-linear systems by linearising the models around the a priori state estimates leading to the extended Kalman filter (EKF). Although the linearization procedure makes the EKF a suboptimal estimator, as far as the linearization effect can be

negligible, the EKF can result in nearly optimum solution for the non-linear state estimates. A non-linear stochastic system with non-linear plant and measurement models can be described as

$$\mathbf{X}_k = f_{k-1}(\mathbf{X}_{k-1}) + \mathbf{W}_{k-1} \quad (3.13)$$

$$\mathbf{Z}_k = h_k(\mathbf{X}_k) + \mathbf{V}_k \quad (3.14)$$

where \mathbf{X}_k is the $n \times 1$ state vector at time step k which is related to the previous step state (\mathbf{X}_{k-1}) by the non linear function f , \mathbf{Z}_k is the $m \times 1$ measurement vector which is non-linearly dependent on \mathbf{X}_k . The functions f and h are differentiable functions of the state vector \mathbf{X} . \mathbf{W}_k and \mathbf{V}_k are plant and observation noise vectors with the following characteristics:

$$E\{\mathbf{W}_k\} = 0 \quad (3.15)$$

$$E\{\mathbf{W}_k \mathbf{W}_j^T\} = \delta(k-j) \mathbf{Q}_k$$

$$E\{\mathbf{V}_k\} = 0 \quad (3.16)$$

$$E\{\mathbf{V}_k \mathbf{V}_j^T\} = \delta(k-j) \mathbf{R}_k$$

$$E\{\mathbf{V}_k \mathbf{W}_j^T\} = 0 \quad \text{for all } k \text{ and } j \quad (3.17)$$

The computational steps for each EKF iteration can be summarized as (Grewal & Andrews 2001):

1- The predicted state estimate at time step k ($\hat{\mathbf{X}}_{k|k-1}$) is first computed using f_{k-1} , and $\hat{\mathbf{X}}_{k-1|k-1}$:

$$\hat{\mathbf{X}}_{k|k-1} = f_{k-1}(\hat{\mathbf{X}}_{k-1|k-1}) \quad (3.18)$$

2-The predicted measurement vector is computed as

$$\hat{\mathbf{Z}}_k = h_k(\hat{\mathbf{X}}_{k-1|k-1}). \quad (3.19)$$

3- f and h are then linearised around $\hat{\mathbf{X}}_{k|k-1}$ for each filter iteration. $\Phi^{[1]}_{k-1}$, and $\mathbf{H}^{[1]}_{k-1}$ are the linearised versions of the f and h functions respectively:

$$\Phi^{[1]}_{k-1} \approx \left. \frac{\partial f_k}{\partial \mathbf{X}} \right|_{\mathbf{X}_{k-1|k-2}} \quad (3.20)$$

$$\mathbf{H}^{[1]}_k \approx \left. \frac{\partial h_k}{\partial \mathbf{X}} \right|_{\mathbf{X}_{k|k-1}} \quad (3.21)$$

4- The a priori covariance matrix at time step k ($\mathbf{P}_{k|k-1}$) is then computed as

$$\mathbf{P}_{k|k-1} = \Phi^{[1]}_{k-1} \mathbf{P}_{k-1|k-1} \Phi^{[1]T}_{k-1} + \mathbf{Q}_{k-1}. \quad (3.22)$$

5- The Kalman gain (\mathbf{K}_k) is then derived from $\mathbf{P}_{k|k-1}$ (step 2), $\mathbf{H}^{[1]}_{k-1}$, and \mathbf{R}_k :

$$\mathbf{K}_k = \mathbf{P}_{k|k-1} \mathbf{H}^{[1]T}_{k-1} (\mathbf{H}^{[1]}_{k-1} \mathbf{P}_{k|k-1} \mathbf{H}^{[1]T}_{k-1} + \mathbf{R}_k)^{-1} \quad (3.23)$$

6- The posteriori estimate ($\hat{\mathbf{X}}_{k|k}$) is derived using \mathbf{K}_k , priori state vector $\hat{\mathbf{X}}_{k|k-1}$, and the input data \mathbf{Z}_k :

$$\hat{\mathbf{X}}_{k|k} = \hat{\mathbf{X}}_{k|k-1} + \mathbf{K}_k (\mathbf{Z}_k - \hat{\mathbf{Z}}_k) \quad (3.24)$$

7- $\mathbf{P}_{k|k}$ is computed in the last step.

$$\mathbf{P}_{k|k} = (\mathbf{I} - \mathbf{K}_k \mathbf{H}^{[1]_k}) \mathbf{P}_{k|k-1} \quad (3.25)$$

3.2.2 Innovation statistics

When the Kalman filter works as an optimal estimator, the innovations ($v_k = \mathbf{Z}k - \hat{\mathbf{Z}}k$) have the following characteristics

$$\begin{aligned} E\{v_k\} &= 0 \\ E\{v_k v_k^T\} &= \mathbf{R}_k - \mathbf{H}_k \mathbf{P}_{k|k-1} \mathbf{H}_k^T \end{aligned} \quad (3.26)$$

In the suboptimal case, the innovations are not white and their covariance can be written as (Gelb et al 1974)

$$C_j = E\{v_k v_{k+j}^T\} = \begin{cases} \mathbf{R}_k + \mathbf{H}_k \mathbf{P}_{k|k-1} \mathbf{H}_k^T = \mathbf{C}_0 & j = 0 \\ \mathbf{H} [\Phi (\mathbf{I} - \mathbf{K}_k \mathbf{H}_k)]^{j-1} \Phi (\mathbf{P}_{k|k-1} \mathbf{H}_k^T - \mathbf{K} \mathbf{C}_0) & j > 0 \end{cases} \quad (3.27)$$

In the optimal solution $\mathbf{K} = \mathbf{P}_{k|k-1} \mathbf{H}_k^T \mathbf{C}_0^{-1}$, where $\mathbf{C}_j > 0 = 0$, the innovations sequence (v_k) becomes white with a covariance matrix \mathbf{C}_0 .

3.3 KPLL structure

Now that the background theory for the tracking loops and Kalman filtering has been introduced, the first Kalman-based tracking loop structure is described in this section. In this new structure, shown in Figure 3.3 and called Kalman PLL (KPLL), the code tracking loop is the same as the DLL in the standard structure, but the carrier tracking loop has changed to an EKF-based loop.

Like the standard structure, the DLL discriminator and loop filter are used as the optimal estimator for the code Doppler. The KPLL structure is an alternative structure for the carrier tracking loop. The KPLL is a substitute for both the PLL discriminator and loop filter. Early, prompt and late correlator outputs are used as the input measurements to the KPLL. The KPLL estimates the carrier phase error ($\delta\phi_{k+1}$) and carrier Doppler error (δf_{k+1}) from these noisy measurements. The predicted errors are then used as the commands in the NCO to update the carrier phase (ϕ_k) and carrier Doppler (f_k) by adding these corrections to the previous values of the carrier phase and carrier Doppler. The NCO commands are updated in each iteration of the KPLL as

$$\begin{aligned} f_{k+1} &= f_k + \delta f_{k+1} \\ \phi_{k+1} &= \phi_k + \delta\phi_{k+1} \end{aligned} \tag{3.28}$$

In the KPLL, both updated carrier phase (ϕ_{k+1}) and carrier Doppler (f_{k+1}) are sent as commands to the carrier NCO. These updated NCO commands are then used to generate the local signal which is further used in the code and carrier correlation process.

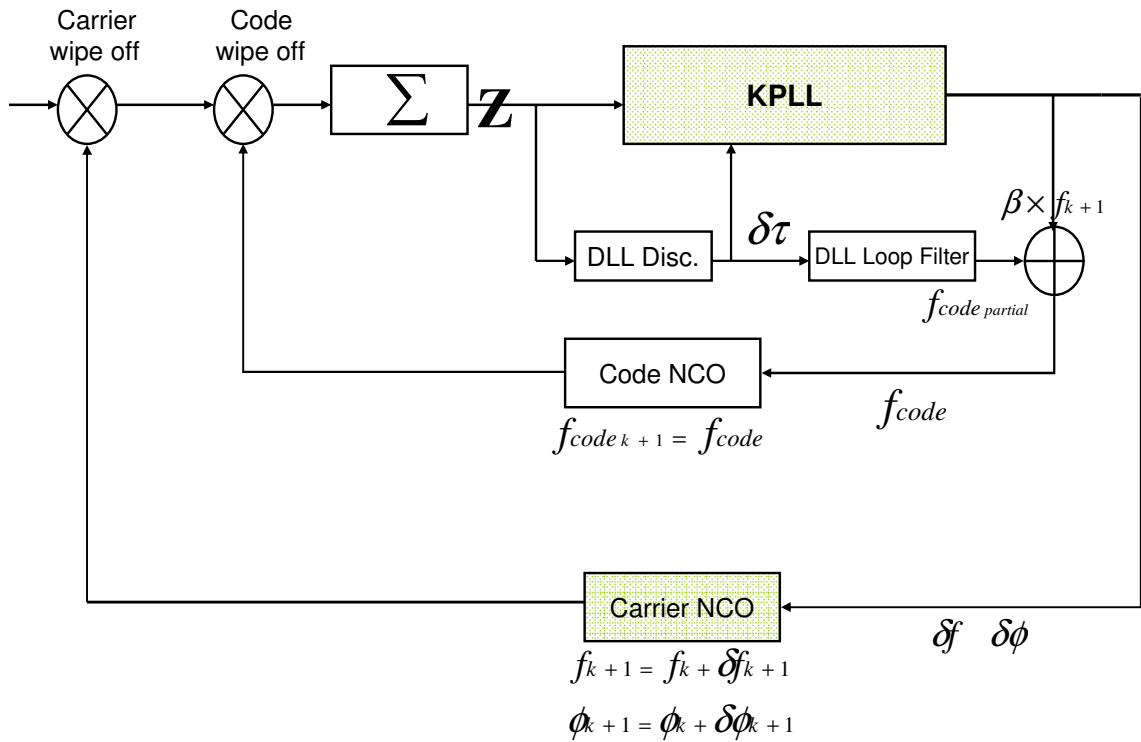


Figure 3.3: KPLL carrier tracking loop structure

The KPLL needs code phase error estimates for calculating the \mathbf{H} matrix elements. These code phase error estimates are obtained from the DLL loop (code discriminator). So both the KPLL and DLL modules need some information from the other one in order to operate correctly. It should be noted that carrier phase ($\Delta\phi_{k+1}$) and carrier Doppler errors (Δf_{k+1}) are reset to zero after each loop update in order to avoid errors to be accumulated and causing the PLL to lose lock.

3.3.1 KPLL implementation

The KPLL implementation in the GSNRxTM software receiver is described next. GSNRxTM is a C++ based GPS software receiver in which all the proposed structures are developed (Petovello et al 2008). In the KPLL structure, no extra path is assumed to be

added to the LOS signal, so the received signal is composed of just LOS signal components.

The m-th correlator output for this non-multipath case can be written as

$$\begin{aligned}
 I_{\Delta m} + j Q_{\Delta m} &= d_{NAV} A_{LOS} \text{Sinc}(\delta f T) R(\delta \tau_0 + \Delta_m) \text{Cos}(\delta \hat{\Phi}_0) \\
 &\quad + j d_{NAV} A_{LOS} \text{Sinc}(\delta f T) R(\delta \tau_0 + \Delta_m) \text{Sin}(\delta \hat{\Phi}_0) \quad , \\
 &= d_{NAV} A_0 R(\delta \tau_0 + \Delta_m) \text{Cos}(\delta \hat{\Phi}_0) \\
 &\quad + j d_{NAV} A_0 R(\delta \tau_0 + \Delta_m) \text{Sin}(\delta \hat{\Phi}_0) \quad m = 1, 2, 3
 \end{aligned} \tag{3.29}$$

where A_0 is the accumulated amplitude during the integration period δT , R is the autocorrelation function of the ranging code, $\delta \tau_0$ is the code phase bias between the locally generated code and the incoming signal and δf is the frequency error between the locally generated and the incoming signal. $\delta \hat{\Phi}_0$ is the average phase error over the integration interval, which is modeled as (Psiaki 2001, Petovello & Lachapelle 2006)

$$\delta \hat{\Phi}_0 = \delta \phi_0 + \frac{1}{2} \delta T \delta f + \frac{1}{6} \delta T^2 \delta \alpha \quad , \tag{3.30}$$

where $\delta \phi_0$ is the carrier phase bias between the locally estimated phase ($\theta_{local} = \hat{\theta}_0$) and the incoming signal carrier phase at the start of the integration time, and

$$\delta \phi_0 = \theta_0 - \theta_{local} = \theta_0 - \hat{\theta}_0 \quad . \tag{3.31}$$

The correlator outputs ($I_{\Delta m}, Q_{\Delta m}$) are used as the input vector (\mathbf{Z} vector) to the EKF module to estimate the states in each filter iteration. The elements of \mathbf{Z} are the conventional early, prompt, and late correlator outputs:

$$\begin{aligned}
 \mathbf{Z}^T &= [I_{\Delta 1} \ Q_{\Delta 1} \ I_{\Delta 2} \ Q_{\Delta 2} \ I_{\Delta 3} \ Q_{\Delta 3}] \\
 &= [I_P \ Q_P \ I_E \ Q_E \ I_L \ Q_L] \quad .
 \end{aligned} \tag{3.32}$$

As suggested by Eq.3.29, the $\text{Sinc}(\cdot)$ terms are effectively combined with the amplitude terms because the attenuation due to the frequency error is difficult to separate from the

variations in the amplitude. Therefore, the frequency error is only estimated from the average phase error component $\delta\Phi_0$ (Petovello & Lachapelle 2006).

Since the code tracking loop is the same as the DLL in the standard structure, and only the carrier tracking loop is implemented in the EKF-based structure, the state vector matrix \mathbf{X} is a 4×1 matrix modeling all the carrier phase components, and the total accumulated amplitude:

$$\begin{aligned}\mathbf{X}_k &= \Phi \mathbf{X}_{k+1} + \mathbf{W}_k \\ \mathbf{X}^T &= [A_0 \ \delta\phi_0 \ \delta f \ \delta a] \\ \mathbf{W}^T &= [\omega_A \ \omega_\phi \ \omega_f \ \omega_a]\end{aligned}\tag{3.33}$$

A_0 is the accumulated amplitude during the integration period δT , $\delta\phi_0$ is the carrier phase error between the locally estimated phase and the incoming phase, δf is the frequency error and δa is the frequency error rate. The amplitude (A_0) dynamic is modeled as a first order autoregressive (AR) process:

$$\dot{A}_0 = \omega_A\tag{3.34}$$

where ω_A is a zero mean Gaussian process.

The carrier phase dynamic model takes the form of a discrete-time triple integrator driven by a discrete-time white noise (Brown & Hwang 1992). Its continuous form can be written as

$$\begin{aligned}\delta\dot{\phi} &= \delta f + \omega_\phi \\ \delta\dot{f} &= \delta a + \omega_f \\ \delta\dot{a} &= \omega_a\end{aligned}\tag{3.35}$$

The discrete-time transition matrix (Φ) for the KPLL model can be derived from Eqs.3.34 and 3.35:

$$\Phi = \begin{bmatrix} \mathbf{1} & 0 & 0 & 0 \\ 0 & 1 & \delta T & \frac{1}{2}\delta T^2 \\ 0 & 0 & 1 & \delta T \\ 0 & 0 & 0 & 1 \end{bmatrix} \quad (3.36)$$

The covariance of the $\mathbf{W}^T_{\Phi} = [\omega_{\phi} \ \omega_f \ \omega_a]$ is a combination of three terms. The third term models a random walk acceleration of the line-of-sight (LOS) vector to the satellite, and the other two model the effects of receiver clock phase random walk and frequency random walk. The total covariance of \mathbf{W}^T_{Φ} can be written as (Psiaki & Jung 2002)

$$E\{\mathbf{W}_{\Phi}\mathbf{W}^T_{\Phi}\} = \begin{bmatrix} \frac{1}{20}q_{LOS}\delta T^5 + \frac{1}{3}S'_g\delta T^3 + S'_f\delta T & \frac{1}{8}q_{LOS}\delta T^4 + \frac{1}{2}S'_g\delta T^2 & \frac{1}{6}q_{LOS}\delta T^3 \\ \frac{1}{8}q_{LOS}\delta T^4 + \frac{1}{2}S'_g\delta T^2 & \frac{1}{3}q_{LOS}\delta T^3 + S'_g\delta T & \frac{1}{2}q_{LOS}\delta T^2 \\ \frac{1}{6}q_{LOS}\delta T^3 & \frac{1}{2}q_{LOS}\delta T^2 & q_{LOS}\delta T \end{bmatrix}$$

$$S'_g = S_g \omega_{L1}^2$$

$$S'_f = S_f \omega_{L1}^2$$

(3.37)

where q_{LOS} is the intensity of the acceleration random walk, and S_g and S_f are the receiver clock's frequency and phase random walk intensities. ω_{L1} is the nominal L1 frequency.

H Matrix calculation

In the KPLL model, the relation between the states and measurements is non-linear which is described by the non-linear function h . h should therefore be linearised in order to obtain $\mathbf{H}^{[1]}_k$ elements:

$$\mathbf{Z}_k = h_k(\mathbf{X}_k) + \mathbf{V}_k \quad (3.38)$$

$$\mathbf{H}^{[1]}_k \approx \left. \frac{\partial h_k}{\partial \mathbf{X}} \right|_{\mathbf{X}_{k|k-1}} = [h_{i,j}] \quad (3.39)$$

$$h_{i,j} = \frac{\partial \hat{Z}[i]}{\partial X[j]_{k|k-1}} \quad (3.40)$$

$$\begin{aligned} \hat{\mathbf{Z}}^T &= [\hat{I}_{\Delta_1} \hat{Q}_{\Delta_1} \hat{I}_{\Delta_2} \hat{Q}_{\Delta_2} \hat{I}_{\Delta_3} \hat{Q}_{\Delta_3}] \\ \hat{I}_{\Delta} &= \hat{d}_{NAV} \hat{A} R(\delta\hat{\tau} + \Delta) \text{Cos}(\delta\hat{\Phi}_0) \\ \hat{Q}_{\Delta} &= \hat{d}_{NAV} \hat{A} R(\delta\hat{\tau} + \Delta) \text{Sin}(\delta\hat{\Phi}_0) \end{aligned} \quad (3.41)$$

The elements of the matrix $\mathbf{H}^{[1]}_k$ are the partial derivatives of different measurements relative to different states evaluated at the predicted values of the states. In order to obtain the H matrix, the data bit sign (d_{NAV}), amplitude (A), code phase error ($\delta\tau$), and average carrier phase error ($\delta\Phi_0$) should be predicted. Data bit sign estimation (\hat{d}_{NAV}) is achieved using a hard decision as long as the signal power strength is high (Eq.3.42). The predicted amplitude (\hat{A}) is the first state in the \mathbf{X} matrix. The average carrier phase error estimate ($\delta\hat{\Phi}_0$) is obtained from Eq. 3.30. The code phase error estimate ($\delta\hat{\tau}$) is also obtained from the DLL discriminator:

Hard Decision bit estimation (High C/No)

$$\hat{d} = \begin{cases} 1 & I_P > 0 \\ -1 & I_P < 0 \end{cases} \quad (3.42)$$

$$\begin{aligned}
\hat{A} &= X[1]_{k|k-1} \quad \text{a priori estimate} \\
\delta\hat{\phi} &= X[2]_{k|k-1} \\
\delta\hat{f} &= X[3]_{k|k-1} \\
\delta\hat{\alpha} &= X[4]_{k|k-1} \\
\delta\hat{\Phi} &= \delta\hat{\phi} + \frac{1}{2} \delta T \delta\hat{f} + \frac{1}{6} \delta T^2 \delta\hat{\alpha}
\end{aligned} \tag{3.43}$$

The partial derivatives of the in-phase observations relative to the Kalman states are formulated as

$$\begin{aligned}
\frac{\partial I_{\Delta}}{\partial A} &= \hat{d}R(\hat{\tau} + \Delta) \text{Cos}(\delta\hat{\Phi}) \\
\frac{\partial I_{\Delta}}{\partial \delta\phi} &= -\hat{d}\hat{A}R(\hat{\tau} + \Delta) \text{Sin}(\delta\hat{\Phi}) \\
\frac{\partial I_{\Delta}}{\partial \delta f} &= -\left(\frac{1}{2} \delta T\right) \hat{d}\hat{A}R(\hat{\tau} + \Delta) \text{Sin}(\delta\hat{\Phi}) \\
\frac{\partial I_{\Delta}}{\partial \delta\alpha} &= -\left(\frac{1}{6} \delta T^2\right) \hat{d}\hat{A}R(\hat{\tau} + \Delta) \text{Sin}(\delta\hat{\Phi})
\end{aligned} \tag{3.44}$$

The ideal autocorrelation function $R(\tau)$ is not differentiable. It is also not realistic when the input RF signal has passed through a band-pass filter. A more realistic autocorrelation function, which is a 6-th order polynomial approximation of $R(\tau)$, is therefore used in the KMP:

$$\begin{aligned}
R(\tau) &\approx P_6\tau^6 + \dots + P_1\tau + P_0 \\
\dot{R}(\hat{\tau} + \Delta_m) &= \frac{\partial}{\partial \tau} R(\tau) \quad ; \tau = \hat{\tau} + \Delta_m
\end{aligned} \tag{3.45}$$

3.4 KPDLL (KLOS) structure

The Kalman PLL DLL (KPDLL), illustrated in Figure 3.4, is the second proposed structure in which both code and carrier tracking loops are implemented based on the

Kalman filter technique. Since the KPDLL models only the LOS signal components, it will also be called Kalman LOS (KLOS) from now on. Both PLL and DLL discriminators and loop filters in the standard structure are substituted by a single KLOS module. Hence, the KLOS obtains the required commands for both code and carrier NCOs. The procedure these command are obtained is different from that used in the original tracking loops. In a conventional loop (Figure 3.1), the overall code and carrier Doppler ($f_{code\ k+1}$, f_{k+1}) for the next iteration are estimated and fed to the code and carrier NCOs. These Doppler values account for the phase change rate due to the Doppler effect and the bias between local and incoming signals, so there is no need to send code and carrier phase commands to the NCOs. In the KPDLL structure, these two error sources are estimated separately.

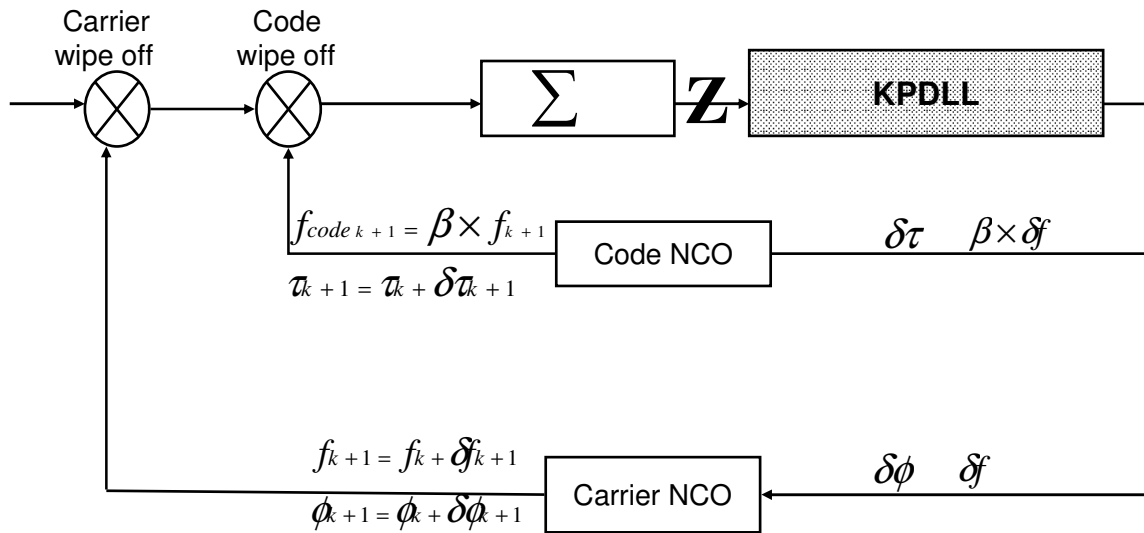


Figure 3.4: KPDLL (KLOS) code and carrier tracking loop structure

For tracking the carrier, both carrier phase and carrier Doppler (f_{k+1} and ϕ_{k+1}), are estimated separately and sent to the NCO as two different commands. The carrier phase

error ($\delta\phi_{k+1}$) is the second Kalman state and the carrier Doppler (δf_{k+1}), the third Kalman state. These estimated errors are added to the previous carrier phase (ϕ_k) and carrier Doppler (f_k) to form the updated carrier phase (ϕ_{k+1}) and carrier Doppler (f_{k+1}). The procedure for generating the carrier NCO commands in each loop iteration is as follows:

$$\begin{aligned} f_{k+1} &= f_k + \delta f_{k+1} \\ \phi_{k+1} &= \phi_k + \delta\phi_{k+1} \end{aligned} \quad (3.46)$$

For tracking the code phase, both code phase and code Doppler ($f_{code\ k+1}$ and τ_{k+1}) are estimated separately and sent to the code NCO as two different commands. The code phase error ($\delta\tau_{k+1}$) is the fourth Kalman state while the code Doppler ($\delta f_{code\ k+1}$) is obtained by multiplying the third Kalman state (δf_{k+1}) by the factor β which converts from units of Hertz to chips per second. These estimated errors are added to the previous code phase (τ_k) and code Doppler ($f_{code\ k}$) to form the updated code phase (τ_{k+1}) and code Doppler ($f_{code\ k+1}$). This procedure for generating the code NCO commands can be formulated as

$$\begin{aligned} f_{code\ k+1} &= \beta \times f_{k+1} \\ \tau_{k+1} &= \tau_k + \delta\tau_{k+1} \end{aligned} \quad (3.47)$$

These updated NCO commands are then used to generate the local signal used in the code and carrier correlation process.

3.4.1 KLOS implementation

In this section, the KPDLL implementation in the GSNRxTM software is described. As mentioned previously, the KPLL structure is an alternative implementation for the carrier tracking loop in a non-multipath environment. The state vector matrix \mathbf{X} in the KPLL model (\mathbf{X}^T_{KPLL}) is a 4×1 matrix modeling the carrier phase components, and the accumulated amplitude:

$$\mathbf{X}^T_{KPLL} = [A_0 \ \delta\phi_0 \ \delta f \ \delta a] \quad (3.48)$$

In the KPDLL (KLOS) structure, both carrier and code tracking loops are implemented as a single EKF for a non-multipath environment. The state vector matrix \mathbf{X}^T_{KLOS} is therefore a 5×1 matrix modeling the carrier phase components, accumulated amplitude, as well as the code phase component:

$$\mathbf{X}^T_{KLOS} = [A_0 \ \delta\phi_0 \ \delta f \ \delta a \ \delta\tau_0] \quad (3.49)$$

The amplitude (A_0) dynamics and carrier phase dynamics are modeled as follows:

$$\dot{A}_0 = \omega_A \quad (3.50)$$

where ω_A is a zero mean Gaussian process, and

$$\begin{aligned} \dot{\delta\phi} &= \delta f + \omega_\phi \\ \dot{\delta f} &= \delta a + \omega_f \\ \dot{\delta a} &= \omega_a \end{aligned} \quad (3.51)$$

where ω_ϕ , ω_f and ω_a are uncorrelated zero mean Gaussian processes.

The code Doppler is modeled as

$$\delta\dot{\tau}_0 = \beta \times \delta f \quad (3.52)$$

where β is a coefficient which relates units of chips to cycles.

As \mathbf{X}^T_{KLOS} contains all the states for tracking a LOS signal, it is also called \mathbf{X}^T_{LOS} . The

state transition equation is then given by

$$\mathbf{X}^T_{LOS\ k+1} = \Phi_{LOS} \mathbf{X}^T_{LOS\ k} + \mathbf{W}_k \quad (3.53)$$

The discrete-time transition matrix (Φ_{LOS}) for the KLOS model can be derived from

Eqs.3.50, 3.51 and 3.52 as

$$\Phi_{LOS} = \begin{bmatrix} 1 & 0 & 0 & 0 & 0 \\ 0 & 1 & \delta T & \frac{1}{2} \delta T^2 & 0 \\ 0 & 0 & 1 & \delta T & 0 \\ 0 & 0 & 0 & 1 & 0 \\ 0 & 0 & \beta \delta T & \frac{1}{2} \beta \delta T^2 & 1 \end{bmatrix} \quad (3.54)$$

The measurement vector (\mathbf{Z}) elements are the conventional early, prompt, and late correlator outputs:

$$\begin{aligned} \mathbf{Z}^T &= [I_{\Delta 1} \ Q_{\Delta 1} \ I_{\Delta 2} \ Q_{\Delta 2} \ I_{\Delta 3} \ Q_{\Delta 3}] \\ &= [I_P \ Q_P \ I_E \ Q_E \ I_L \ Q_L] \end{aligned}$$

$$\begin{aligned} I_{\Delta m} + j Q_{\Delta m} &= d_{NAV} A_{LOS} \text{Sinc}(\delta f T) R(\delta \tau_0 + \Delta_m) \text{Cos}(\delta \hat{\Phi}_0) \\ &\quad + j d_{NAV} A_{LOS} \text{Sinc}(\delta f T) R(\delta \tau_0 + \Delta_m) \text{Sin}(\delta \hat{\Phi}_0) \\ &= d_{NAV} A_0 R(\delta \tau_0 + \Delta_m) \text{Cos}(\delta \hat{\Phi}_0) \\ &\quad + j d_{NAV} A_0 R(\delta \tau_0 + \Delta_m) \text{Sin}(\delta \hat{\Phi}_0) \quad m = 1, 2, 3 \end{aligned} \quad (3.55)$$

H Matrix calculation

Since the relation between states and the measurements is non-linear, the h function should be linearised in order to obtain $\mathbf{H}^{[1]}_k$ elements as

$$\mathbf{Z}_k = h_k(\mathbf{X}_k) + \mathbf{V}_k \quad (3.56)$$

$$\mathbf{H}^{[1]}_k \approx \left. \frac{\partial h_k}{\partial \mathbf{X}} \right|_{\mathbf{x}_{k|k-1}} = [h_{i,j}] \quad (3.57)$$

$$h_{i,j} = \frac{\partial \hat{Z}[i]}{\partial X[j]_{k|k-1}} \quad (3.58)$$

$$\begin{aligned} \hat{\mathbf{Z}}^T &= [\hat{I}_{\Delta_1} \hat{Q}_{\Delta_1} \hat{I}_{\Delta_2} \hat{Q}_{\Delta_2} \hat{I}_{\Delta_3} \hat{Q}_{\Delta_3}] \\ \hat{I}_{\Delta} &= \hat{d}_{NAV} \hat{A} R (\delta\hat{\tau} + \Delta) \text{Cos}(\delta\hat{\Phi}_0) \\ \hat{Q}_{\Delta} &= \hat{d}_{NAV} \hat{A} R (\delta\hat{\tau} + \Delta) \text{Sin}(\delta\hat{\Phi}_0) \end{aligned} \quad (3.59)$$

Knowledge of the data bit sign (d_{NAV}), amplitude (A), code phase error ($\delta\tau$), and average carrier phase error ($\delta\Phi_0$) is needed to calculate the H matrix elements for each iteration. \hat{d}_{NAV} , \hat{A} and $\delta\hat{\Phi}_0$ are obtained as described before in Section 3.3.1. The code phase error estimate ($\delta\hat{\tau}$) is also provided by the fifth state of \mathbf{X} :

$$\begin{aligned} \hat{A} &= X[1]_{k|k-1} \quad \text{a priori estimate} \\ \delta\hat{\phi} &= X[2]_{k|k-1} \\ \delta\hat{f} &= X[3]_{k|k-1} \\ \delta\hat{\alpha} &= X[4]_{k|k-1} \\ \delta\hat{\Phi} &= \delta\hat{\phi} + \frac{1}{2} \delta T \delta\hat{f} + \frac{1}{6} \delta T^2 \delta\hat{\alpha} \\ \delta\hat{\tau} &= X[5]_{k|k-1} \end{aligned} \quad (3.60)$$

The partial derivatives of the in-phase observations relative to the Kalman states are formulated as

$$\begin{aligned}
\frac{\partial I_{\Delta}}{\partial A} &= \hat{d}R(\hat{\tau} + \Delta) \text{Cos}(\delta\hat{\Phi}) \\
\frac{\partial I_{\Delta}}{\partial \delta\phi} &= -\hat{d}\hat{A}R(\hat{\tau} + \Delta) \text{Sin}(\delta\hat{\Phi}) \\
\frac{\partial I_{\Delta}}{\partial \delta f} &= -\left(\frac{1}{2} \delta T\right) \hat{d}\hat{A}R(\hat{\tau} + \Delta) \text{Sin}(\delta\hat{\Phi}) \\
\frac{\partial I_{\Delta}}{\partial \delta\alpha} &= -\left(\frac{1}{6} \delta T^2\right) \hat{d}\hat{A}R(\hat{\tau} + \Delta) \text{Sin}(\delta\hat{\Phi}) \\
\frac{\partial I_{\Delta}}{\partial \delta\tau} &= \hat{d}\hat{A}\hat{R}(\hat{\tau} + \Delta) \text{Cos}(\delta\hat{\Phi})
\end{aligned} \tag{3.61}$$

3.4.2 KLOS verification using the real data

In this sub-section, an analysis of the KLOS performance is shown. KLOS is verified by real data collected from an antenna mounted on a pillar on the roof of the CCIT building at the University of Calgary.

3.4.2.1 In-phase and Quadrature phase correlator outputs

The performance of the carrier phase tracking can be evaluated by analyzing the I and Q correlator outputs. In a perfect carrier phase lock situation, the total signal energy is in the I arm and Q doesn't contain any signal power and hence should consist of a zero mean white Gaussian noise process. The I values contain signal power plus a zero mean white Gaussian noise. So the I distribution should be a Gaussian with non-zero mean with a mean value equivalent to the mean signal amplitude, and the Q distribution should be Gaussian with zero mean. As the I values are modulated by data bits, the I distribution

consists of two non-zero mean Gaussian distributions centered at plus and minus the signal amplitudes. These are the characteristics of a perfect phase lock. Figures 3.5 and 3.6 show these desired characteristics for the KLOS tracking loop.

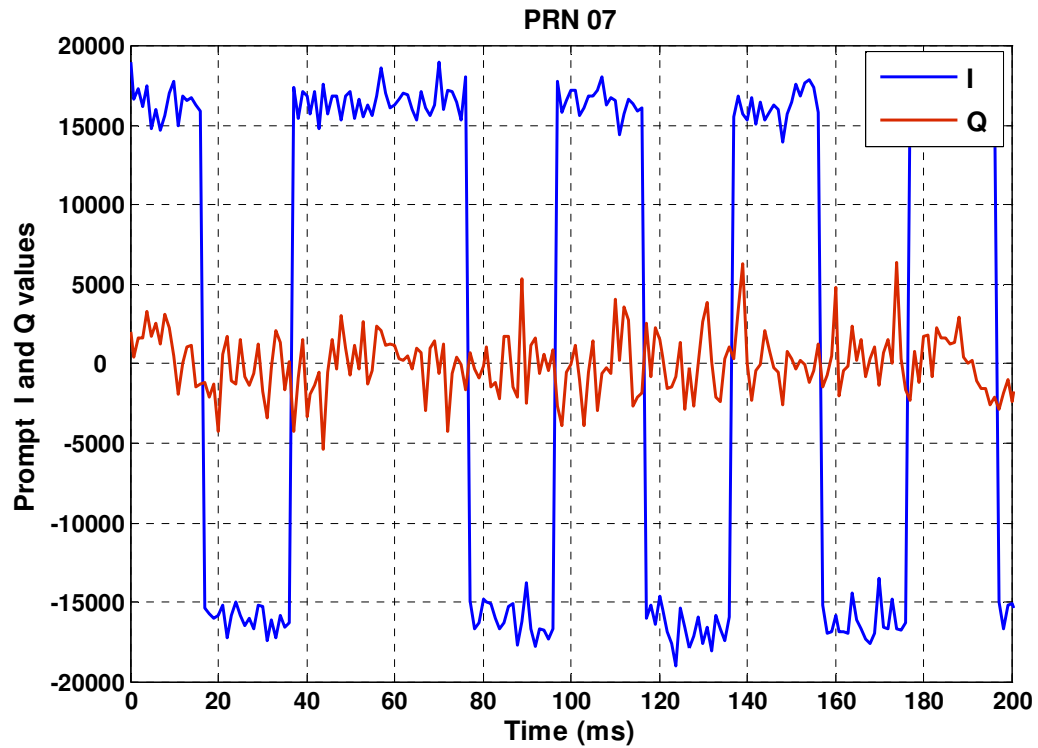


Figure 3.5: I and Q values in the KLOS loop structure

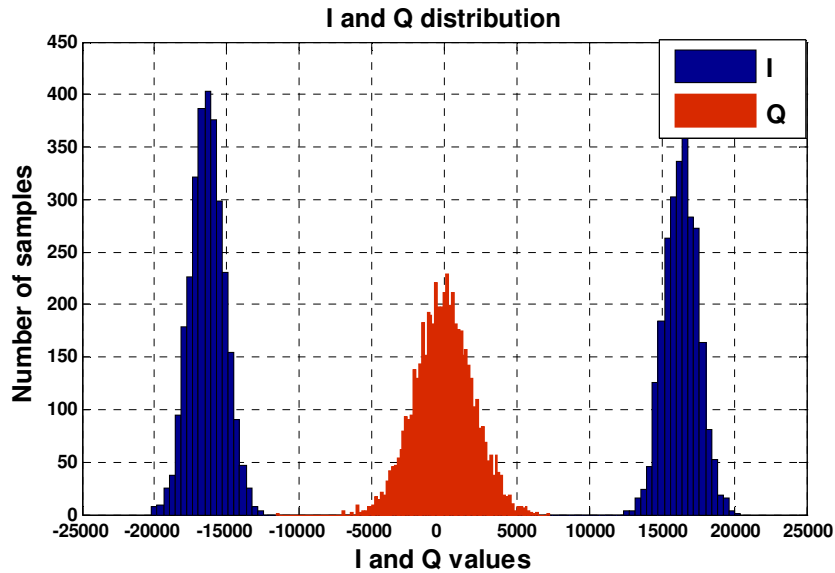


Figure 3.6: I and Q distributions in the KLOS loop structure

3.4.2.2 Kalman gain analysis

In the conventional tracking loop, the loop bandwidth is a key parameter which shows the loop response to the signal dynamics and the input noise level. Similarly in the KLOS loop structure, state estimation bandwidth can be defined. A higher state estimation bandwidth allows the filter to track higher dynamics, but this also increases the total noise power entered into the states. Changes in the Kalman filter estimation bandwidth during state estimation can be investigated from its corresponding Kalman gain. In this sub-section, the Kalman filter state estimation bandwidth change in the amplitude estimation is investigated. In the KLOS architecture, the Kalman gain matrix (\mathbf{K}) is a 5×6 vector in which the i -th ($i=1, \dots, 5$) row corresponds to the i -th Kalman state, and j -th ($j=1, \dots, 6$) column corresponds to the Kalman gain for the j -th measurement. The Kalman gain corresponding to the prompt in-phase correlator

output and amplitude state is the first element in the \mathbf{K} matrix ($i = 1, j = 1$). This element is plotted over time in Figure 3.7. It can be seen that the Kalman gain for the amplitude has decreased over time as the estimated amplitude has converged to its true value. Figure 3.8 shows the estimated amplitude error standard deviation, which corresponds to the first element in the \mathbf{P} matrix ($i = 1, j = 1$). $P(1,1)$ is also decreasing over time when the estimated amplitude converges to its true value. As Figures 3.7 and 3.8 reveal, there is a relationship between Kalman gain and state estimation bandwidth.. The equivalent filter state estimation bandwidth was initially large to let the estimated amplitude reach its true value and then decreased to prevent noise from entering into the state estimates. The Kalman bandwidth has adaptively changed from a higher value to a lower value, thereby enabling the initial “pull-in” of the amplitude estimate, while still allowing low noise estimates in steady-state.

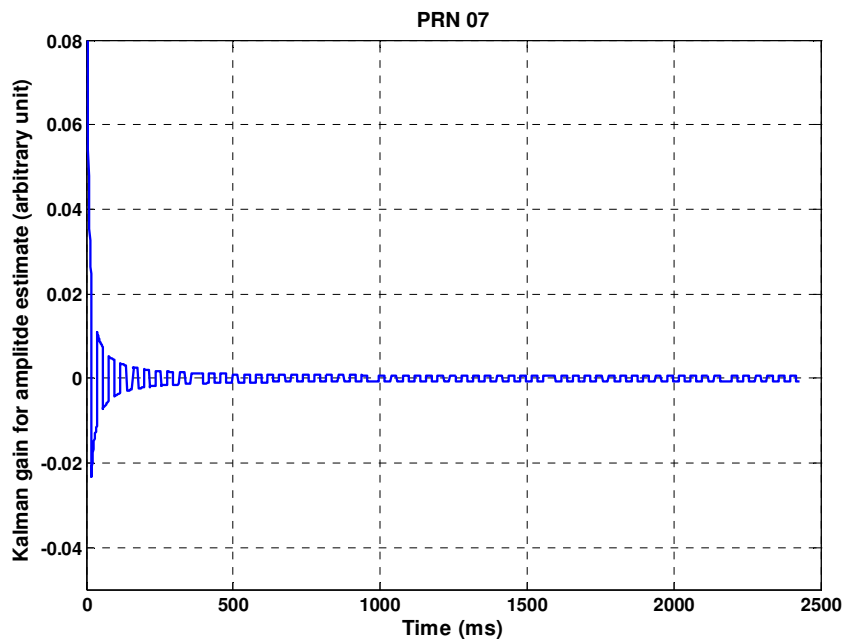


Figure 3.7: Kalman gain for PRN 07 amplitude estimate

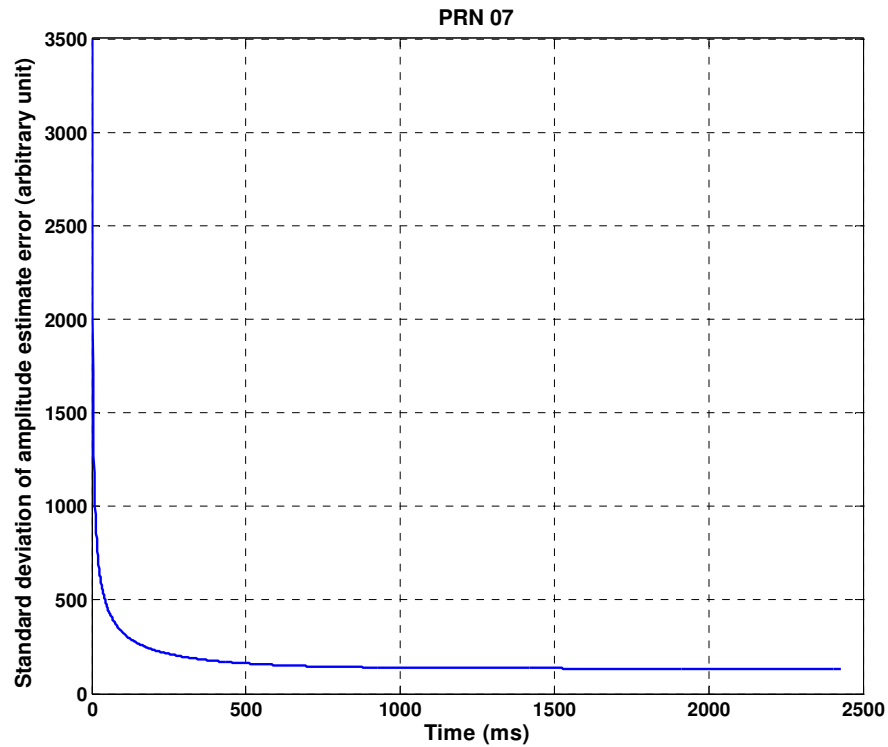


Figure 3.8: Amplitude estimation error variance

3.4.2.3 P matrix analysis

The diagonal elements of the \mathbf{P} matrix are the estimated error variances of the states. The diagonal elements corresponding to the second, third, fourth and fifth states, which are the carrier phase error ($\delta\phi_0$), carrier Doppler error (δf), carrier Doppler rate error (δa) and code phase error ($\delta\tau_0$) respectively, are plotted in Figure 3.9. These values show the expected precision of the state estimation.

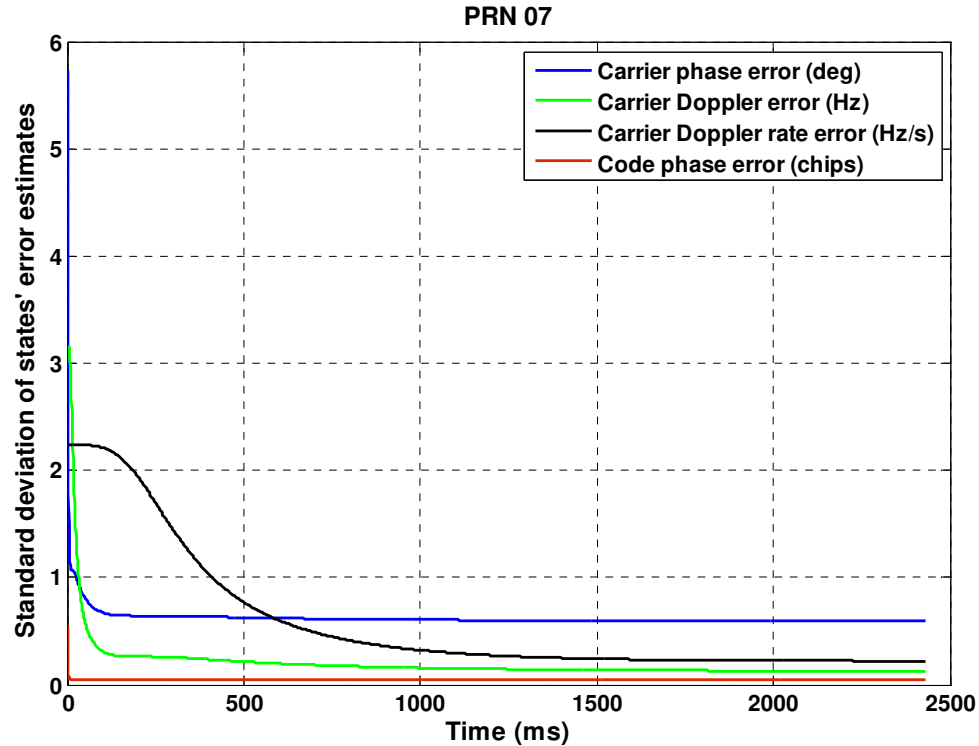


Figure 3.9: 4 Kalman states estimation error variance

The carrier phase error uncertainty started at 60 degrees at the beginning and then converged to 0.59 degrees. The carrier Doppler error uncertainty has started at 3 Hz and converged to 0.12 Hz. The carrier Doppler rate error uncertainty initial value is 2.2 Hz/s and converged to 0.22 Hz/s. The code phase error uncertainty started at 0.54 chips and converged to 0.048 chips. Comparing these values with standard deviation of the estimates shows that the filter states have converged to their final values with an acceptable precision. Since the Doppler rate error is not directly observable by the measurements, it has converged to its steady-state value much slower than the other states.

3.5 Received GPS signal modeling in a specular multipath environment

The KLOS structure was designed in for a non-multipath environment. The KLOS model can be extended to the Kalman multipath (KMP) structure in order to account for the extra multipath components embedded in the received signal. The KMP scheme will be explained in Section 3.6 after the received signal in a specular multipath is described herein. As was shown in Chapter 2, the transmitted GPS L1 C/A signal can be written as

$$S(t) = \sqrt{2P(t)}d_{NAV}(t)\text{Cos}(2\pi ft + \theta'_0)PRN(t), \quad (3.62)$$

where $P(t)$ is the signal power, d_{NAV} is the navigation bit, f is the GPS signal RF carrier frequency, and $PRN(t)$ is the C/A code sequence. θ'_0 is the transmitted signal carrier phase. In a specular multipath environment, the channel can be modeled as (Iltis 1999)

$$h(\tau, t) = \sum_{n=0}^{n=N_{mp}} f_n(t) \delta(\tau - \tau_n), \quad (3.63)$$

where $N_{mp}+1$ received paths are assumed. $f_n(t)$ is the complex-valued channel coefficient for the n -th path modeling all the amplitude and phase changes in $S(t)$ during the transmission, and τ_n shows the delay for the n -th path. The received RF signal can then be written as

$$R(t) = \sum_{n=0}^{n=N_{mp}} |f_n| \sqrt{2P(t - \tau_n)} d_{NAV}(t - \tau_n) \quad (3.64)$$

$$\text{Cos}(2\pi[f + \delta f_{(t - \tau_n)}]t + [\theta'_n + \angle f_n])PRN(t - \tau_n)$$

where $\delta f_{(t - \tau_n)}$ is the instantaneous Doppler frequency of the LOS signal due to relative motion of the satellite and receiver. In general, all paths can have different Doppler frequencies. The bandwidth spread of these frequencies is called fading bandwidth. For stationary reflector-receiver cases, the fading bandwidth is determined by the satellite

geometry change during the observation which is usually much smaller than 1 Hz (Van Nee 1993). A Doppler difference of 1 Hz in a loop with TCOH = 1ms introduces 0.36° phase change. Hence, the small Doppler difference between multipath and the LOS signal can be absorbed in the multipath phases (θ_n $n = 1, \dots, N_{mp}$), and all paths will be assumed to have the same Doppler frequency.

As was shown in Section 2.5.1, the in-phase and quadrature outputs ($I_{\Delta_m}, Q_{\Delta_m}$) for the m -th correlator can be written as

$$I_{\Delta_m} = d_{NAV} A_0 R(\delta\tau_0 + \Delta_m) \text{Sinc}(\delta f T) \text{Cos}(\delta\hat{\Phi}_0) + \sum_{n=1}^{N_{mp}} d_{NAV} A_n R(\delta\tau_0 + \Delta_m + \tau_n) \text{Sinc}(\delta f T) \text{Cos}(\delta\hat{\Phi}_n) \quad (3.65)$$

$$Q_{\Delta_m} = d_{NAV} A_0 R(\delta\tau_0 + \Delta_m) \text{Sinc}(\delta f T) \text{Sin}(\delta\hat{\Phi}_0) + \sum_{n=1}^{N_{mp}} d_{NAV} A_n R(\delta\tau_0 + \Delta_m + \tau_n) \text{Sinc}(\delta f T) \text{Sin}(\delta\hat{\Phi}_n) \quad (3.66)$$

A_n ($0 < n < N_{mp}$) is the n -th path accumulated amplitude during the integration period T .

$\delta\tau_0$ is the code phase bias between the locally generated code and the incoming LOS signal, and δf is the frequency error between locally generated and the incoming signal.

$\delta\hat{\Phi}_n$ is the average phase error over the integration interval for the n -th signal component which was modeled previously in Eqs. 2.34 and 2.35.

3.6 RAKE-like multi-correlator structure (KMP structure)

The proposed KMP tracking loop has a multi correlator structure (Jee et al 2002, Fishler & Bobrovsky 1999), as illustrated in Figure 3.10. In contrast to a conventional tracking loop, which uses three versions of the code replicas (prompt, early and late correlators), the KMP uses extra correlators for estimating the extra signal components (multipath components). Since the multipath components with relative code delays less than one chip period are of interest, sub-chip correlator spacing spanning from -1 chip to 1 chip is performed in the code generator. The correlator outputs after accumulation form the I and Q measurements which are then fed into the KMP estimator. The KMP estimates (tracks) the LOS signal components as well as the multipath signal components. The LOS signal components are further used for updating the code and carrier NCOs in each loop iteration.

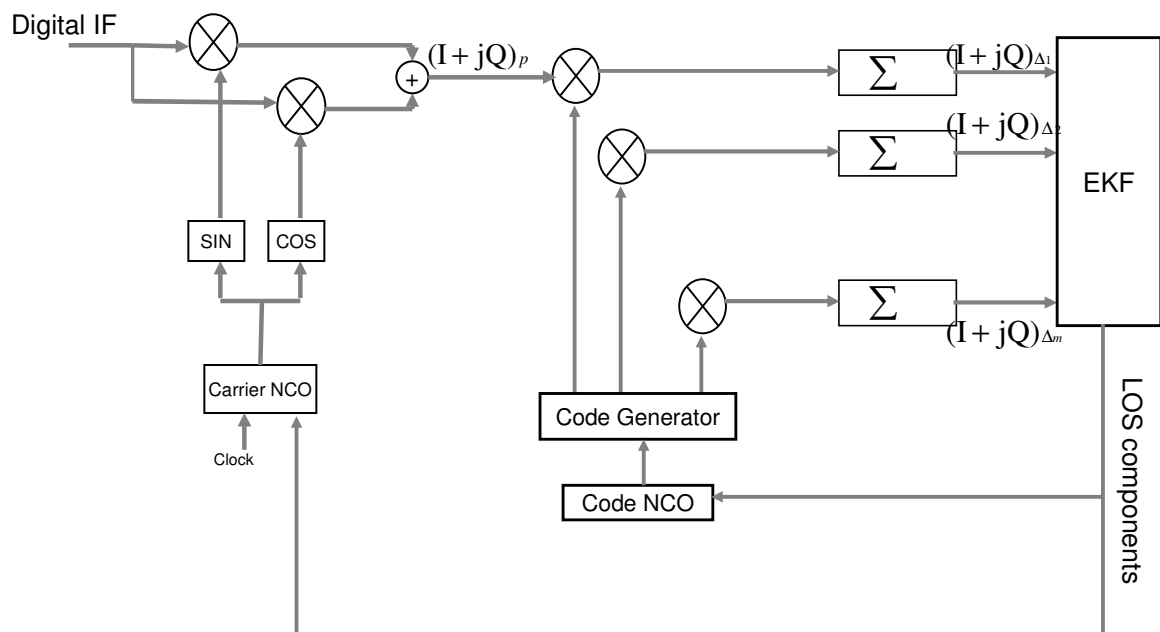


Figure 3.10: Multi-correlator with EKF structure

The KLOS model was designed for a non-multipath environment. It is not matched with a multipath scenario in which N_{mp} extra paths are added to the LOS received signal. These additional signal components are modeled in the Kalman Multipath (KMP) model. The KMP state vector \mathbf{X} consists of two sub vectors \mathbf{X}_{LOS} and \mathbf{X}_{MP} . \mathbf{X}_{LOS} was modeled in Section 3.4.1, and its corresponding transition matrix (Φ_{LOS}) is shown by Eq.3.54.

3.6.1 KMP implementation

Since the GPS signal is received through a multipath environment, there are unknown LOS as well as multipath components in the measurements which should be estimated. Let us introduce \mathbf{X} as the total state vector to be estimated in each integration period through the Kalman Filter:

$$\begin{aligned}\mathbf{X}^T &= [\mathbf{X}_{LOS}^T \mathbf{X}_{MP}^T] \\ \mathbf{X}_{LOS}^T &= [A_0 \delta\phi_0 \mathcal{F} \delta\alpha \delta\tau_0] \\ \mathbf{X}_{MP}^T &= [A_1 \delta\phi_1 \tau_1 \dots A_{N_{mp}} \delta\phi_{N_{mp}} \tau_{N_{mp}}]\end{aligned}\tag{3.67}$$

where \mathbf{X}_{LOS}^T is a 5×1 vector containing the LOS signal components and \mathbf{X}_{MP}^T is a $(3N_{mp}) \times 1$ vector for the multipath states. The correlator outputs contain information about the signal components and are used as inputs to the EKF estimator. They are shown as the measurement vector \mathbf{Z} which is a $m \times 1$ vector:

$$\mathbf{Z} = [I_{\Delta_0} Q_{\Delta_0} \dots I_{\Delta_m} Q_{\Delta_m}],\tag{3.68}$$

where $I_{\Delta_m} + jQ_{\Delta_m}$ is the m -th correlator output.

Generally, a higher number of correlators results in a more accurate state estimation, but it also increases the computational load. The least number of correlators and m is

determined by the state vector dimension n . In order to have a unique solution for the Kalman filter states, the following condition applies:

$$m \geq n, \quad n = 5 + 3 \times N_{mp} \quad (3.69)$$

Once the system and measurement models are defined, a Kalman filter can be implemented to estimate the states \mathbf{X} from the noisy measurements \mathbf{Z} . The system dynamics and measurement models can be written as Eqs. 3.1 and 3.2 respectively.

\mathbf{X}_{MP}^T is a $(3N_{mp}) \times 1$ vector and each path introduces three elements to this vector. These three elements for the n -th path are amplitude, phase, and relative code delay, modeled as

$$\begin{aligned} \dot{A}_n &= -\beta_{A_n} A_n + \omega_{A_n} \\ \delta \dot{\phi}_n &= \delta f + \omega_{\phi_n} \\ \dot{\tau}_n &= -\beta_{\tau_n} \tau_n + \omega_{\tau_n} \quad n = 1, \dots, N_{mp} \end{aligned} \quad (3.70)$$

where ω_{A_n} , ω_{ϕ_n} and ω_{τ_n} are uncorrelated zero mean Gaussian processes corresponding to the n -th multipath amplitude, carrier and code phases respectively.

The discrete-time description of the multipath state dynamics can be derived from Eq.3.70 as

$$\begin{aligned} A_{n,k+1} &= \alpha_{A_n} A_{n,k} + W_{A_n} \\ \delta \phi_{n,k+1} &= \delta \phi_{n,k} + \delta f \delta T + \frac{1}{2} \delta T^2 \delta \alpha + W_{\delta \phi_n} \\ \tau_{n,k+1} &= \alpha_{\tau_n} \tau_{n,k} + W_{\tau_n} \end{aligned} \quad (3.71)$$

The multipath amplitude (A_n) and relative code delay (τ_n) are modeled as Gauss-Markov process. The Gauss-Markov parameters for these states are set as follows, which correspond to nearly constant channel coefficients and constant delay (Iltis 1999):

$$\begin{aligned}
\alpha_{A_n} &= e^{-\beta_{A_n} \delta T} \quad ; \quad \beta_{A_n} = 10.05 \\
\alpha_{\tau_n} &= e^{-\beta_{\tau_n} \delta T} \quad ; \quad \beta_{\tau_n} = 10.05
\end{aligned}
\tag{3.72}$$

Therefore, the total transition matrix for Nmp=1 case can be written as

$$\begin{bmatrix}
1 & 0 & 0 & 0 & 0 & 0 & 0 & 0 \\
0 & 1 & \delta T & \frac{1}{2} \delta T^2 & 0 & 0 & 0 & 0 \\
0 & 0 & 1 & \delta T & 0 & 0 & 0 & 0 \\
0 & 0 & 0 & 1 & 0 & 0 & 0 & 0 \\
0 & 0 & \beta \delta T & \frac{1}{2} \beta \delta T^2 & 1 & 0 & 0 & 0 \\
0 & 0 & 0 & 0 & 0 & \alpha_{A_1} & 0 & 0 \\
0 & 0 & \delta T & \frac{1}{2} \delta T^2 & 0 & 0 & 1 & 0 \\
0 & 0 & 0 & 0 & 0 & 0 & 0 & \alpha_{\tau_1}
\end{bmatrix}
\tag{3.73}$$

Modeling H:

As Eqs. 3.65 and 3.66 show, the observation matrix is non-linearly related to the state matrix through \hat{h} as

$$\mathbf{Z} = \hat{h}(\mathbf{X}) \tag{3.74}$$

$$\mathbf{Z} = [I_{\Delta_0} \ Q_{\Delta_0} \ \dots \ I_{\Delta_m} \ Q_{\Delta_m}]$$

Since \mathbf{Z} is a non-linear function of \mathbf{X} , \hat{h} should be linearised around $\hat{\mathbf{X}}_{k|k-1}$ (the priori estimate of \mathbf{X}) for each filter iteration. The \mathbf{H} matrix, which is the linearised version of \hat{h} is calculated in each iteration by

$$\begin{aligned}
\mathbf{H} &= [h_{i,j}] \\
h_{i,j} &= \left. \frac{\partial Z[i]}{\partial X[j]} \right|_{\hat{\mathbf{X}}_{k|k-1}}
\end{aligned}
\tag{3.75}$$

The following equations show the partial derivatives of the In-phase observations relative to the LOS states:

$$\begin{aligned}
\frac{\partial I_{\Delta_m}}{\partial A_0} &= \hat{d}R(\delta\hat{\tau}_0 + \Delta_m) \text{Cos}(\delta\hat{\Phi}_0) \\
\frac{\partial I_{\Delta_m}}{\partial \delta\phi_0} &= -\hat{d}\hat{A}_0 R(\delta\hat{\tau}_0 + \Delta_m) \text{Sin}(\delta\hat{\Phi}_0) \\
\frac{\partial I_{\Delta_m}}{\partial \delta f} &= -\left(\frac{1}{2} \delta T\right) \hat{d}\hat{A}_0 R(\delta\hat{\tau}_0 + \Delta_m) \text{Sin}(\delta\hat{\Phi}) \\
&\quad - \sum_{n=1}^{N_{mp}} \left(\frac{1}{2} \delta T\right) \hat{d}\hat{A}_n R(\delta\hat{\tau}_0 + \tau_n + \Delta_m) \text{Sin}(\delta\hat{\Phi}_n) \\
\frac{\partial I_{\Delta_m}}{\partial \delta\alpha} &= -\left(\frac{1}{6} \delta T^2\right) \hat{d}\hat{A}_0 R(\delta\hat{\tau}_0 + \Delta_m) \text{Sin}(\delta\hat{\Phi}) \\
&\quad - \sum_{n=1}^{N_{mp}} \left(\frac{1}{6} \delta T^2\right) \hat{d}\hat{A}_n R(\delta\hat{\tau}_0 + \tau_n + \Delta_m) \text{Sin}(\delta\hat{\Phi}_n) \\
\frac{\partial I_{\Delta_m}}{\partial \delta\tau_0} &= \hat{d}\hat{A}\dot{R}(\delta\hat{\tau}_0 + \Delta_m) \text{Cos}(\delta\hat{\Phi}_0) \\
&\quad + \sum_{n=1}^{N_{mp}} \hat{d}\hat{A}_n \dot{R}(\delta\hat{\tau}_0 + \tau_n + \Delta_m) \text{Cos}(\delta\hat{\Phi}_n)
\end{aligned} \tag{3.76}$$

The partial derivatives of the In-phase observations relative to the n-th multipath states are formulated as

$$\begin{aligned}
\frac{\partial I_{\Delta_m}}{\partial A_n} &= \hat{d}R(\delta\hat{\tau}_0 + \tau_n + \Delta_m) \text{Cos}(\delta\hat{\Phi}_n) \\
\frac{\partial I_{\Delta_m}}{\partial \delta\phi_n} &= -\hat{d}\hat{A}_n R(\delta\hat{\tau}_0 + \tau_n + \Delta_m) \text{Sin}(\delta\hat{\Phi}_n) \\
\frac{\partial I_{\Delta_m}}{\partial \delta\tau_n} &= \hat{d}\hat{A}_n \dot{R}(\delta\hat{\tau}_0 + \tau_n + \Delta_m) \text{Cos}(\delta\hat{\Phi}_n) \quad , n = 1, \dots, N_{mp}
\end{aligned} \tag{3.77}$$

3.7 Primary-Secondary structure for RHCP/LHCP Data

GPS signals collected by an RHCP/LHCP antenna provide two data sets. To process the RHCP and LHCP data sets, a specific tracking loop structure is proposed and described

herein. This structure is called primary-secondary structure as there is one primary closed loop followed by a secondary open loop. The primary loop is the standard code and carrier tracking loop explained in Section 3.1. In contrast to the primary loop, the secondary loop is an open loop. Tracking information used for generating the LHCP locally generated signal is updated by the primary loop instead of being obtained from the secondary loop filter. The secondary open loop outputs the accumulated I and Q values obtained from the correlation of LHCP data and the LHCP locally generated signal. These accumulated I and Q values can then be used for multipath monitoring and analyses such as LHCP relative multipath phase changes and the LHCP autocorrelation function.

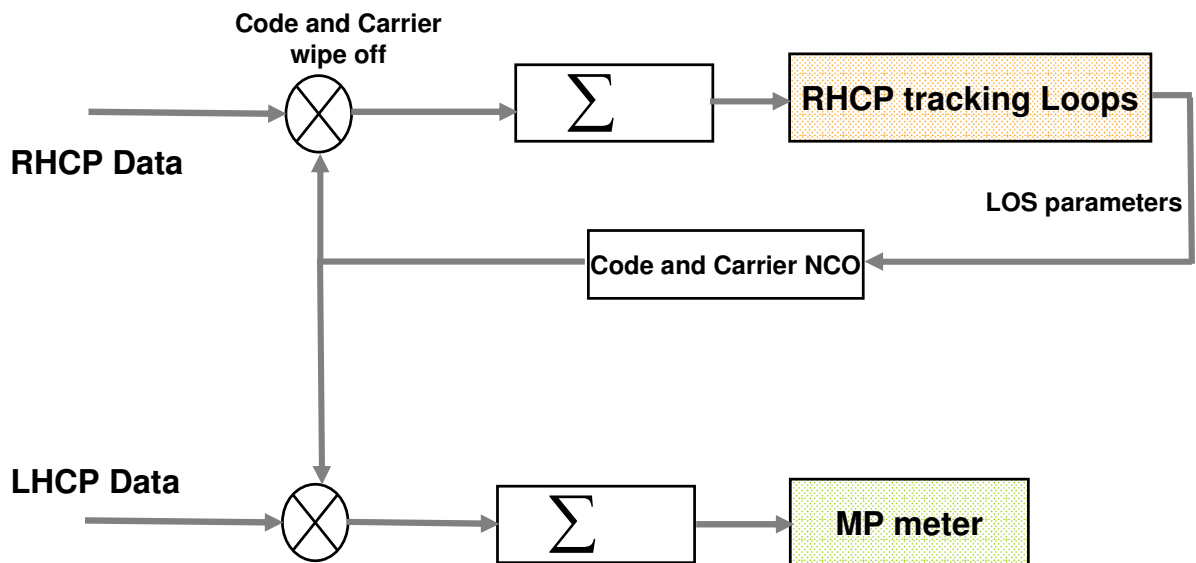


Figure 3.11: Primary-secondary structure

3.7.1 Primary-secondary implementation in the GSNRx™ software

There is one input file for the GSNRx™ software receiver, and all processing procedures are applied to this file. One sample reader object is defined from the

GSRx™ option file class which determines the sample type (real or complex), sample size, IF frequency and sampling rate for the GPS raw data to be read by the software. There is also one Doppler Removal and correlation (DRC) object defined for the channels, which performs Doppler Removal and correlation for each channel. Since two GPS raw data are simultaneously processed in the primary-secondary structure, two input files should be defined in the option file, and two sample reader and DRC objects should also be assigned for the channels. The RHCP data has its own sample reader (SampleReader_RHCP) and DRC object (DRC_RHCP) while the LHCP data has also its own sample reader (SampleReader_LHCP) and DRC (DRC_LHCP) objects. As previously discussed, the secondary open loop uses primary tracking information for generating the secondary local replica signal. So the primary tracking information should always be copied to the secondary structure for each processing step. This copying procedure is done in two phases. First in the channel initialization where all initial tracking information provided from the acquisition step as well as other information such as signal IF frequency, sampling rate and sample size, are copied from the primary trackingData object to the SecondaryTrackingData object. Secondly, after each loop update, just tracking information, which are the carrier phase, carrier Doppler, code phase, and code Doppler, are copied from the trackingData object to the SecondaryTrackingData object.

The secondary local replica which is generated from the copied SecondaryTrackingData object is then used with the LHCP raw GPS data in the Doppler removal and correlation process to produce In-phase (I) and Quadrature phase (Q) samples. These I and Q values

after 1 ms to 20 ms accumulation are copied into the SecondaryTrackingData object to form the secondary loop I and Q values. Figure 3.12 summarizes the primary/secondary implementation scheme in the GSNRx™ software.

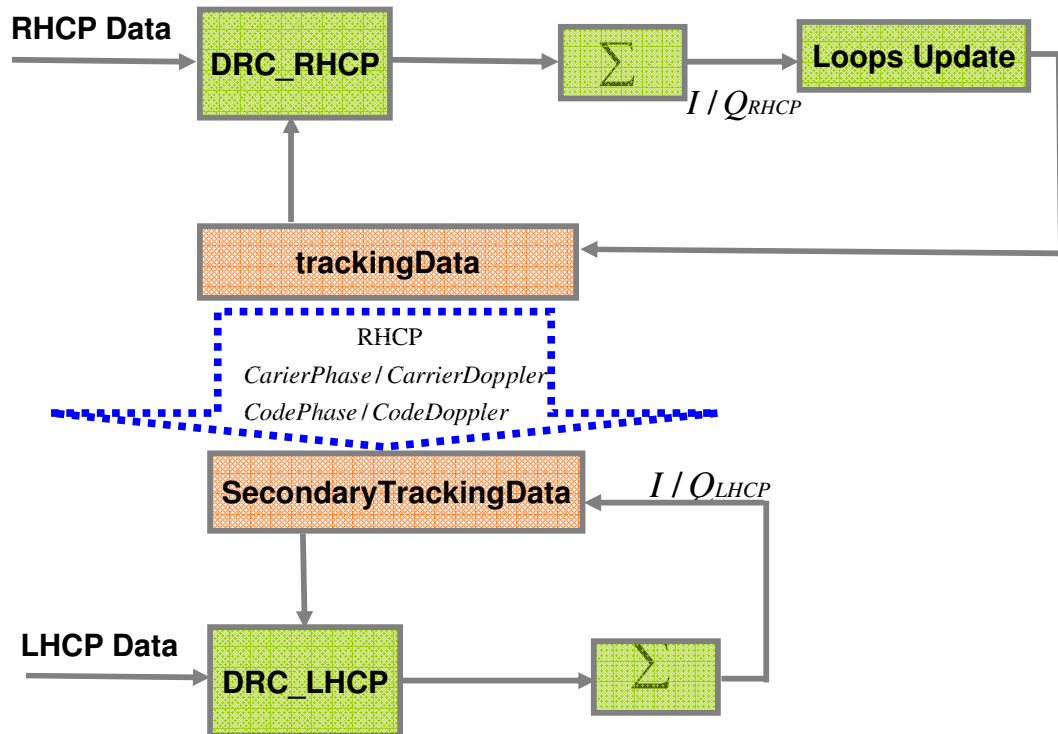


Figure 3.12: Primary-secondary implementation scheme in the GSNRx™ software

3.7.2 Verifying the primary-secondary structure with real data

In order to verify the primary-secondary structure, a data collection was performed. As Figure 3.13 indicates, the GPS signals were collected from a roof pillar antenna. The antenna output was split into two parts and then each part was fed to the digital front-end after passing through an external low noise amplifier (LNA).

Two synchronized RF channels in the front-end were assigned to these two data sets for down-converting and digitizing the original RF signal. The resultant digital IF signals were saved on an external hard drive to be further processed by the primary/secondary structure developed in the software receiver.

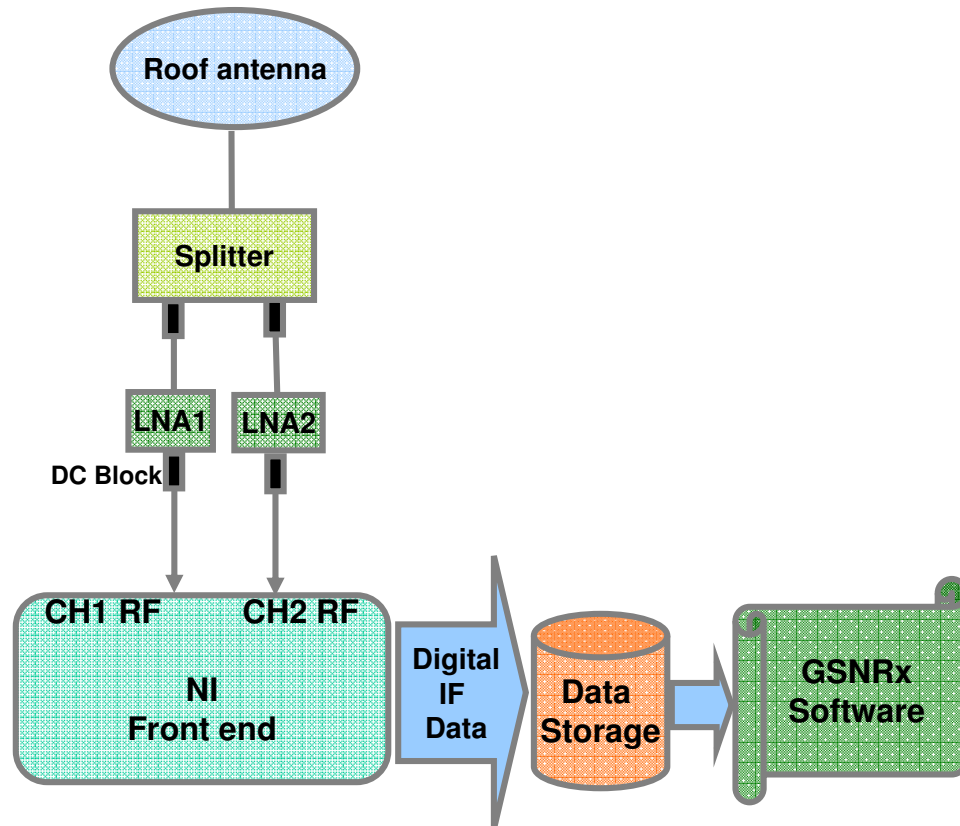


Figure 3.13: Data collection scheme for verifying the primary-secondary structure

The two data sets (primary and secondary data) collected during the test were then processed by the primary/secondary structure to generate primary and secondary accumulated I and Q values. The test was performed three times and three primary/secondary data sets were processed with GSNRx™. Figures 3.14 and 3.15 show the corresponding results for the first and second trial, respectively.

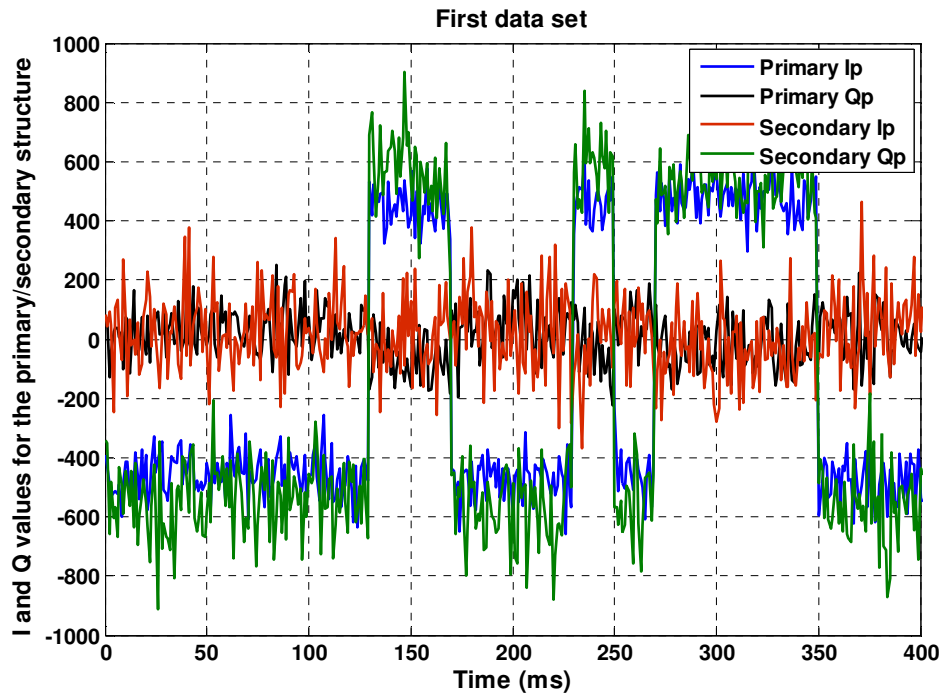


Figure 3.14: Primary and secondary correlator outputs (First trial)

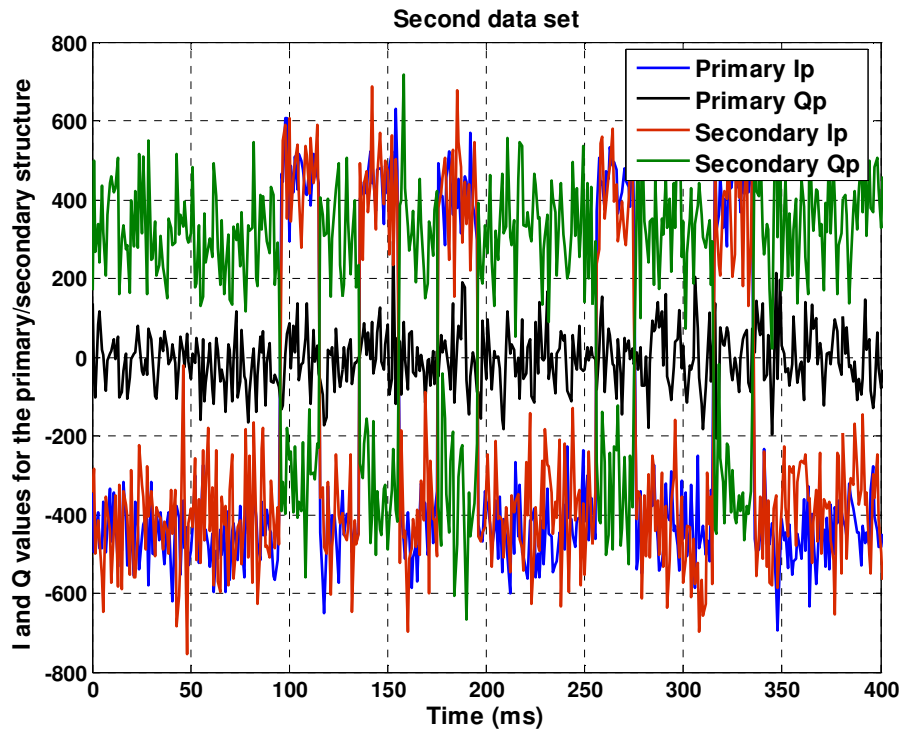


Figure 3.15: Primary and secondary correlator outputs (Second trial)

Table 3.1: Phase bias between primary and secondary channels

Trial number	Phase bias between primary and secondary channels (degrees)
1	90
2	~ 45
3	<45

Four correlator outputs are plotted in each figure, namely the prompt In-phase and Quadrature phase correlator outputs for the primary ($I_p^{\text{primary}}, Q_p^{\text{primary}}$) and the secondary ($I_p^{\text{secondary}}, Q_p^{\text{secondary}}$) loops. As expected, all signal power remains in the I_p^{primary} component and Q_p^{primary} contains no power. In the first trial, $Q_p^{\text{secondary}}$ has absorbed all the signal power while $I_p^{\text{secondary}}$ contains no power, which shows a 90 degree phase bias between the primary and secondary front-end channels. In the second trial, both $I_p^{\text{secondary}}$ and $Q_p^{\text{secondary}}$ have non-zero values and the secondary signal power has been split between the $I_p^{\text{secondary}}$ and $Q_p^{\text{secondary}}$ components. $I_p^{\text{secondary}}$ is in phase with I_p^{primary} , and its absolute value is slightly higher than the $Q_p^{\text{secondary}}$ absolute value. This corresponds to a 40-45 degree phase bias between the primary and secondary front-end channels. The third trial also shows a phase bias of less than 45 degree between the two front-end channels. Therefore the primary-secondary structure shows that there is an unknown but constant random phase mismatch between the front-end channels. This

demonstrates that the primary-secondary structure operates as expected. Analyses of the results in multipath environments are deferred to Chapter 5.

3.8 Summary

This chapter focused on describing the Kalman filter based tracking models for the non-multipath and multipath environments. The Kalman multipath (KMP) algorithm described in this chapter was then implemented in GSNRx™ and applied to both simulated and real multipath signals. The KMP algorithm results along with primary-secondary structure output analyses and other multipath parameterization results are presented in the next chapters.

Chapter Four: Analysis of the KMP Technique

This chapter focuses on the parameterization of the multipath environment using the techniques described in Chapter 3. It begins with an investigation of the KMP algorithm performance in a simulated multipath environment. The multipath signal is simulated using a Spirent GSS 7700 Hardware Simulator (Spirent 2006). The KMP technique is verified under different Signal-to-Multipath Ratios (SMRs), and multipath relative code delays. A real multipath environment and data collection scheme is then introduced in Section 4.2. LOS and multipath parameters are then estimated through the KMP technique for this multipath environment.

4.1 KMP verification using a GPS hardware simulator

The KMP algorithm is first verified using data from a Spirent GSS 7700 Hardware Simulator. The multipath signal is added to the LOS signal, and the composite RF GPS signals are collected using a National Instruments PXI-5661 RF front-end after passing through an external LNA. The signals undergo down-conversion and digitization in the front-end. The digital IF signals are then saved in an external hard drive to be further processed by the GSNRx™ software receiver (Figure 4.1).

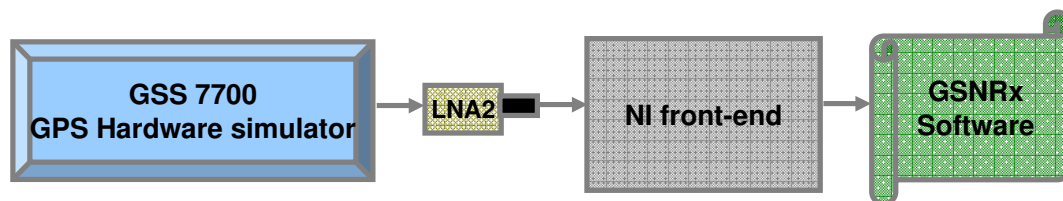


Figure 4.1: Data collection scheme

The KMP algorithm implemented in GSNRx™ is applied to the simulated multipath signals in order to parameterize the simulated multipath environment. Four correlators were used as the KMP input measurements. Figure 4.2 shows the correlator spacing about the prompt correlator. In the following sections, one extra path is assumed in the KMP structure. As Eq. 3.70 implies, four correlators are needed for this structure.

In order to investigate KMP performance with different SMR levels and multipath relative code delays, three scenarios are simulated by the hardware simulator. The KMP algorithm starts after the conventional PLL and DLL have run for 100 ms. The estimate of LOS amplitude, code and carrier phase errors obtained from the original tracking loops provide reasonable initial values for the corresponding KMP states. The KMP algorithm is then applied in each scenario, and the results are analyzed in the next section.

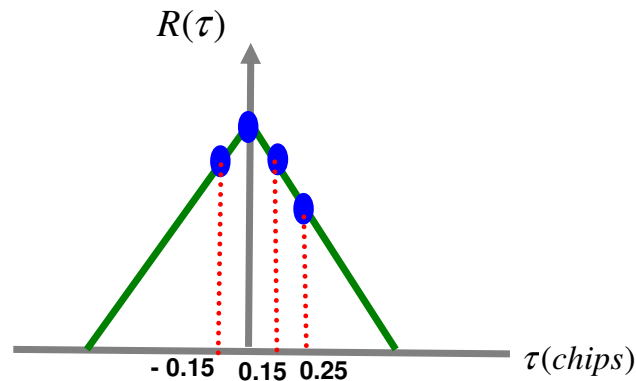


Figure 4.2: Correlator spacing

4.1.1 First scenario

The first simulated scenario contains an extra path spaced 0.5 chips from the LOS signal with a SMR of 6 dB. SMR can be defined as the ratio between the LOS power and the

multipath power and is expressed in decibels. It is a factor for measuring the multipath power embedded in the composite signal and can be measured in real scenarios for monitoring the instantaneous multipath power level. The SMR can be calculated as

$$\text{SMR} = 20\log_{10}\left(\frac{A_0}{A_1}\right). \quad (4.1)$$

In the entire 80 s duration of the test, the LOS signal power is kept constant, but only in the first 43 s is multipath power added to the signal. Figure 4.3 shows the LOS (A_0) and multipath (A_1) amplitudes estimated by the KMP algorithm. The estimated multipath amplitude is half the estimated LOS amplitude in the first 43 s and the estimated LOS amplitude is constant over the whole interval. This verifies that KMP has accurately estimated multipath power from the composite signal.

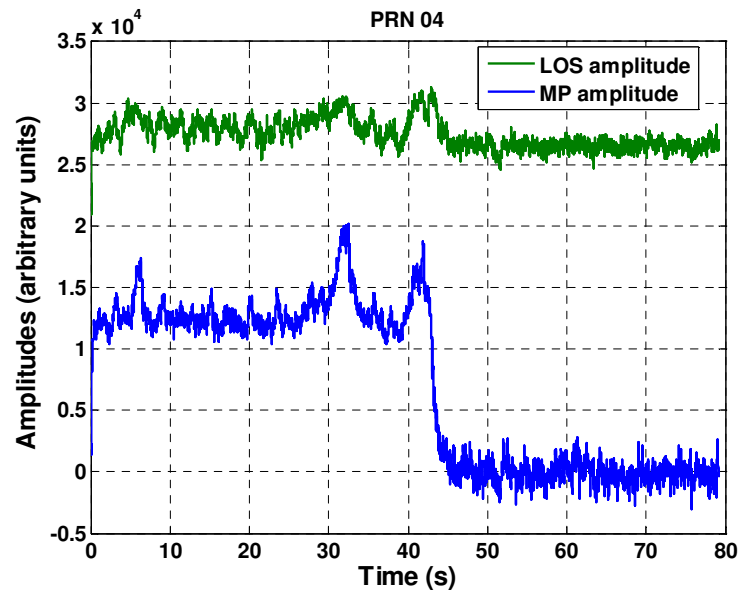


Figure 4.3: LOS and Multipath amplitude for the first scenario

The SMR for this composite signal is estimated using Eq. 4.1 and is shown in Figure 4.4. The RMSE for the first 43 s is 1.7 dB. As Table 4.1 shows, the mean estimated SMR is 7.3 dB for the first 43 s, but it has a very high value (44.3 dB) after the multipath power is switched off in the hardware simulator. Since there is no multipath power in the embedded signal after the first 43 s, the KMP has estimated the mean multipath power as zero. This has made the denominator in Eq. 4.1 to have a small value which is equivalent to high values for the SMR.

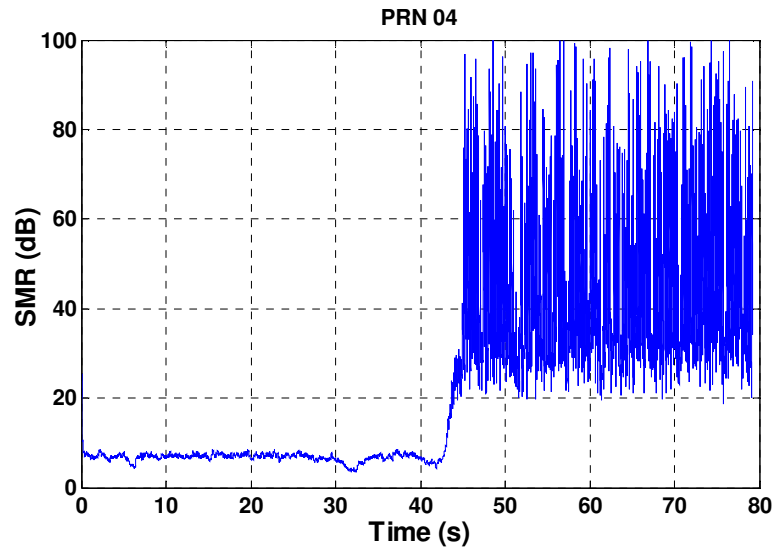


Figure 4.4: SMR for the first scenario

Table 4.1: SMR estimate statistics for the first scenario

SMR (dB)	First duration	Second duration
Mean of the estimated values	7.3	44.3
Standard deviation of the estimated values	1.0	10.7

The estimated multipath relative code delay ($\hat{\tau}_1$) is also shown for this scenario in Figure 4.5. The mean and standard deviation of the estimated relative code delays for the first and second duration are showed in Table 4.2. The mean value is 0.53 chips for the first 43 s and 0.01chips after the multipath power is switched off. The RMSE for the first 43 s is also 0.07 chips, which demonstrates that the KMP algorithm has correctly detected the embedded multipath power, and has reasonably accurately estimated the corresponding multipath parameters.

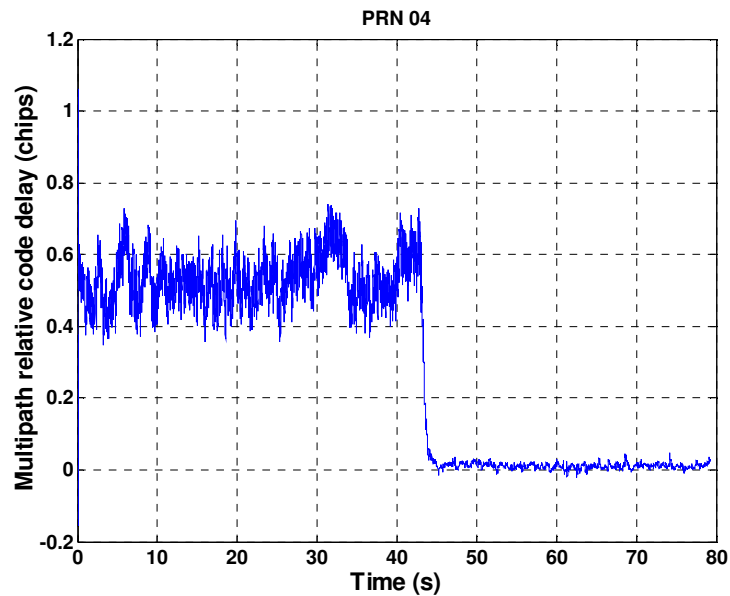


Figure 4.5: Multipath relative code delay (chips) for the first scenario

Table 4.2: Relative code delay estimates statistics for the first scenario

Relative code delay (chips)	First duration	Second duration
Mean of the estimated values	0.53	0.01
Standard deviation of the estimated values	0.07	0.01

As discussed in Chapter 3, the diagonal elements of the \mathbf{P} matrix are the estimated states' error variances. These values show the expected precision of the estimates. The estimated error standard deviations corresponding to the first and sixth Kalman states which are the LOS (A_0) and multipath amplitudes (A_1) are plotted in Figure 4.6, and $\sqrt{P[8][8]}$ which corresponds to the estimated error standard deviation for the multipath relative code delay (τ_1) is shown in Figure 4.7. At the start of the Kalman filter estimation process, when there is large uncertainty on the Kalman states estimates, these values are initialized to large numbers as listed in Table 4.3. These elements subsequently converged to small values after the filter corrected the states by the measurements and the uncertainty in the states estimates decreased. Considering the LOS amplitude component $P[1][1]$, it can be seen to have dropped to a smaller number once the multipath power is switched off in the simulator. This shows that the filter has estimated the LOS amplitude with higher precision when there is no multipath power corrupting the signal. The same trend can be seen for the multipath amplitude component $P[6][6]$. Since there is LOS as well as multipath power in the first 43 s, the filter estimation precision is lower than the duration when there is just LOS power embedded in the composite signal.

Table 4.3: Initial values for the error standard deviations

LOS amplitude (arbitrary units)	Multipath amplitude (arbitrary units)	Multipath relative code delay (chips)
6300	9500	3.2

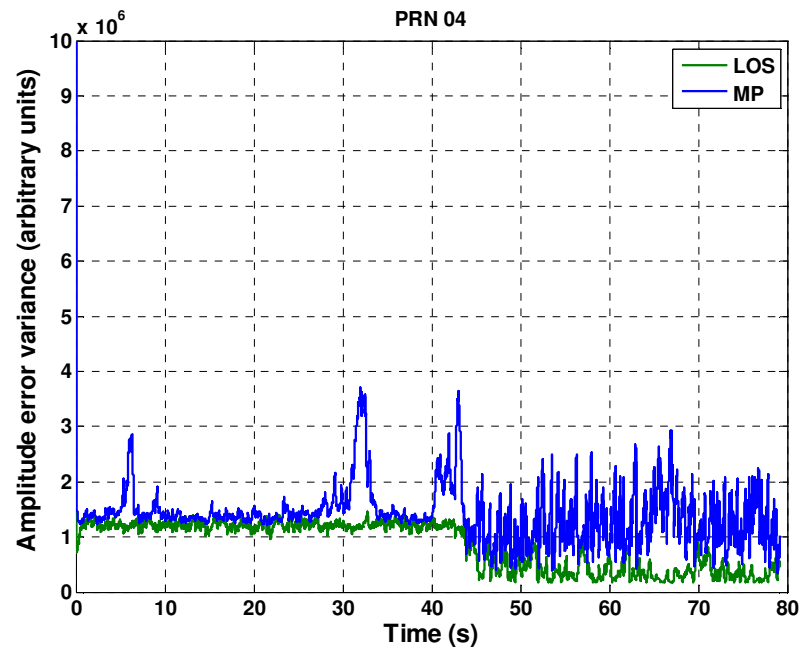


Figure 4.6: Estimated LOS and multipath amplitude error standard deviations

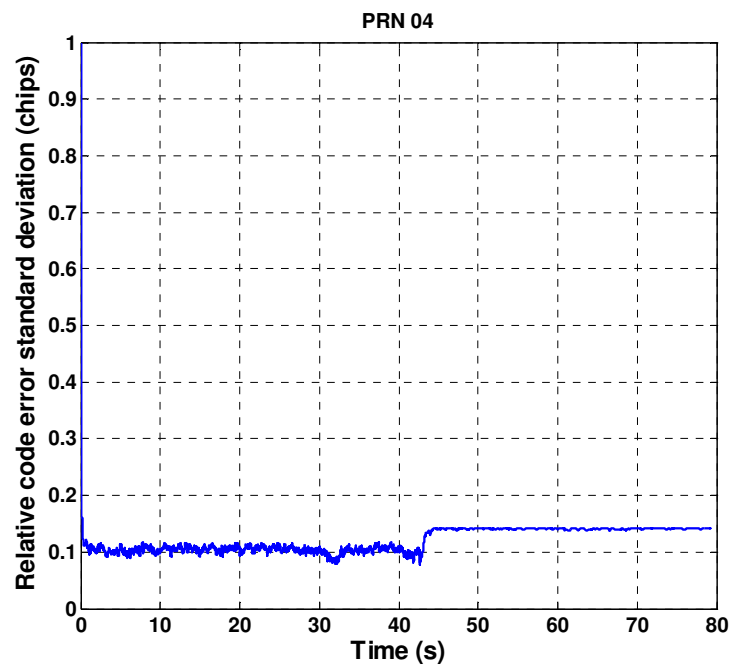


Figure 4.7: Estimated multipath relative code delay error standard deviations

For the multipath relative code delay component ($\sqrt{P[8][8]}$), it has increased to a larger value once the multipath power is switched off. During the first 43s, the estimated error standard deviation converges to 0.1 chips. As Table 4.2 shows, the true error standard deviation is 0.07 chips, which is close to the error standard deviation estimated by the filter. During the first 43 s, since the multipath power is present in the measurements, the filter has had a better precision for estimating the multipath parameters such as the multipath relative code delay. As shown by the figures and tables in this sub-section, the KMP has estimated the multipath parameters in this scenario with the aforementioned estimation characteristics.

4.1.2 Second scenario

The second scenario corresponds to a multipath environment in which a multipath signal spaced 0.2 chips from the LOS signal with an SMR of 6 dB is present in the received signal. This scenario tests the KMP algorithm for a multipath condition when the multipath component is considerably closer to the LOS component than in the first scenario.

The entire 60 s duration of the test can be divided into three parts. The first part consists of the first 22 s when the multipath with the mentioned characteristics is added to the LOS signal. In the next 18 s, the multipath power is switched off in the simulator. The multipath power is turned on again for the last 20 s and the multipath signal with the same characteristics is added again to the LOS signal. The third period tests the KMP ability to track the multipath signal after its absence in the second period. The LOS signal

power is also kept constant over the entire 60 s duration. Figure 4.8 shows the LOS (A_0) and multipath (A_1) amplitudes estimated by the KMP algorithm. The estimated LOS amplitude is constant over the entire interval. The estimated multipath amplitude is half the estimated LOS amplitude in the first and third periods when the multipath power was present in the signal, which is equivalent to an SMR of 6 dB. The KMP shows the mean multipath amplitude as zero in the second period when there was no multipath signal. This verifies that the KMP has accurately estimated multipath power from the composite signal for the three periods. It has also correctly detected the absence of multipath signal in the second period.

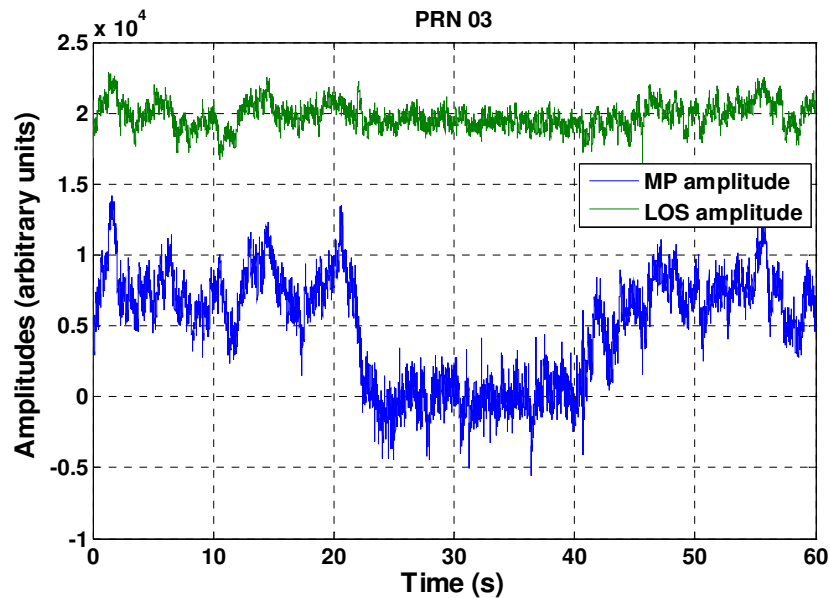


Figure 4.8: LOS and Multipath amplitude for the second scenario

The SMR for this scenario is also plotted in Figure 4.9. The mean and standard deviation of the estimated SMR values for the three different durations in the test are shown in Table 4.4. The mean estimated SMR is 6.9 dB for the first 22 s and 7.4 dB for the last 20 s period, but it is very high (20.7 dB) in the second 18 s period when the multipath

power is switched off in the hardware simulator. Since there was no multipath signal present during the second period, the KMP has estimated the mean multipath power close to zero. This has made the denominator in Eq. 4.1 to have small values which is equivalent to large values of SMR. The same trend was also observed in the first scenario. Comparing the RMSE for the first (1.4 dB) and third (1.9 dB) periods shows that the error in the SMR estimation has increased in the third period. In the second period, the estimated multipath amplitudes (Figure 4.8) were close to zero. After the multipath power is added to the signal in the third part, this state has slowly converged to its true value, which has resulted in higher RMSE values in this period comparing to the first period.

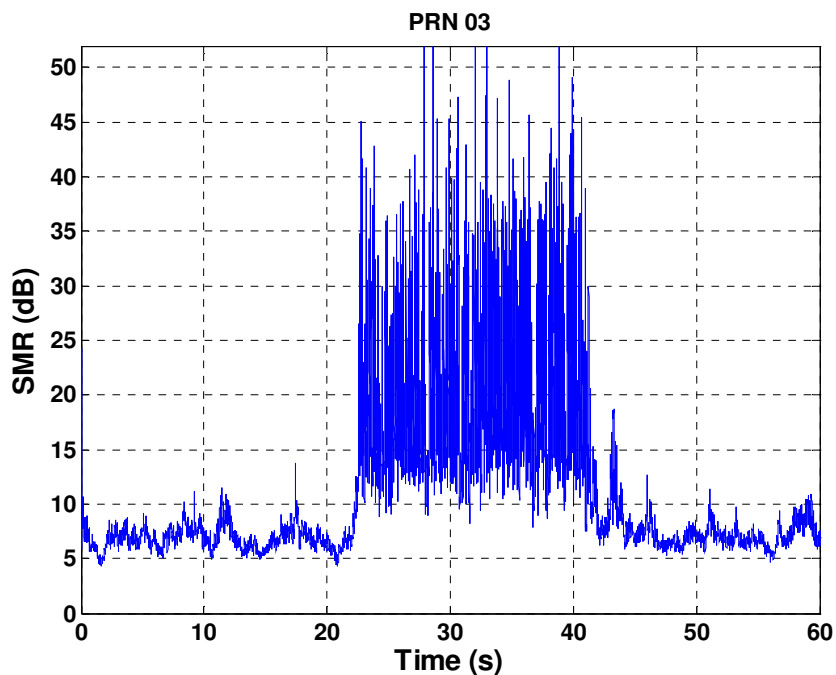


Figure 4.9: SMR for the second scenario

Table 4.4: SMR statistics for the second scenario

SMR (dB)	First duration	Second duration	Third duration
Mean of the estimated values	6.9	20.7	7.4
Standard deviation of the estimated values	1.1	5.0	1.4

The estimated multipath relative code delay (τ_1) is also shown in Figure 4.10. Its mean value is 0.26 chips for the first 22 s and 0.02 after the multipath power is switched off in the second period. The mean estimated value rises to 0.25 chips in the third period after the multipath power is turned on again. The RMSE for the first and third duration is also 0.08 chips, which demonstrates that the KMP algorithm has estimated the multipath parameters embedded in the signal within an acceptable accuracy.

These scenarios were used to investigate KMP performance under different multipath relative code delays (0.2 and 0.5 chips). The RMSE is higher in the second scenario where the multipath signal is spaced closer to the LOS component. As expected, the closer multipath signal has more correlated characteristics with the LOS signal and it is harder to entirely estimate the multipath signal components in this case. The third scenario shows the KMP performance under different SMR conditions.

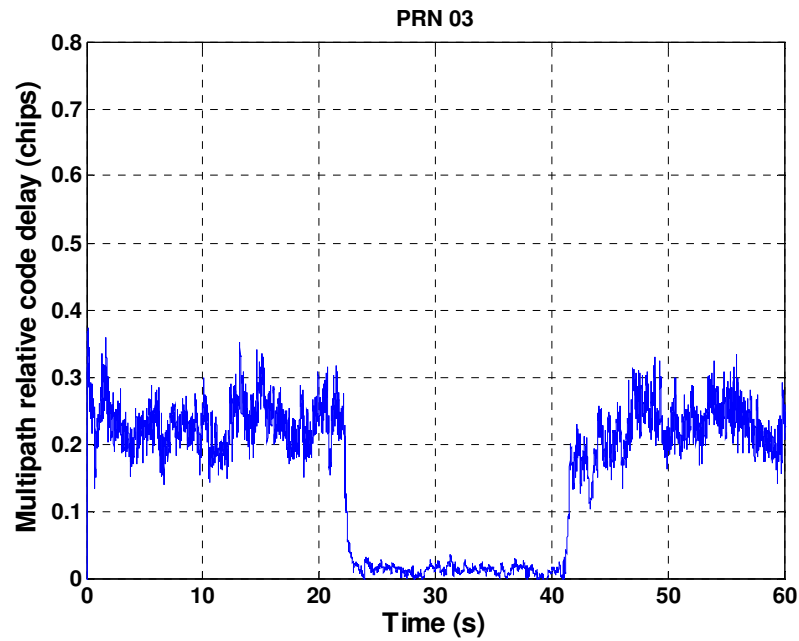


Figure 4.10: Multipath relative code delay (chips) for the second scenario

Table 4.5: Relative code delay statistics for the second scenario

Relative code delay (chips)	First duration	Second duration	Third duration
Mean of the estimated values	0.26	0.02	0.25
Standard deviation of the estimated values	0.07	0.01	0.08

The estimated error standard deviations corresponding to the LOS (A_0) and multipath amplitudes (A_1) are shown in Figure 4.11, while $\sqrt{P[8][8]}$, which is the estimated error standard deviation value for the multipath relative code delay (τ_1), is shown in

Figure 4.12. Similar to the first scenario, the amplitude standard deviations ($\sqrt{P[1][1]}$ and $\sqrt{P[6][6]}$) are higher in the presence of multipath power compared to the interval in which it is switched off. This demonstrates a greater degree of uncertainty in amplitude estimation when both LOS and multipath components are present.

The multipath relative code delay error standard deviation ($\sqrt{P[8][8]}$) is also lower when the multipath is embedded in the signal, as was also observed for the first scenario. During the first and third periods, when the multipath power is present in the signal, the estimated error standard deviation converges to 0.11 chips. As Table 4.4 shows, the true error standard deviations are 0.07 and 0.08 chips which are close to the error standard deviations estimated by the filter.

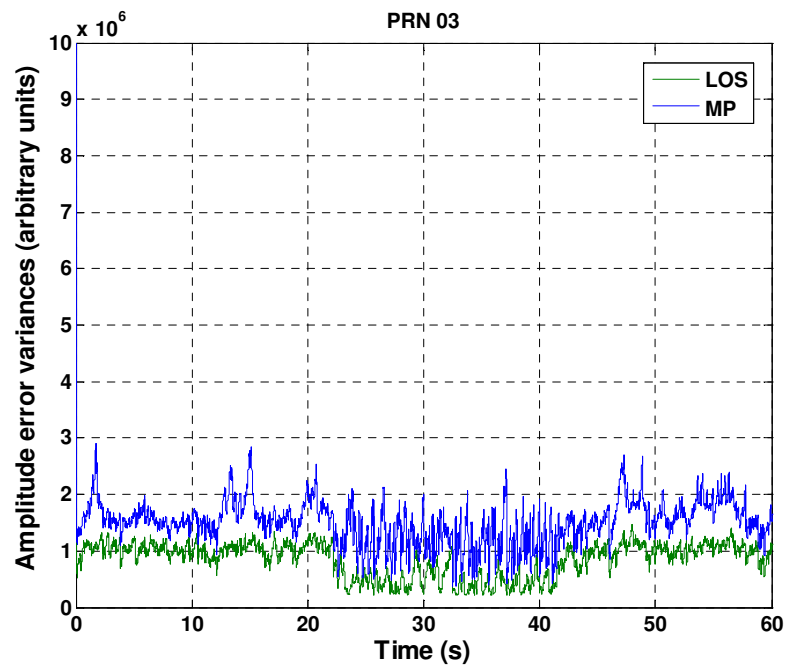


Figure 4.11: Estimated LOS and multipath estimate error standard deviations

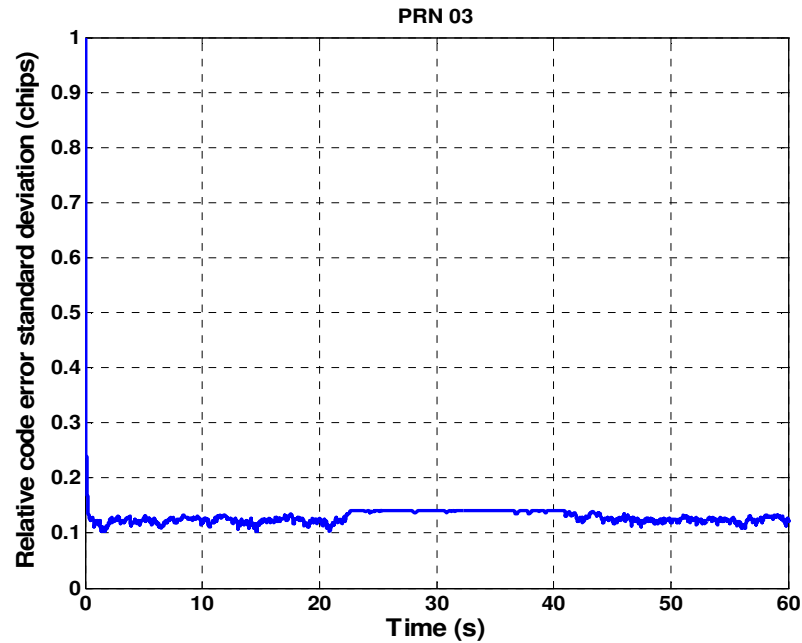


Figure 4.12: Estimated multipath relative code delay estimate standard deviations

4.1.3 Third scenario

The KMP algorithm is tested under different SMRs in the third simulated scenario in order to investigate its sensitivity to the SMR level. In this scenario, the LOS signal power is kept constant over the whole 60 s duration while the multipath power is changed every 25 s. The SMR is 12 dB for the first 25 s, then it is raised to 20 dB for the second 25 s period, and finally it is dropped to 6 dB for the last 10 s period. The multipath relative code delay is 0.2 chips for the entire duration. The estimated LOS and multipath amplitudes are plotted in Figure 4.13, while Figure 4.14 shows the SMR values estimated through the KMP algorithm.

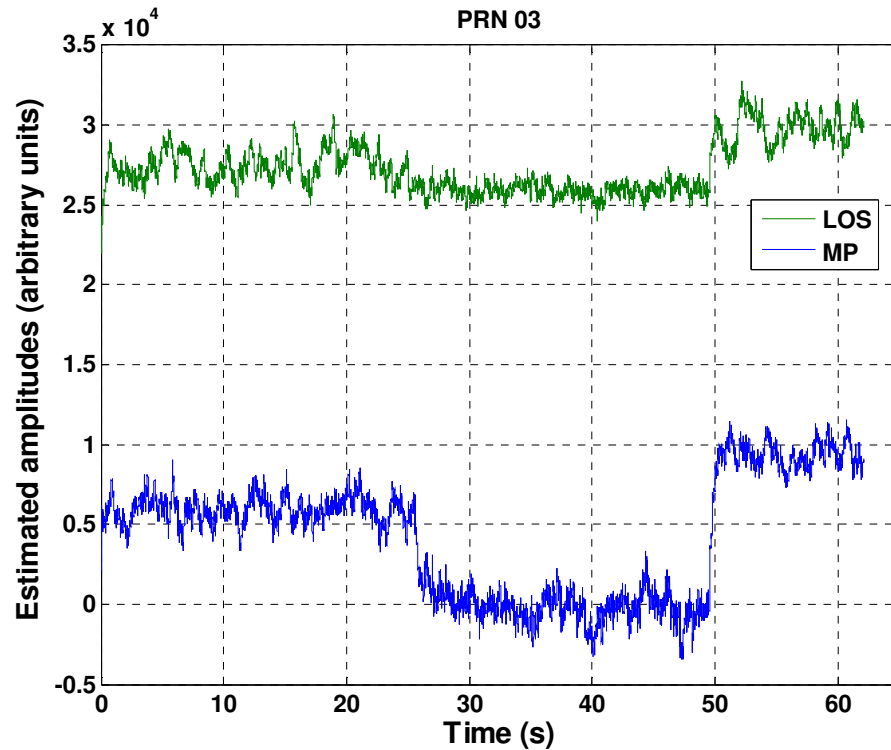


Figure 4.13: LOS and Multipath amplitude for the third scenario

The estimated LOS amplitude is constant when the SMR is 12 and 20 dB, but is higher than its actual value when the multipath power is increased. It seems when the multipath component is spaced close to the LOS signal, the KMP algorithm did not detect all the multipath power embedded in the composite signal, so some part of the multipath power has leaked into the LOS amplitude estimate. While the KMP estimator has estimated the multipath amplitude with a reasonable accuracy when the actual SMR is 12 and 6 dB, it has detected the mean multipath amplitude as zero when the actual SMR is 20 dB. This indicates that there is a limit to the sensitivity of the technique.

The estimation characteristics for the three different durations in the test are showed in Table 4.6. The mean SMR values for the first and third periods are 13.5 dB and 8 dB

while the actual SMR values are 12 dB and 6 dB, respectively. Since the multipath power is very small compared to the LOS power in the case when the actual SMR is 20 dB, the filter is not able to extract the noisy multipath components from the composite signal. This caused the estimated SMR to have high values with a mean of 42.7 dB. Consequently, the RMSE is also very high (24.9 dB) in this period. This shows that multipath powers with SMR values as low as 20 dB are not resolvable by the KMP technique.

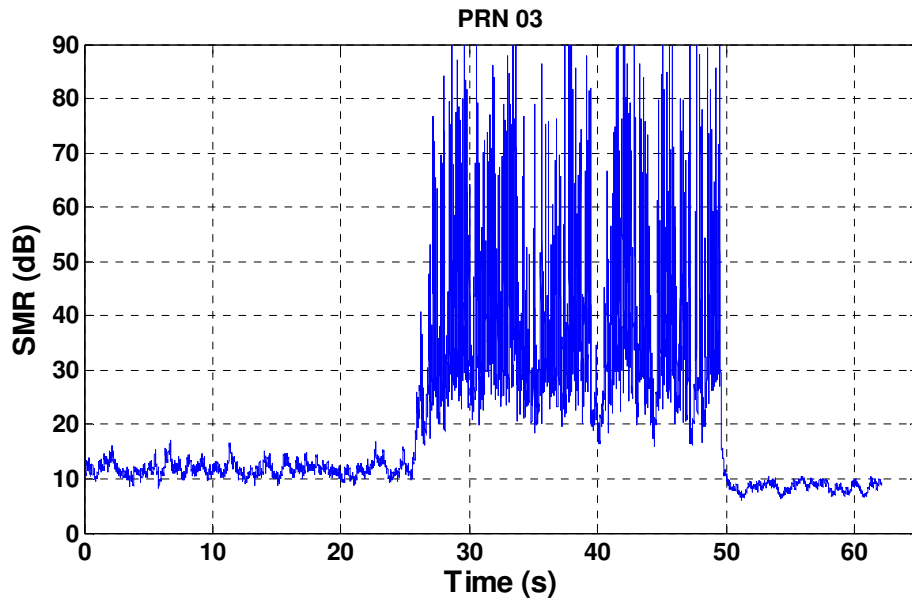


Figure 4.14: SMR for the third scenario

Table 4.6 : SMR statistics for the third scenario

SMR (dB)	First period	Second period	Third period
Mean of estimated values	13.5	42.7	8.2
Standard deviation of estimated values	1.3	10.3	0.87
RMSE	2.0	24.9	3.1

The estimated multipath relative code delay (τ_1) is also shown in Figure 4.15. As Figure 4.14 and 4.15 clarify, the KMP algorithm has detected multipath powers with SMR values of 6 and 12 dB embedded in the composite signal. The mean multipath value is 0.25 chips for the first 25 s and 0.30 chips for the last 10 s. As demonstrated by the SMR results, multipath power with SMR of 20 dB is absorbed partially in the LOS components. Consequently, the KMP has estimated the relative code delay with a chip error of 0.1 to 0.2 when the SMR is 20 dB. During this period of very weak multipath interference, the estimated relative code delay has a mean value of 0.01 chips with an RMSE of 0.19 chips, which shows that the multipath power with a SMR of 20 dB is not resolvable from the LOS component and will be absorbed in the LOS component.

The RMSE for the third duration (0.1 chips) is higher than its corresponding value for the first duration (0.06 chips). Since the KMP filter parameters corresponding to the multipath relative code delay were tuned in order to track low SMR levels (between 12 and 20 dB), the KMP has not sensed all the power variations corresponding to the multipath component with a SMR of 6 dB. As a result, some portion of the multipath power has leaked into the LOS states estimation and has caused an additional bias in the multipath Kalman estimates in the third period.

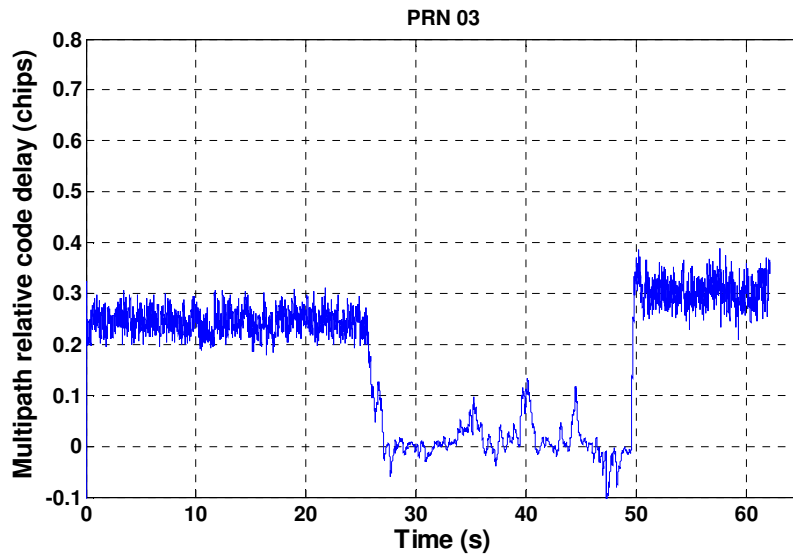


Figure 4.15: Multipath relative code delay (chips) for the third scenario

Table 4.7: Relative code delay statistics for the third scenario

Relative code delay (chips)	First duration	Second duration	Third duration
Mean of the estimated values	0.25	0.01	0.30
Standard deviation of the estimated values	0.02	0.03	0.02
RMSE	0.06	0.19	0.10

4.2 Real multipath environment

A test under moderate multipath conditions was performed in order to characterize the environment using KMP and other parameterization techniques. Data were collected on the University of Calgary campus (Figure 4.16 and 4.17). The ICT and Earth Science buildings obscured the LOS GPS signals received from the west and east sides of the

location at elevation angles up to 50° . In addition, a walled walkway obscured signals arriving from the south below about 25° in elevation (MacGougan 2003). The northern direction has a relatively clear view of the sky.

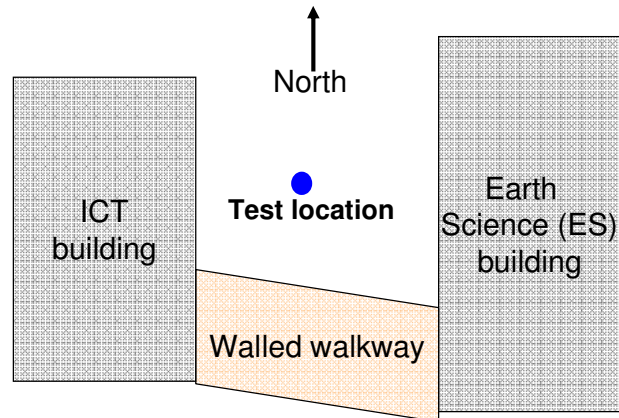


Figure 4.16: Real multipath environment schematic

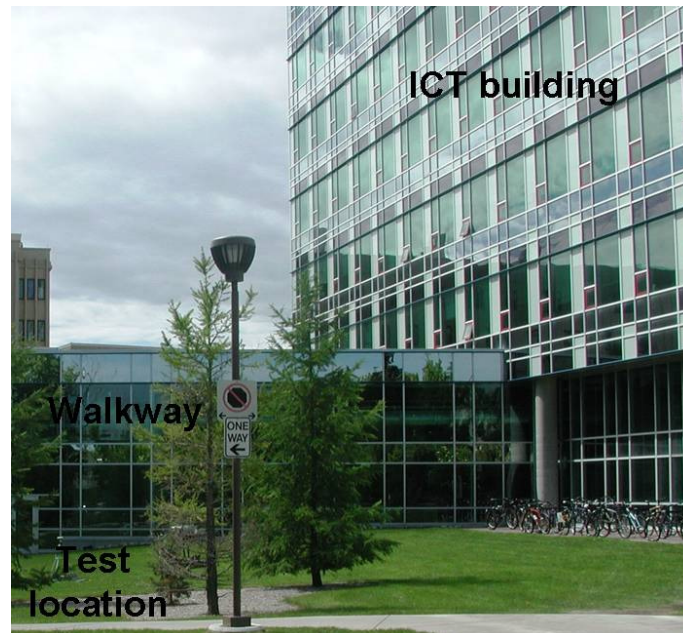


Figure 4.17: Real multipath environment (west and south view)

The ICT building and walled walkway on the west and south side of the test site have glass and metallic surfaces that act as signal blockers and reflectors and are major sources of strong specular multipath. The Earth science building on the east side of the site location (Figure 4.18) has small windows and rough stone textured exterior and is the major source of diffuse signal reflection or obscuration (MacGougan 2003).

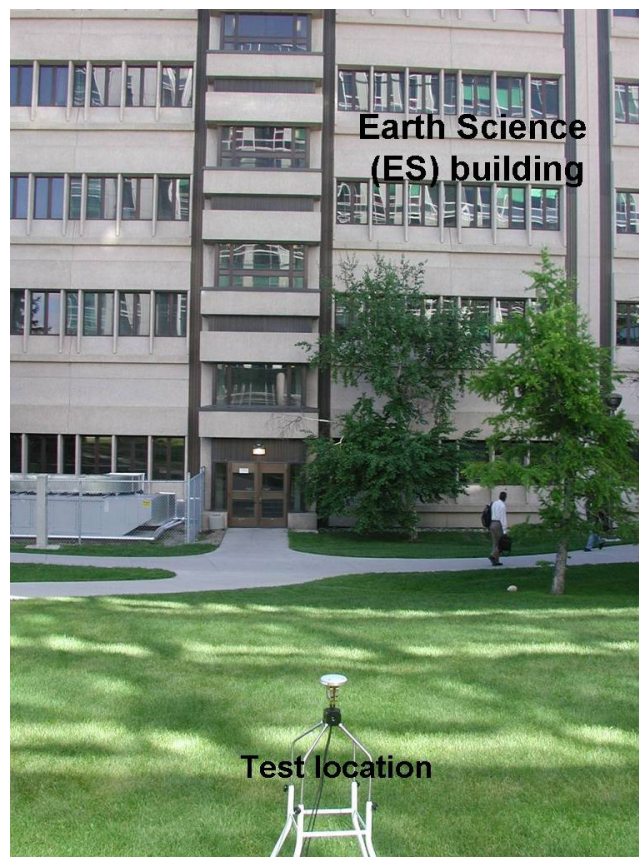


Figure 4.18: Real multipath environment (east view)

4.2.1 Data collection scheme

As shown in Figure 4.19 and 4.20, GPS signals were collected using a dual polarized RHCP/LHCP antenna. This antenna consists of one RHCP and one LHCP antenna integrated in one housing, with a common phase centre. The output of each antenna was fed to a National Instruments PXI-5661 RF front-end after passing through an external

LNA. Two synchronized RF channels in the front-end were assigned to these two antenna outputs for down-converting and digitizing the original RF signal. The resultant two digital IF signals were saved on an external hard drive to be further processed by GSNRx™. The KMP and other algorithms required were implemented in this software by the author. The two power splitters after the antenna outputs were used to split each RHCP and LHCP antenna power between the NI front-end and U-blox commercial high sensitivity receivers.

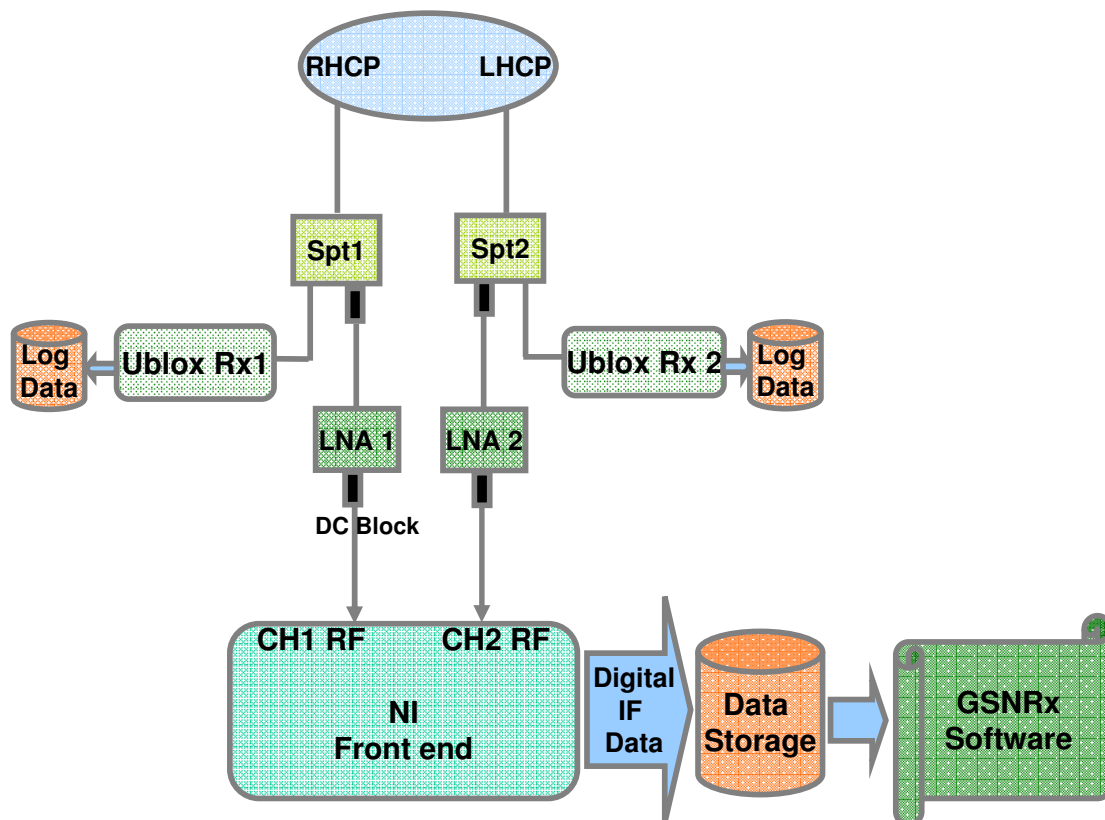


Figure 4.19: Real scenario data collection scheme

U-blox receivers were used in order to power the antennas, and also to monitor the multipath environment for further analyses (Izadpanah et al 2008). They were connected to a laptop computer through the USB ports. The laptop logged U-blox measurements

and also powered these receivers. DC blocks were also used after and before each antenna's LNA in order to isolate DC power from the front-end and to avoid any damage to the front-end's channels. It should be noted that the NI front-end cart was placed 5 m away from the antenna's tripod in order to avoid any unwanted signal blockage and reflection by the test setup equipment (Figure 4.20).

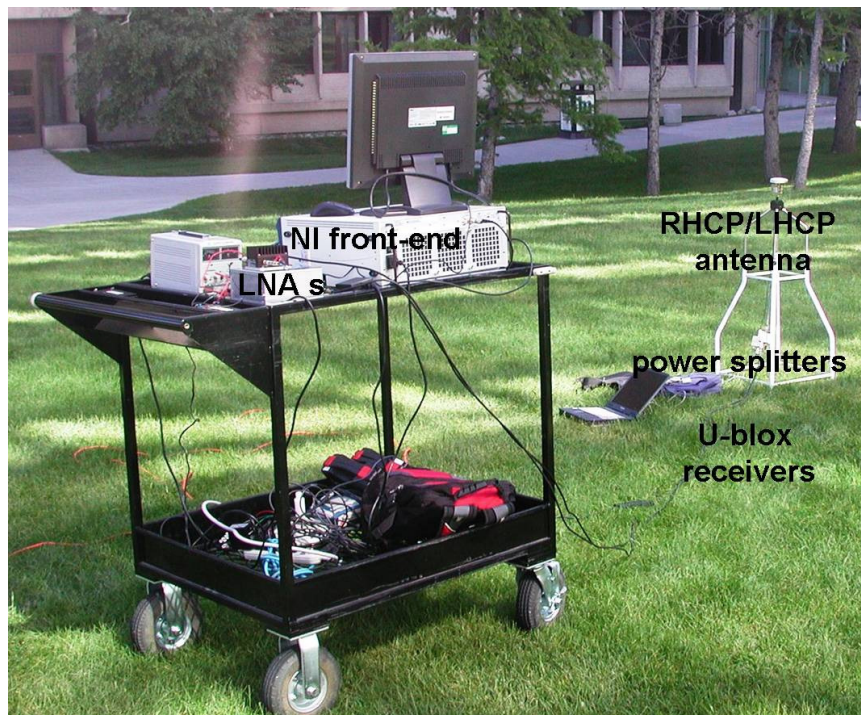


Figure 4.20: Real scenario data collection setup

In order to have the appropriate satellite geometry for the multipath environment, the Trimble planning software was used to find an observation period with a suitable geometry. It was ideal to have multiple satellites in low to medium elevations in the west and east directions in order to receive multipath signals reflected by the ICT and Earth Science buildings. Figure 4.21 shows the GPS constellation observed by the U-blox receiver connected to the RHCP antenna. As expected, the ICT and Earth Science

buildings acted as signal blockers and reflectors and were major contributors to the generation of multipath signals.

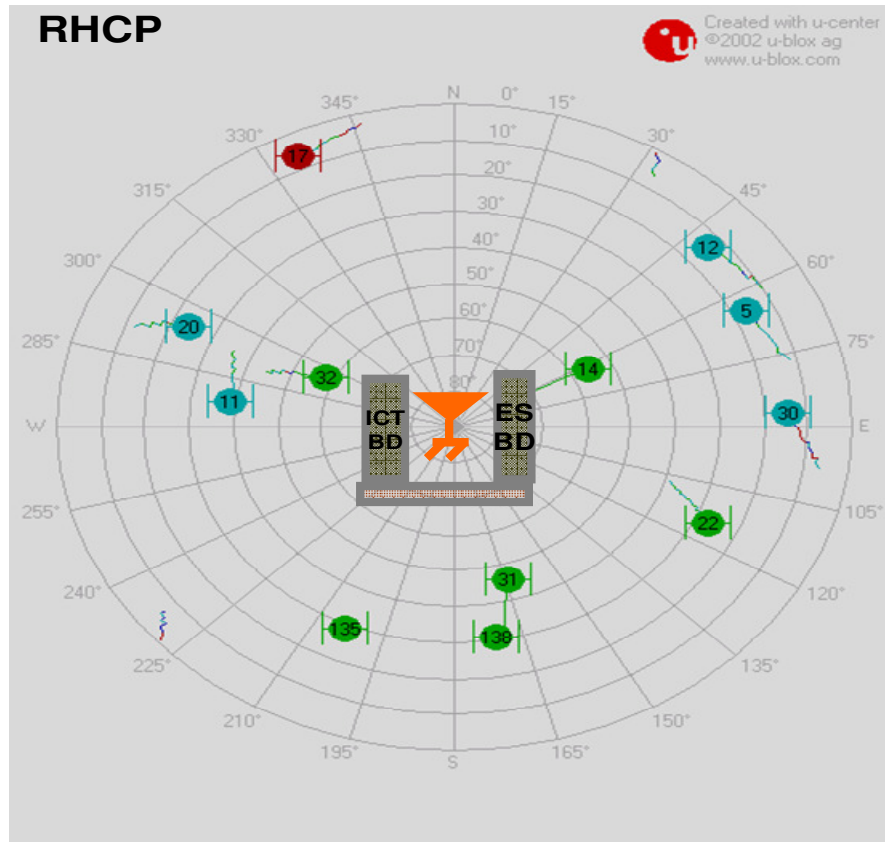


Figure 4.21: GPS constellation observed by U-blox receiver

4.2.2 KMP analysis

As shown in Figure 4.21, Satellite 31 was partially blocked by the walled walkway. Since the walkway's height is not very high, there was still high chance of receiving LOS signals from this satellite. Satellite 14 was partially blocked by the Earth Science building and there was a high probability of multiple reflections from the ICT and Earth Science buildings for this satellite signal. Therefore, it is expected that the signal from Satellite 14 had undergone more multipath distortion than that from Satellite 31. The KMP technique

is applied to the signals from these satellites to estimate their corresponding multipath characteristics.

4.2.2.1 PRN 31 RHCP amplitudes and relative code delays

The KMP algorithm is first applied on the data to characterize PRN 31's signal. The LOS and multipath amplitudes for this PRN are shown in Figure 4.22. Multipath power is changing over time but is considerably lower than the LOS power. Signals are received from the south and there are no major blockages and reflectors in this direction. Therefore, the signals are not subjected to high multipath reflections.

Figure 4.23 shows the multipath relative code delay estimated by the KMP algorithm. It changes over time but has values between 0.05 to 0.08 chips in the periods when the multipath amplitude shows a multipath power added to the signal. These relative code delays correspond to reflectors spaced 10 to 30 m from the receiving antenna. The detected multipath is probably caused by the ICT building, which is 15 m from the antennas.

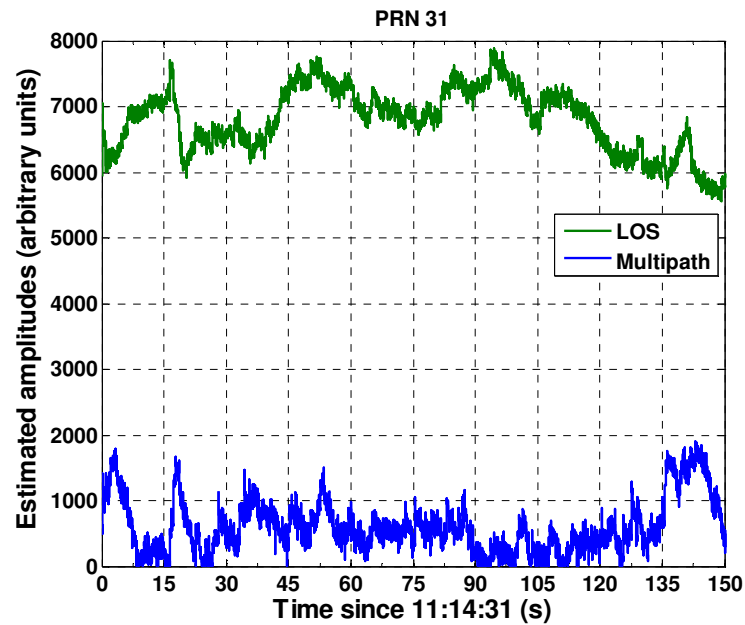


Figure 4.22: PRN 31's LOS and multipath amplitude for real data scenario

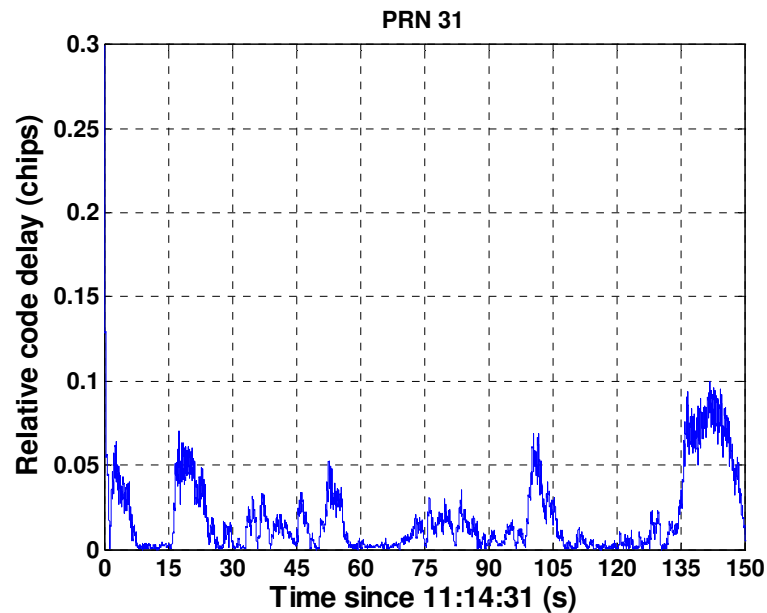


Figure 4.23: PRN 31's multipath relative code delay (chips) for real data scenario

Comparing Figures 4.22 and 4.23 shows a correlation between the estimated multipath amplitude and relative code delay values. The cross-correlation function of these

parameters is generated after their mean values are removed. The function is then normalized to its maximum value (Figure 4.24).

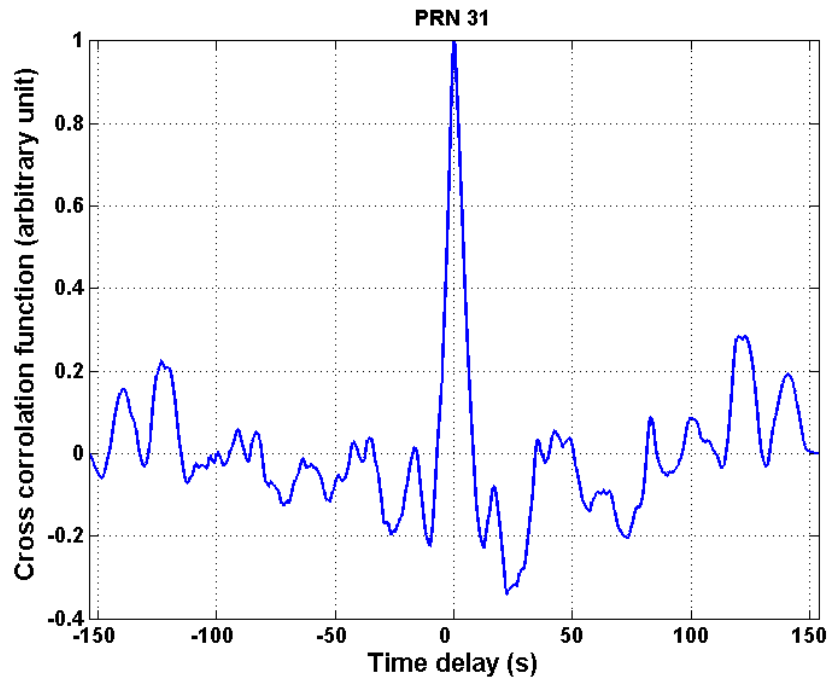


Figure 4.24: PRN 31's multipath amplitude and relative code delay normalized cross correlation function

The correlation coefficient matrix of these two data sets is calculated as

$$\mathbf{C}_{31} = \begin{bmatrix} 1 & 0.78 \\ 0.78 & 1 \end{bmatrix} \quad (4.2)$$

where the diagonal elements correspond to the autocorrelation of each data set and the other two elements show the cross-correlation coefficient of these data sets, at zero relative delay. It shows that instantaneous multipath amplitudes and relative code delays estimated from the KMP algorithm are highly correlated to each other. The correlation

coefficient matrix can be recalculated for the epochs when the multipath amplitudes are sufficiently high so as to be within the KMP's tracking sensitivity. The result is given by

$$\mathbf{C}'_{31} = \begin{bmatrix} 1 & 0.26 \\ 0.26 & 1 \end{bmatrix}. \quad (4.3)$$

As can be seen, the cross-correlation coefficient is higher in Eq. 4.2 as compared to Eq. 4.3 because transient epochs are included in Eq. 4.2. During the transient periods, the amplitude and relative code delay states converge to their true values with nearly the same rate which, in turn, increases the correlation between these parameters. In Eq. 4.3, the effect of transient epochs is isolated from the average correlation coefficient, but still these parameters are correlated to each other. The observed correlation can be caused by the instantaneous multipath environment characteristics and also Kalman filter estimation procedure. When there is no multipath power in the received signal or the multipath power is considerably lower than the LOS power, the KMP detects small values for the multipath amplitudes and correspondingly the relative code delays converge to small values close to zero which shows that the multipath signals' contribution to the total received signal is quite negligible. The multipath relative code delay converges to a non-zero value when the multipath power is sufficiently high to be detected by the KMP technique. This is in accordance with the expected behaviour of an ideal multipath signal detector. As explained before, one extra path is modeled in the KMP algorithm, but there may be more paths with high multipath powers in the real environment. This also can be another source of correlation between these estimated multipath parameters.

4.2.2.2 PRN 14 RHCP amplitudes and relative code delays

The KMP technique was next applied to the PRN 14's signal in order to estimate multipath parameters embedded in this signal. Figure 4.25 shows the LOS and multipath amplitudes for this satellite. Comparing estimated multipath amplitudes for PRN 31 and 14 shows that PRN 14 multipath power is higher than PRN 31's multipath power for the first 50 s. In the next section, SMR values for these signals are analyzed and show the same phenomenon. Signals from this satellite are received from the east and there are blockages and reflectors (ICT building walls) in this direction. Therefore, the signals are subjected to a significant amount of multipath. Multipath relative code delays are also estimated for this satellite in Figure 4.26, which shows multipath powers with relative code delays of 0.05 to 0.1 chips which can be caused by the ICT building walls.

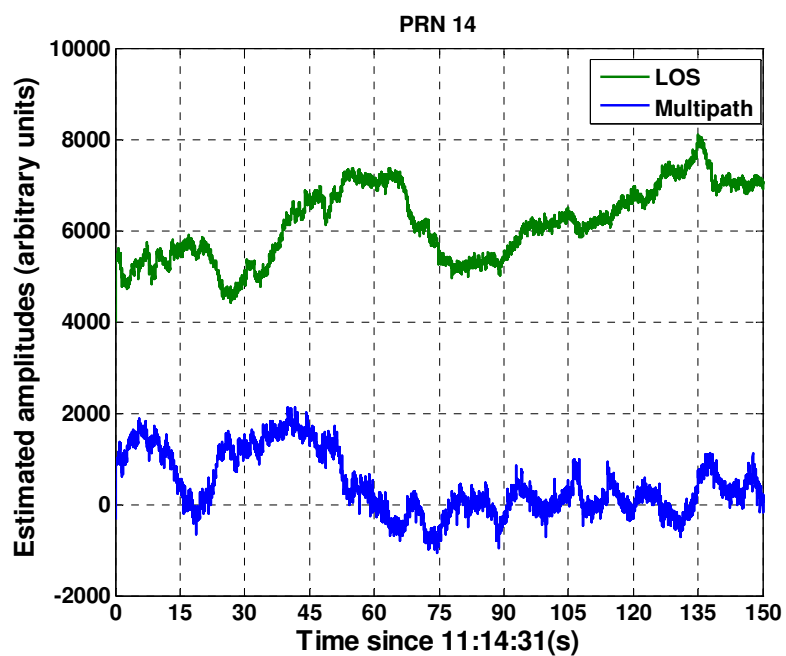


Figure 4.25: PRN 14's LOS and multipath amplitude for real data scenario

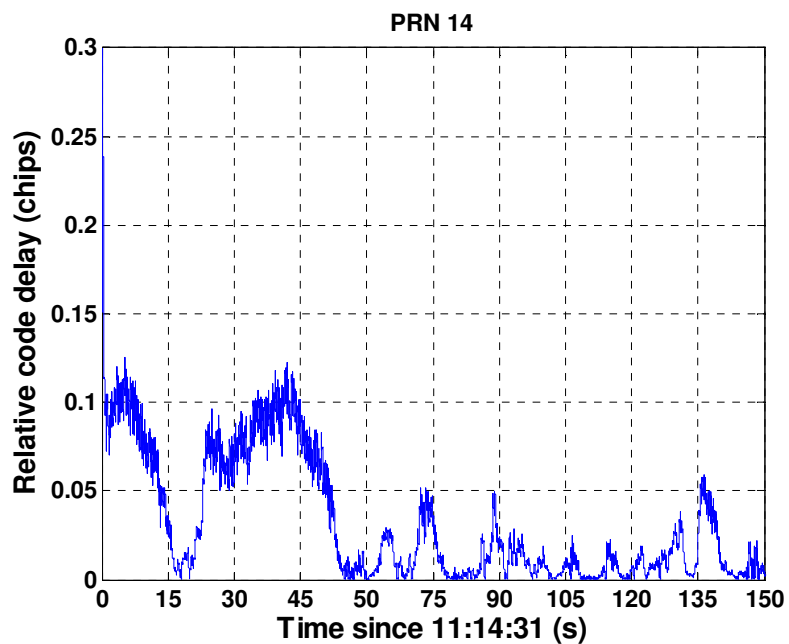


Figure 4.26: PRN 14's multipath relative code delay (chips) for real data scenario

The normalized cross-correlation function of multipath amplitude and relative code delay for PRN 14 is shown in Figure 4.27.

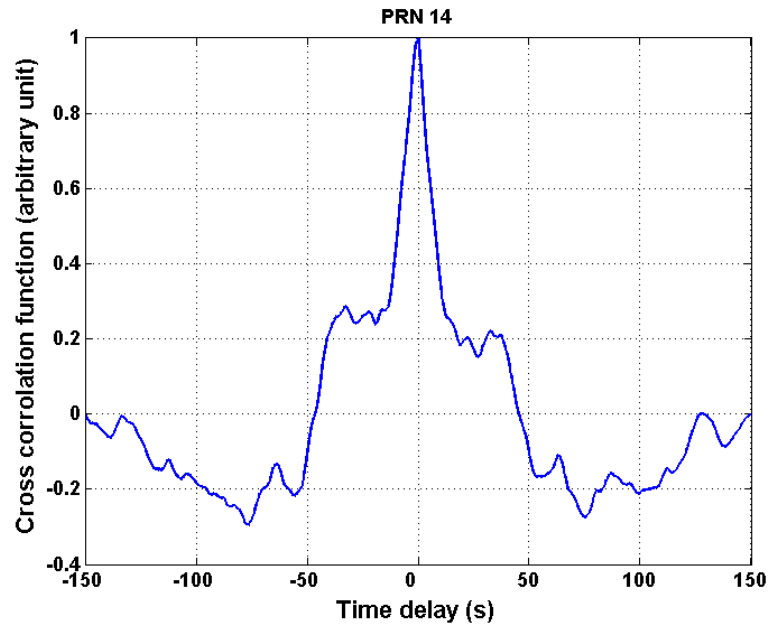


Figure 4.27: PRN 14's multipath amplitude and relative code delay normalized cross correlation function

The correlation coefficient matrix of these two data sets is also calculated as

$$\mathbf{C}_{14} = \begin{bmatrix} 1 & 0.88 \\ 0.88 & 1 \end{bmatrix} \quad (4.4)$$

If the effect of the transient filter response is isolated from the correlation procedure, the correlation coefficient matrix is instead given by

$$\mathbf{C}'_{14} = \begin{bmatrix} 1 & 0.32 \\ 0.32 & 1 \end{bmatrix}. \quad (4.5)$$

As observed previously for PRN 31, the cross-correlation coefficient value decreases after the transient epochs are isolated from the correlation's calculation.

4.2.2.3 PRN 14/31 RHCP SMR analysis

The RHCP and LHCP received signals have different multipath components which make the composite signals sensed by the RHCP and LHCP antennas exhibit different levels of multipath power. This can be shown by estimating the SMR values for RHCP and LHCP signals through the KMP algorithm. As Figure 4.28 shows, PRN 14 exhibits higher multipath fading compared to PRN 31. Similarly, the SMR values for PRN 14 are lower than those for PRN 31, as shown in Figure 4.29. This is in keeping with the assumption that PRN 14 experiences a greater degree of multipath than PRN 31. Multipath power added to the received signal also causes a bias (error) in the pseudorange measurements. Therefore, there is a correlation between low SMR values (Figure 4.29) and high multipath pseudorange errors (Figure 4.30).

The pseudorange multipath error ($MP_{\text{Pseudorange}}$) can be calculated as (Lachapelle 2007)

$$MP_{\text{Pseudorange}} = (\rho - \phi) - (\lambda N + 2d_{ion}) \quad (4.6)$$

where ρ is the pseudorange measurement and ϕ is the phase measurement. These two parameters are obtained from $GSNR_x^{\text{TM}}$. $\lambda N + 2d_{ion}$ is a term corresponding to the integer ambiguity and ionosphere error which is approximated by a quadratic polynomial (Lachapelle 2007).

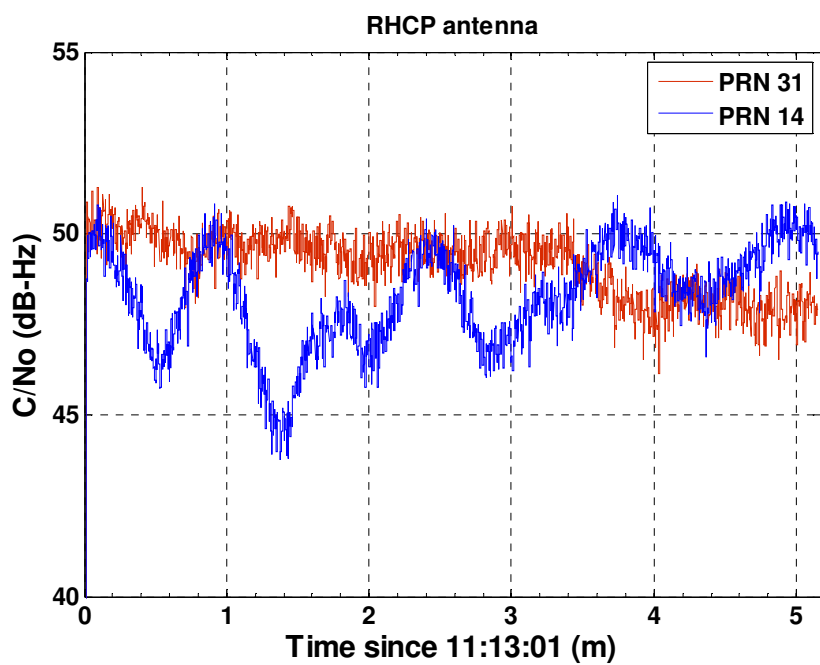


Figure 4.28: RHCP C/N₀ values for PRN 14 and 31

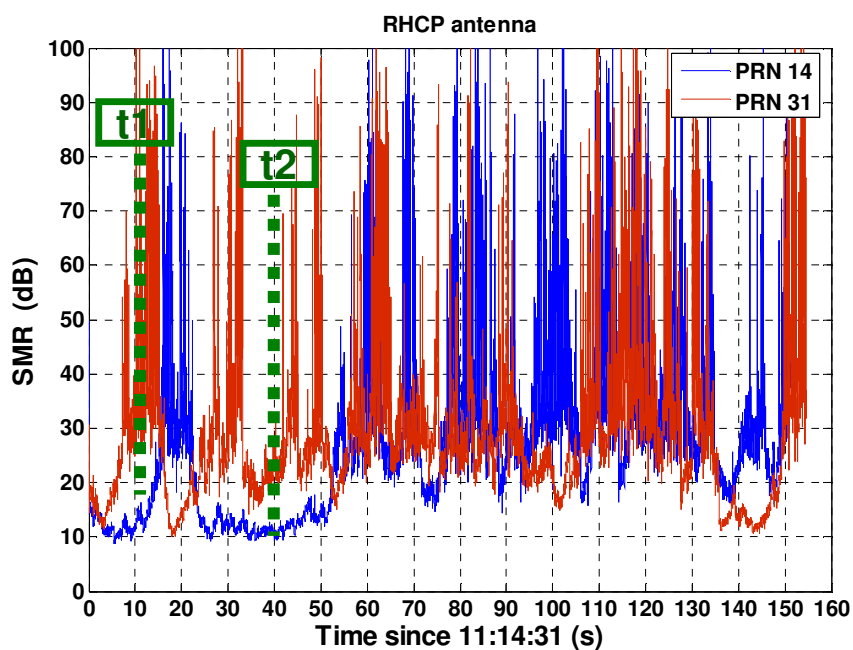


Figure 4.29: PRN 14 and 31 estimated SMR values for the RHCP antenna

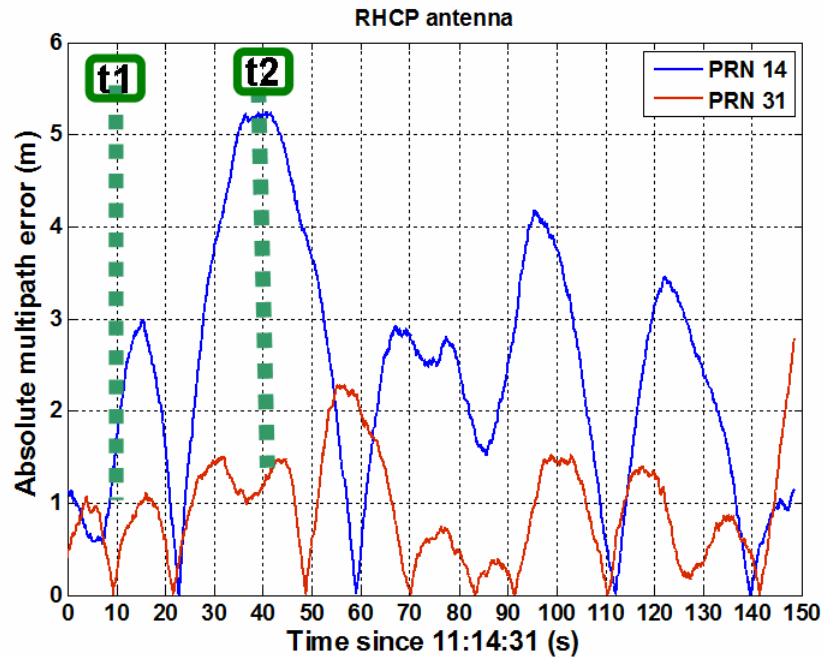


Figure 4.30: PRN 14 and 31 multipath pseudorange errors for the RHCP antenna

As can be seen in these figures, a peak in the SMR (low multipath power) corresponds to a null in the multipath error. This is the case at time t1 for PRN 31 when its SMR has a peak but its multipath error has a null. Also low SMR values correspond to high multipath errors. As an example, time t2 for PRN 14 has a low SMR level but a high multipath error which shows that PRN 14 has received considerable multipath power at this time which has introduced large errors in the pseudorange measurements.

4.3 Summary

This chapter investigated the KMP performance as a multipath parameterization technique in simulated and real multipath environments. Other multipath parameterization techniques which are based on a dual polarized RHCP/LHCP antenna are discussed in the next chapter.

Chapter Five: Dual Polarization techniques analyses

This chapter focuses on the parameterization of multipath environments using dual polarized antennas and methods such as autocorrelation functions, K factor analysis and code minus phase measurements. It begins in Section 5.1 by showing the results from the primary-secondary structure presented in Chapter 3. This gives one a method to analyze multipath characteristics for signals with different levels of multipath power absorption, and for signals received by RHCP and LHCP antennas. The concept of signal power distribution in a multipath environment and the K factor is described in Section 5.2. This section continues by showing the computed K factors for signals received by RHCP and LHCP antennas, under different multipath power levels. Analysis of code minus phase measurements is included in Section 5.3. The K factor results along with code minus phase analyses are gathered in this section to study multipath environments for both RHCP and LHCP antennas. Analyses and comparisons of RHCP and LHCP multipath effects in Carrier to Noise (C/N_0) level and position measurements are shown in Section 5.4. All the aforementioned methods have been used to investigate the effects of different multipath conditions and antenna polarization on different characteristics of the received signal. The real data test scenario introduced in the previous chapter is used for all the results presented in this chapter.

5.1 Autocorrelation function analysis

The autocorrelation function of the GPS C/A code signal ($R_G(\tau)$) can be written as

$$R_G(\tau) = \frac{1}{1023 T_{CA}} \int_{t=0}^{1023} G_i(t) G_i(t+\tau) d\tau \quad (5.1)$$

where $G_i(t)$ is the C/A Gold code sequence for PRN_{*i*}, T_{CA} is the C/A code chipping period (977.5 ns), and τ is the phase of the time shift in the autocorrelation function (Ward et al 2006). $R_G(\tau)$ is obtained in GSNRx™ by computing the correlation powers at different chip spacings from the position of the prompt correlator (Manandhar et al 2006a). The primary-secondary structure developed in GSNRx™ is then applied to the RHCP and LHCP data in order to generate the autocorrelation functions. A set of 11 correlators were used to generate the autocorrelation plots, with spacing given by the following vector **D**

$$\mathbf{D} = [-0.90 \quad -0.70 \quad -0.50 \quad -0.25 \quad -0.15 \quad 0 \quad 0.15 \quad 0.25 \quad 0.50 \quad 0.70 \quad 0.90] . \quad (5.2)$$

In a non-multipath environment in which the strong LOS signal is the only component embedded in the received signal, the autocorrelation function is ideally represented by the triangle showed in Figure 5.1.

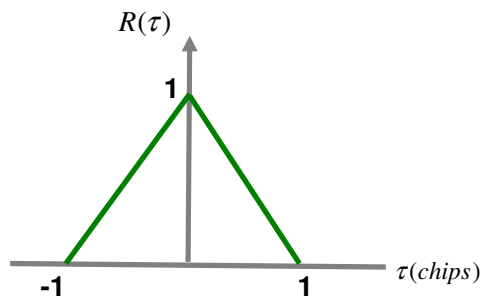


Figure 5.1: Ideal autocorrelation function

In a multipath environment in which multiple paths are added to the LOS signal, the resulting autocorrelation function is corrupted and different from its ideal pattern. Depending on the number and power of the extra paths added to the LOS signal, the autocorrelation function can have a pattern quite different from its ideal case. PRN 14 and 31 are selected as two satellites with different levels of multipath power reception and their corresponding RHCP and LHCP autocorrelation functions are analyzed in the following sections. Instantaneous signal envelope samples ($\sqrt{I^2_P + Q^2_P}$) are used in generating the following autocorrelation functions.

5.1.1 PRN 31 RHCP/LHCP Autocorrelation functions

The RHCP and LHCP autocorrelation functions $\{ R_{RHCP}(\tau), R_{LHCP}(\tau) \}$ for PRN 31 at two different epochs are shown in Figures 5.2 and 5.3. In both cases, $R_{LHCP}(\tau)$ is more corrupted than $R_{RHCP}(\tau)$. As can be seen in Figure 5.4, the LHCP antenna data exhibits greater multipath fading, which explains why $R_{LHCP}(\tau)$ is more distorted than $R_{RHCP}(\tau)$.

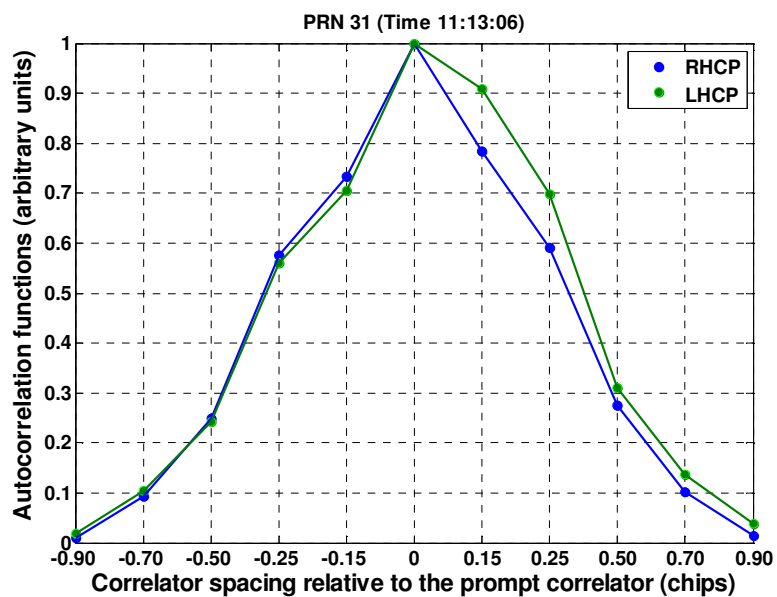


Figure 5.2: PRN 31 Normalized autocorrelation functions for RHCP and LHCP data at time 11:13:06 (t1)

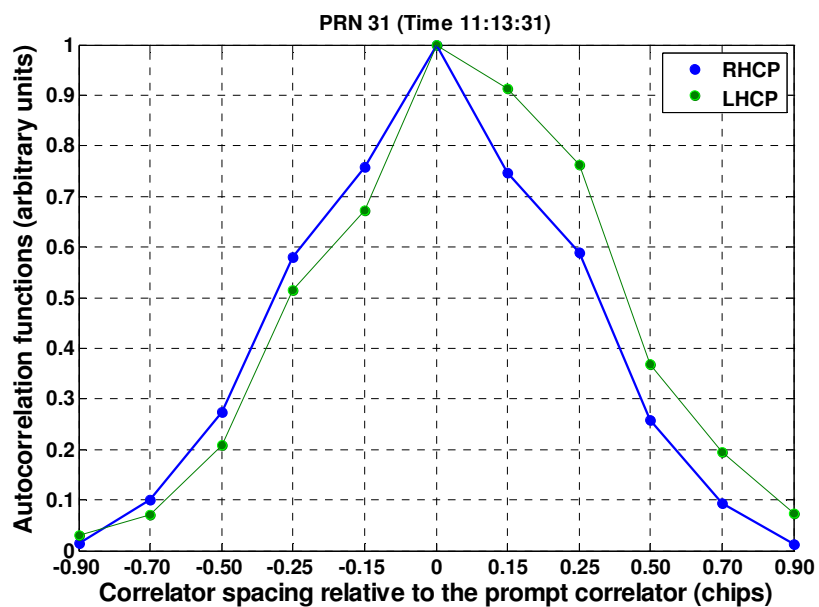


Figure 5.3: PRN 31 Normalized autocorrelation functions for RHCP and LHCP data at time 11:13:31 (t2)

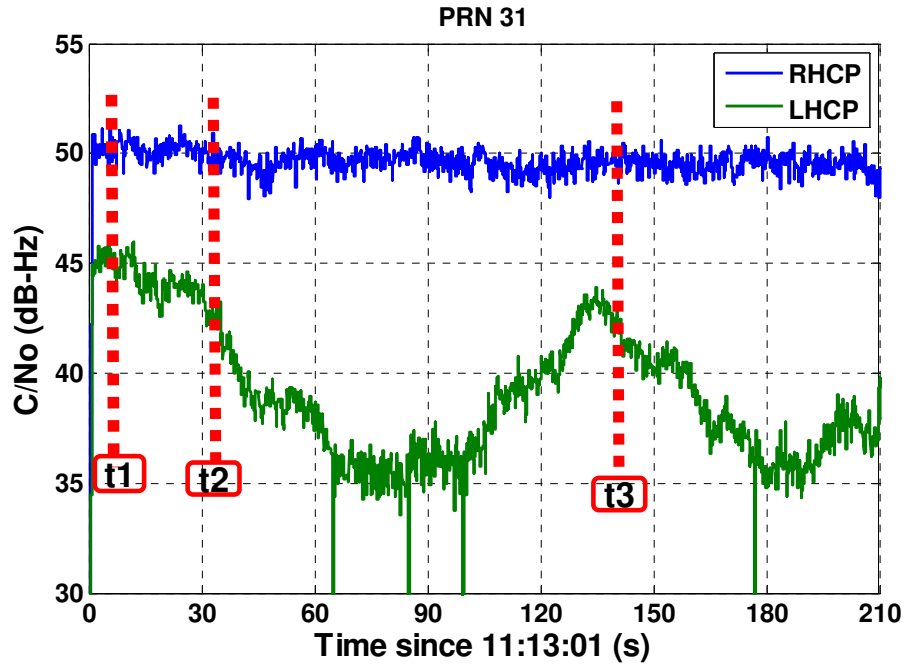


Figure 5.4: C/N_0 values for PRN 31 received by RHCP and LHCP antennas

5.1.2 PRN 14 RHCP/LHCP Autocorrelation functions

The $R_{RHCP}(\tau)$ and $R_{LHCP}(\tau)$ for PRN 14 at times 11:13:06 (t1) and 11:14:23 (t2) are plotted in Figures 5.5 and 5.6, respectively. $R_{LHCP}(\tau)$ at time t2 is more degraded than $R_{LHCP}(\tau)$ at time t1. This phenomenon can be explained by comparing their corresponding C/N_0 values. The multipath components at time 11:14:23 were destructively combined together and have resulted in a deep fade in the C/N_0 level (Figure 5.7). It shows higher multipath power reception at this epoch which has caused more corruption in the autocorrelation function pattern. The LHCP C/N_0 values were subjected to more multipath fading compared to the RHCP C/N_0 values. Therefore, the $R_{LHCP}(\tau)$ patterns are more corrupted than the $R_{RHCP}(\tau)$.

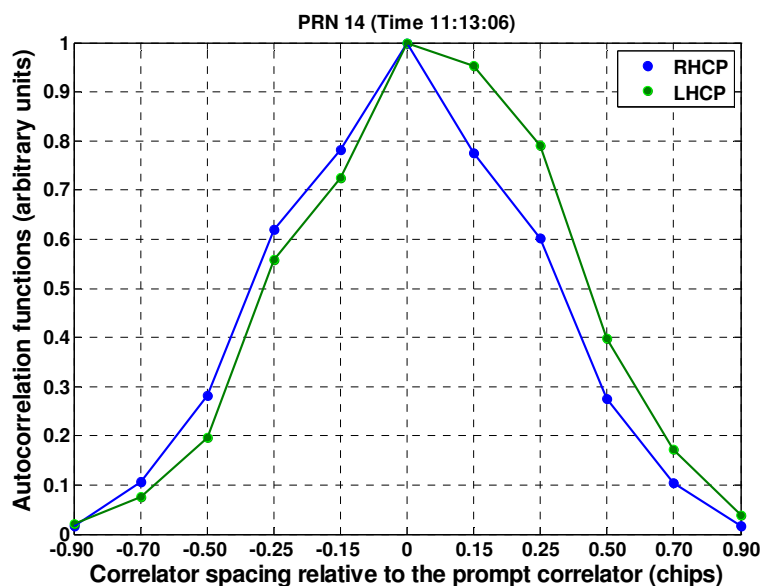


Figure 5.5: PRN 14 Normalized autocorrelation functions for RHCP and LHCP data at time 11:13:06(t1)

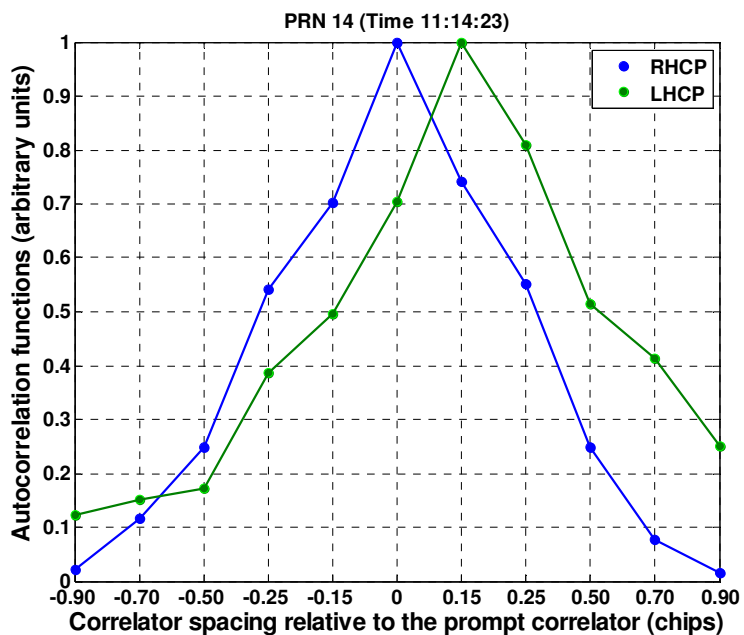


Figure 5.6: PRN 14 Normalized autocorrelation functions for RHCP and LHCP data at time 11:14:23(t2)

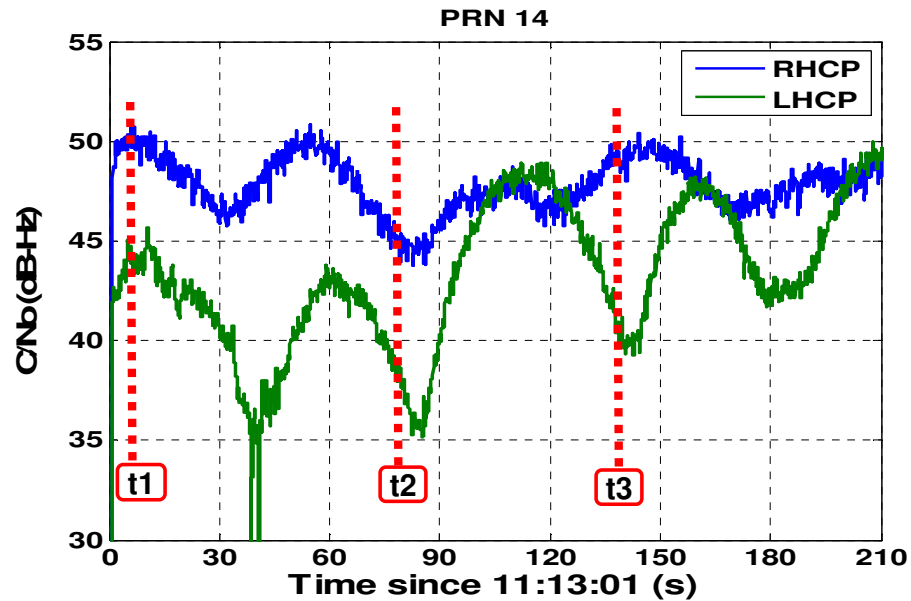


Figure 5.7: C/N_0 values for PRN 14 received by RHCP and LHCP antennas

5.2 Power distribution analysis

Since the RHCP and LHCP antennas have different power patterns, LOS power absorption is quite different for these antennas. Therefore, the total received power in RHCP and LHCP antennas have different characteristics. The RHCP and LHCP antennas' power distributions for satellites with different levels of multipath power reception will be analyzed in the sequel.

5.2.1 K factor concept

In many radio propagation environments where a LOS component exists between the transmitter and receiver, the time-varying envelope of the received signal can be described by a Rician distribution with a Rician K factor (Doukas & Kalivas 2006). The Rician K factor is one measure of communication link quality.

The random process r has a Rice distribution if it can be written as

$$\begin{aligned} r &= \sqrt{x^2 + y^2} \\ x &\sim N(v \cos \theta, \sigma^2) \\ y &\sim N(v \sin \theta, \sigma^2) \end{aligned} \quad (5.3)$$

where x and y are two independent normal processes with the characteristics described in Eq. 5.3 and θ is any real number. The Rician probability density function is

$$f(r|v, \sigma) = \frac{r}{\sigma^2} e^{-\frac{(r^2+v^2)}{2\sigma^2}} I_0\left(\frac{rv}{\sigma^2}\right) \quad (5.4)$$

where $I_0()$ is the modified Bessel function of the first kind of order zero. The Rayleigh distribution can also be viewed as a Rician distribution with v set to zero:

$$\begin{aligned} v=0 &\Rightarrow f(r|\sigma) = \frac{r}{\sigma^2} e^{-\frac{r^2}{2\sigma^2}} \\ r &= \sqrt{x^2 + y^2} \quad x \sim N(0, \sigma^2) \quad y \sim N(0, \sigma^2) \end{aligned} \quad (5.5)$$

For the Rician distribution of Eq. 5.5, the Rician K factor can be defined as

$$K = \frac{\text{LOS power}}{\text{Multipath power}} = \frac{P_{\text{LOS}}}{P_{\text{MP}}} \equiv 10 \log_{10}\left(\frac{v^2}{2\sigma^2}\right). \quad (5.6)$$

The K factor is simply the ratio of LOS power to the multipath power. When K is expressed in decibels, a harsh multipath environment has a large negative K value, and a multipath-free environment has a large positive K value.

Figure 5.8 shows how the Rician distribution pattern changes when the LOS power increases. In this figure, sigma (σ) is kept constant and v increases, which is equivalent

to increasing the K factor. As can be seen, a distribution with a higher K factor (higher ν) has a more symmetric pattern. Figure 5.9 shows the variation in the Rician distribution when the multipath power increases, i.e. ν is constant and σ increases which is equivalent to decreasing the K factor. As can be observed, a distribution with a lower K factor (higher σ) has a more asymmetric distribution.

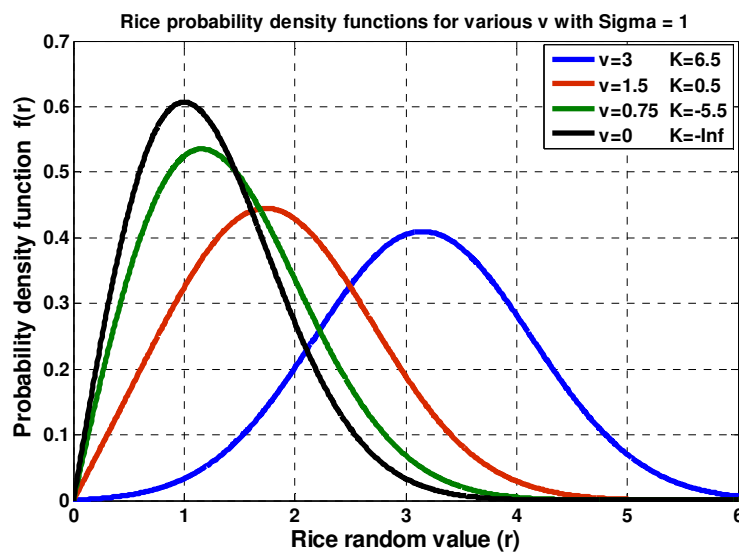


Figure 5.8: Rician distribution (constant sigma)

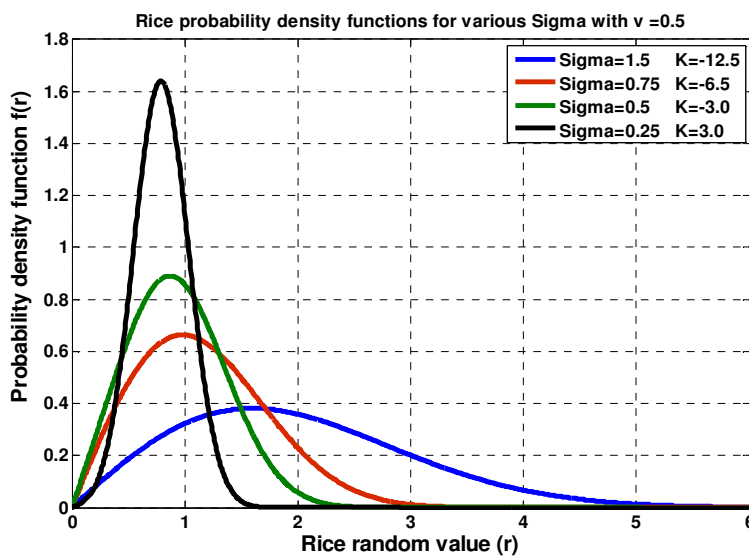


Figure 5.9: Rician distribution (constant ν)

By increasing the K factor, the distribution pattern becomes more symmetric, and by lowering the K factor, the distribution becomes more asymmetric with a longer tail. As can be concluded from Eq. 5.6 and Figures 5.8 and 5.9, a higher K factor corresponds to an environment with lower multipath power (lower σ) absorbed in the composite received signal, and the power distribution is more symmetric.

5.2.2 K factor analysis

The Rician K factor can be approximated by fitting the power distribution to a Rician distribution (Doukas & Kalivas 2006). Estimated K factors can be derived for different satellites and antenna types to show the level of multipath power absorption in the total received signal. Satellites 31 and 14 with different multipath characteristics are selected, and their corresponding K factors are estimated. For each satellite, both RHCP and LHCP data are considered to investigate the antenna polarization effect on the power distribution pattern.

The prompt correlator outputs (I_P, Q_P) in the standard loop architecture were used for generating the signal envelope samples ($\sqrt{I_P^2 + Q_P^2}$). A window at time t_3 (Figures 5.4 and 5.7) with a duration of 20 s was selected. The distribution patterns of the 20,000 samples in the window are then generated for the RHCP and LHCP data. K factors are also estimated from the corresponding distribution functions.

5.2.2.1 PRN 31 RHCP/LHCP power distributions

The Rician K factors for the PRN 31 RHCP and LHCP data are shown in Figures 5.10 and 5.11. Comparing the RHCP ($K_{RHCP}=12.2$ dB) and LHCP K factors ($K_{LHCP}=2.8$ dB) reveals that more multipath power is absorbed in the LHCP antenna relative to the RHCP antenna.

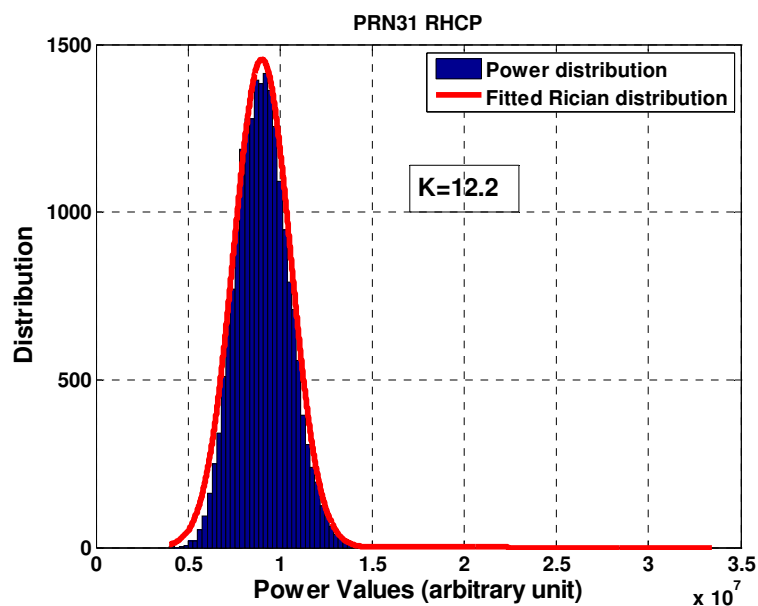


Figure 5.10: PRN 31 power distribution and corresponding Rician distribution for RHCP antenna

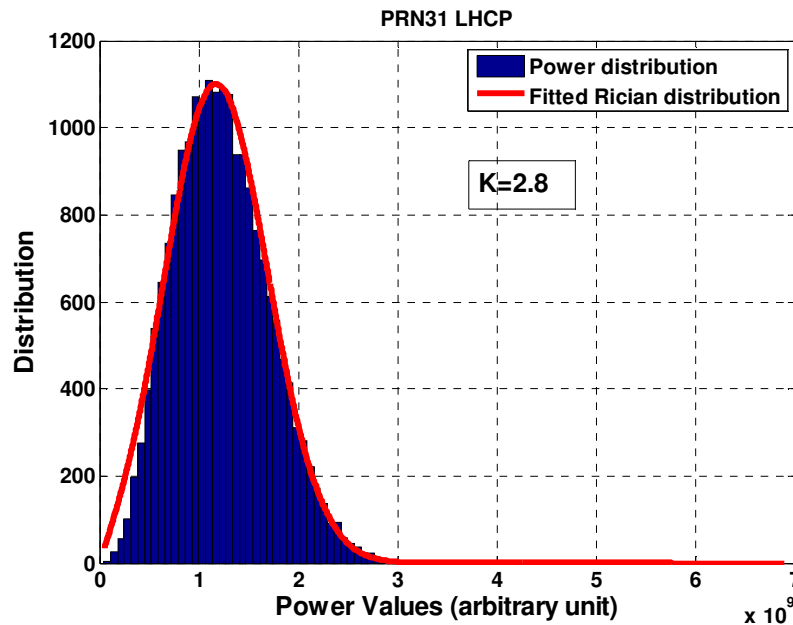


Figure 5.11: PRN 31 power distribution and its corresponding Rician distribution for LHCP antenna

5.2.2.2 PRN 14 RHCP/LHCP power distributions

Figures 5.12 and 5.13 show the RHCP and LHCP power distributions for PRN 14. Their K factors are also estimated through the distribution fitting technique. As expected, the RHCP K factor ($K_{RHCP} = 8.7$ dB) is higher than the LHCP K factor ($K_{LHCP} = -15.4$ dB), which indicates that the signal received by the LHCP antenna was subjected to a higher amount of multipath signals compared to the signal received by the RHCP antenna. The RHCP and LHCP K factors for both satellites are shown in Table 5.1. Both RHCP and LHCP K factors are higher for PRN 31. The signal from PRN 14 is subjected to more multipath reflection than that from PRN 31. Therefore, more multipath power is added to the PRN 14 signal power, and the K factor is lower for this satellite.

Table 5.1: RHCP and LHCP K factor for PRN 14 and 31

PRN	RHCP antenna	LHCP antenna
14	8.7 dB	-15.4 dB
31	12.2 dB	2.8 dB

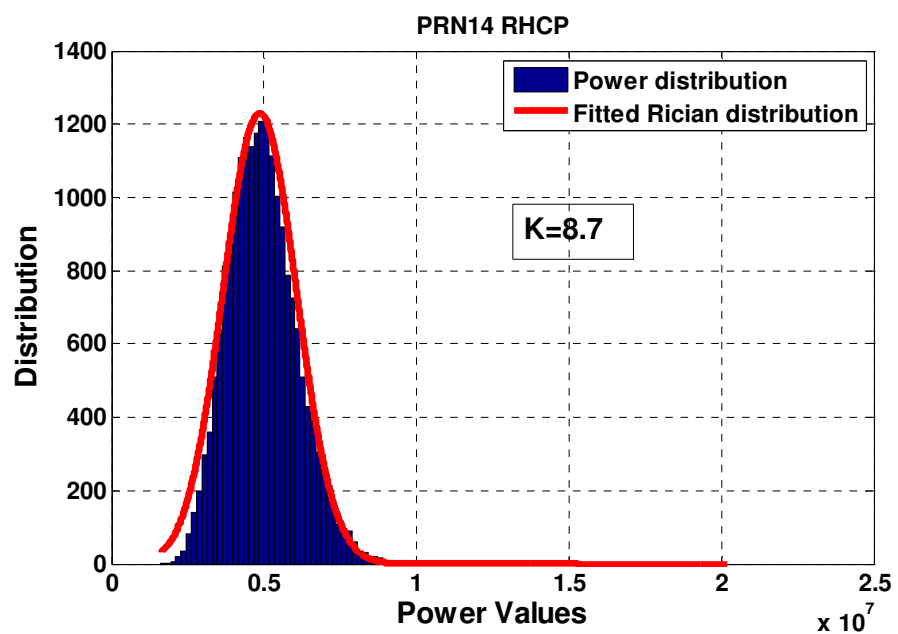


Figure 5.12: PRN 14 power distribution and corresponding Rician distribution for RHCP antenna

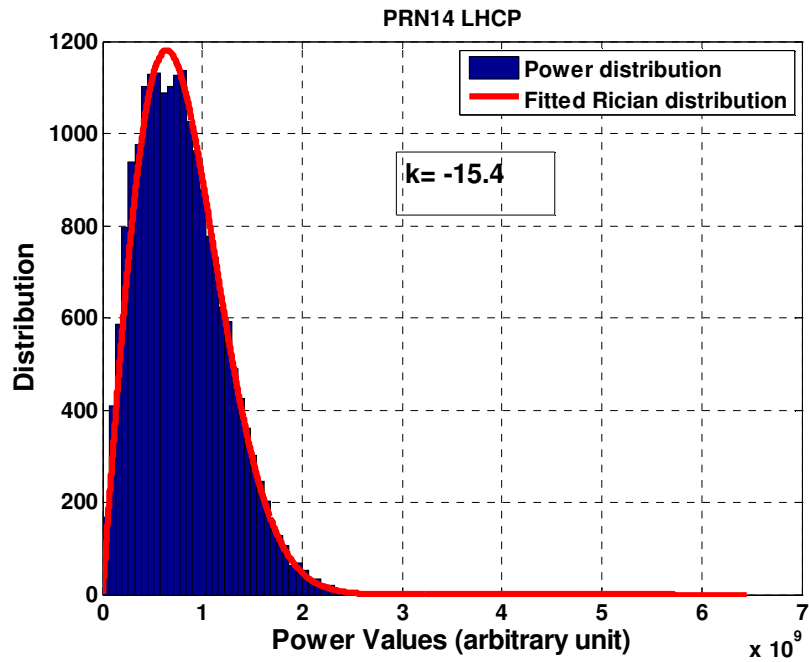


Figure 5.13: PRN 14 power distribution and corresponding Rician distribution for LHCP antenna

5.3 Pseudorange multipath

As has already been observed from the SMR values, autocorrelation functions and K factor analysis, the signal received by the LHCP antenna has absorbed more multipath power compared to the signal from the RHCP antenna. PRN 14 has also been subjected to more multipath power reception compared to the PRN 31. Consequently, more multipath error should have been introduced in the signals with higher level of multipath power reception. Figures 5.14 and 5.15 show that the signal from the LHCP antenna has higher pseudorange multipath errors than the signal received by the RHCP antenna.

As can be seen in Figure 5.16, PRN 14 pseudoranges have higher multipath errors than those of PRN 31. The RHCP and LHCP pseudorange multipath errors for PRN 14 and 31 are also compared in Tables 5.2 and 5.3, which show the mean and maximum values for these pseudorange multipath errors, respectively.

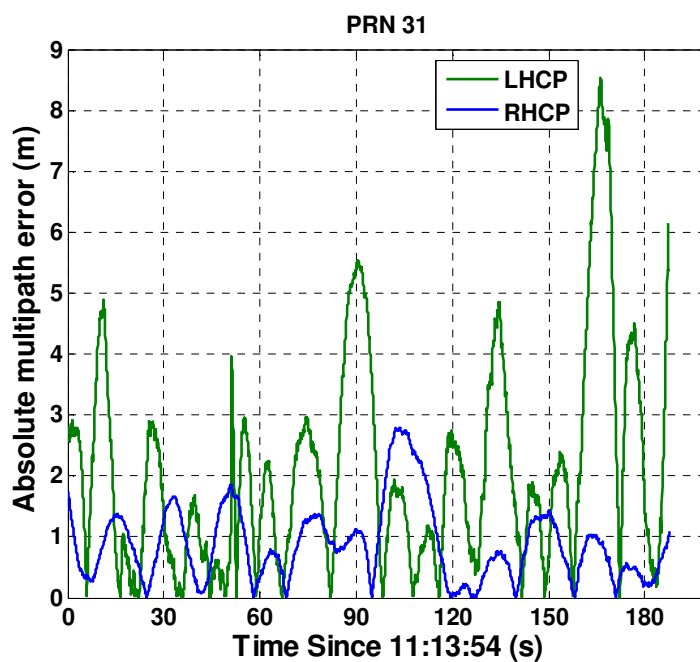


Figure 5.14: PRN 31 multipath errors for RHCP and LHCP antennas

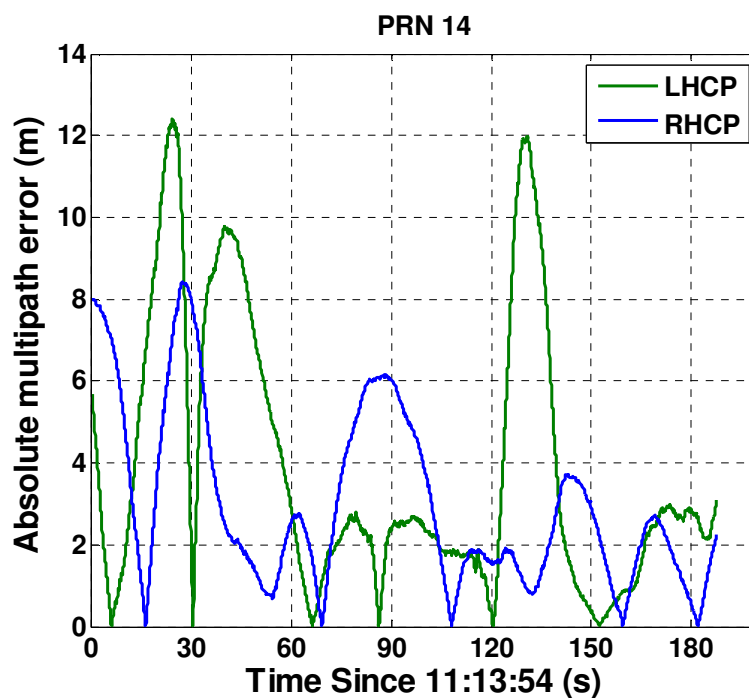


Figure 5.15: PRN 14 multipath errors for RHCP and LHCP antennas

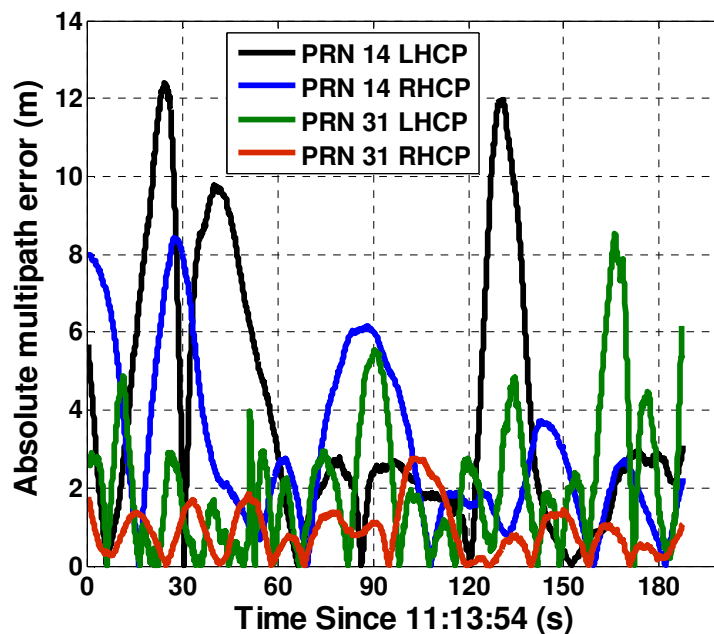


Figure 5.16: PRN 14 and PRN 31 absolute multipath error values for the RHCP and LHCP antenna

Table 5.2: RHCP/LHCP absolute maximum multipath errors for PRN 14 and 31

PRN	Maximum Multipath Error (m)	
	RHCP antenna	LHCP antenna
14	8.44	12.40
31	2.78	8.54

Table 5.3: RHCP and LHCP mean absolute multipath errors (m) for PRN 14 and 31

PRN	Mean Absolute Error (m)	
	RHCP antenna	LHCP antenna
14	2.98	3.84
31	0.88	2.06

5.4 U-blox receiver analyses

This section investigates antenna polarization effects on position domain results as measured by the U-blox receivers. The RHCP and LHCP signals received by the commercial U-blox receivers are further processed by the PLAN group's positioning software C³NAVIG²™ (Petovello et al 2000) in order to obtain the position solutions for both signals. Satellite geometry, C/N₀ values, position solution results as well as DOP values are compared for both RHCP and LHCP signals. The observation interval started at 10:28 on June 20th 2008 and finished at 11:20 the same day. The test was performed near the ICT building in the same place as the previous one.

Figures 5.17 and 5.18 show the GPS satellite geometry observed by the RHCP and LHCP antennas obtained from the U-blox receivers. They show satellites in view at the end of the observation time. They also show the satellite geometry change during the 52 minutes of observations. Satellites shown in red have had weak signal reception and were not tracked by the receivers. Satellites in blue have had higher C/N_0 level and have been partially tracked by the receivers. Since they introduced large pseudorange errors in the position solution, they were not used in computing the position solution. Only the satellites in green have been used in the generation of the position results.

As mentioned before, satellites in the east and west directions at low elevations, such as PRNs 11, 12, 5, 20 and 30, were subjected to multiple blockages and reflections by the ICT and Earth science buildings. This introduces a large amount of multipath power in the received composite signals.

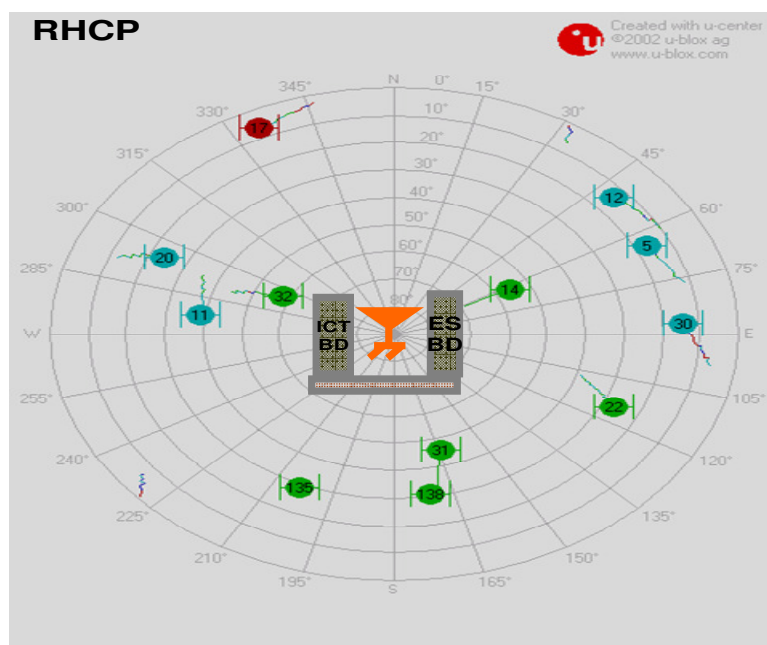


Figure 5.17: GPS satellite geometry observed by the RHCP antenna

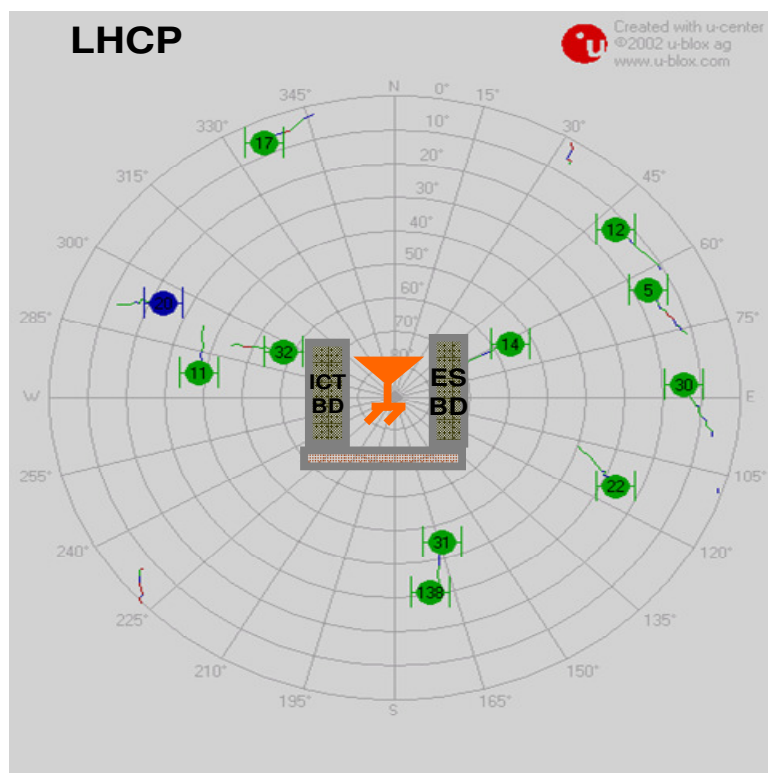


Figure 5.18: GPS satellite geometry observed by the LHCP antenna

Figures 5.19 to 5.21 show the C/N_0 levels measured by the RHCP and LHCP U-blox receivers for high and low elevation satellites in view. As can be seen in Figure 5.19, signals from PRN 12 received by the LHCP antenna have higher C/N_0 levels at some epochs than the corresponding signals received by the RHCP antenna.

As was mentioned before in Chapter 2, the total received signal by the RHCP and LHCP antennas can be written as

$$\begin{aligned}
 \text{Received}^R &= \beta(\theta_{LOS}) \times \text{LOS} + \text{MP}^R = \beta(\theta_{LOS}) \times \text{LOS} + \beta(\theta_{MP}) \times \text{MP}_{\text{RHCP}} + \varepsilon(\theta_{MP}) \times \text{MP}_{\text{LHCP}} \\
 &\approx \beta(\theta_{LOS}) \times \text{LOS} + \beta(\theta_{MP}) \times \text{MP}_{\text{RHCP}} \\
 \text{Received}^L &= \varepsilon(\theta_{LOS}) \times \text{LOS} + \text{MP}^L = \varepsilon(\theta_{LOS}) \times \text{LOS} + \varepsilon(\theta_{MP}) \times \text{MP}_{\text{RHCP}} + \beta(\theta_{MP}) \times \text{MP}_{\text{LHCP}} \\
 &\approx \varepsilon(\theta_{LOS}) \times \text{LOS} + \beta(\theta_{MP}) \times \text{MP}_{\text{LHCP}}
 \end{aligned} \tag{5.7}$$

This equation explains why RHCP and LHCP receiver's performance is different for low elevation satellites such as PRN 12. The LHCP antenna's gain for the LOS signal $\{\varepsilon(\theta_{LOS})\}$ is significantly smaller than RHCP power gain $\{\beta(\theta_{LOS})\}$, but the received signal power seems to be higher for the LHCP antenna. Therefore, it can be concluded that multipath power is the major part in the total composite signal power received by the LHCP antenna. The multipath power received by the LHCP antenna (MP^L) is also higher than the multipath power received by the RHCP antenna (MP^R). The dominant multipath component in the LHCP and RHCP antenna are $\{\beta(\theta_{MP}) \times \text{MP}_{\text{LHCP}}\}$ and $\{\beta(\theta_{MP}) \times \text{MP}_{\text{RHCP}}\}$ respectively. As can be concluded, the LHCP multipath component's power (MP_{LHCP}) is higher than that of the RHCP multipath (MP_{RHCP}) in the received elliptically polarized multipath signal for these satellites.

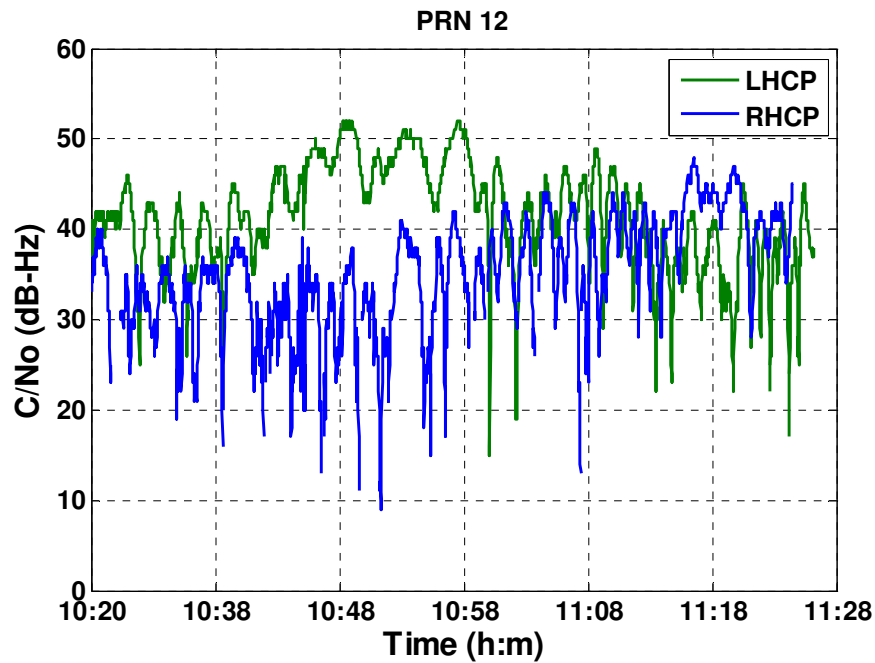


Figure 5.19: RHCP and LHCP C/No levels for PRN 12

Satellites at higher elevations have better LOS visibility. Their corresponding signals can be received by the antenna in direct as well as indirect paths. For example, PRN 32's elevation was 45° at the start of the observation period and it reached 60° at the end of the observation interval. At the start of the observation interval, the C/N_0 level for the LHCP antenna was higher than its corresponding value for the RHCP antenna since PRN 32 was at an elevation at which significant multipath was added to the received signal. As the elevation is increased, PRN 32 had better LOS visibility, which in turn caused the LOS power to have a greater contribution in the total received power. Since the LHCP antenna's gain for the LOS power reception $\{ \epsilon(\theta_{Los}) \}$ is lower than the RHCP antenna's gain $\{ \beta(\theta_{Los}) \}$, the C/N_0 level started to increase in the RHCP antenna and decrease in the LHCP antenna as the elevation increased.

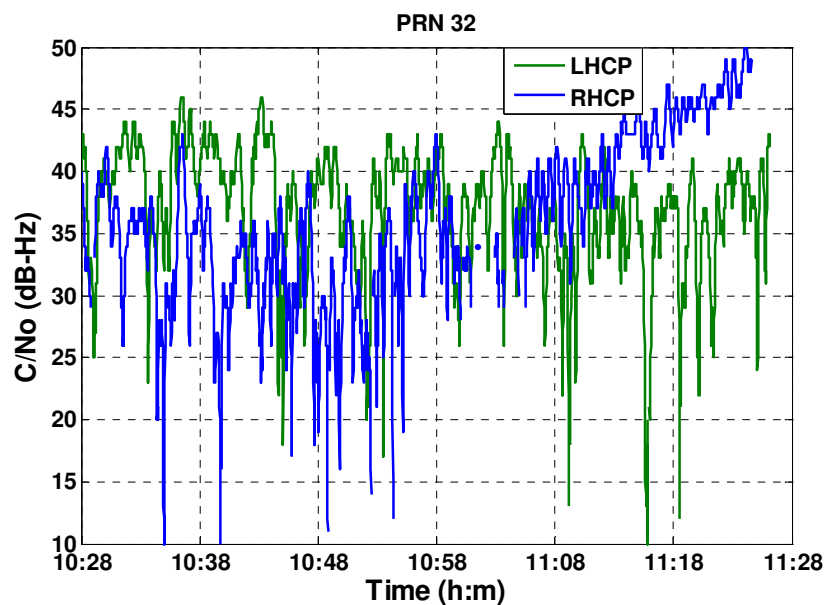


Figure 5.20: RHCP and LHCP C/No levels for PRN 32

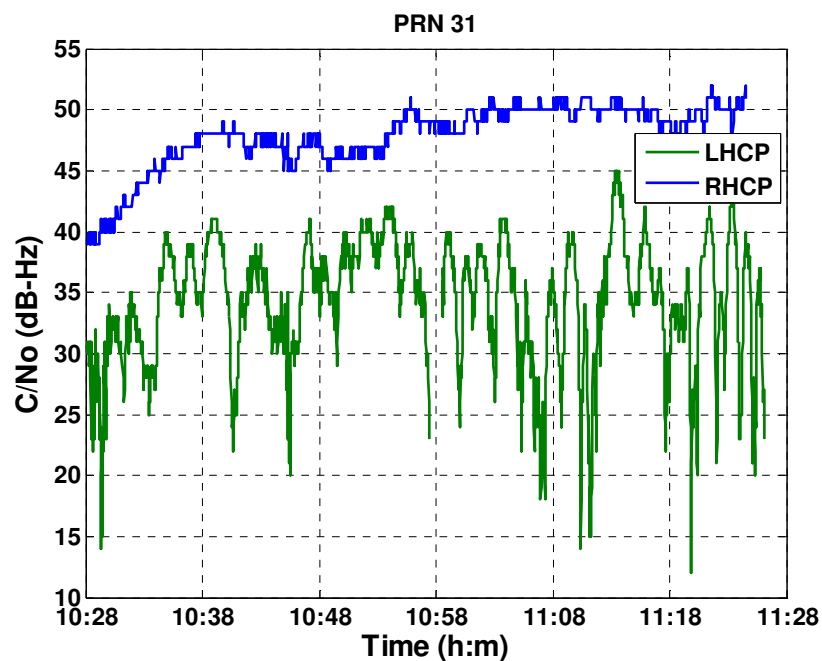


Figure 5.21: RHCP and LHCP C/No levels for PRN 31

For PRN 31, on the other hand, the C/N₀ level is significantly higher in the RHCP antenna than the LHCP antenna (Figure 5.21). Deep fading can be seen in the LHCP

C/N_0 while the RHCP C/N_0 has not undergone any deep fading during the entire observation interval. It shows that the LHCP antenna absorbs much higher multipath power than the RHCP for the high elevation satellites (PRNs 14 and 31).

5.4.1 Position solutions for the RHCP and LHCP antennas

In this sub-section, post-processing of the U-blox receivers' outputs will be discussed. Pseudorange measurements and ephemeris data obtained from RHCP and LHCP U-blox receivers are used as the raw data in the C³NAV^{G2}TM software. C³NAV^{G2}TM was run in differential mode in order to generate position solutions for both RHCP and LHCP receivers. The reference station was at a pre-surveyed point on the CCIT building's roof. The test point was selected as the remote station.

5.4.1.1 RHCP and LHCP DOP values

GDOP values for the RHCP and LHCP antennas were estimated by C³NAV^{G2}TM. As can be seen in Figure 5.22, the LHCP and RHCP antennas give nearly the same DOP (nearly same constellation and satellites to track) and occasionally the LHCP has even exhibited better DOP, particularly when there are low elevation satellites in sky. The RHCP mean DOP value ($\overline{\text{GDOP}}_{\text{RHCP}} = 1.92$) is higher than the corresponding parameter for the LHCP antenna ($\overline{\text{GDOP}}_{\text{LHCP}} = 1.85$), which shows that LHCP antenna has experienced, on average, a better satellite geometry.

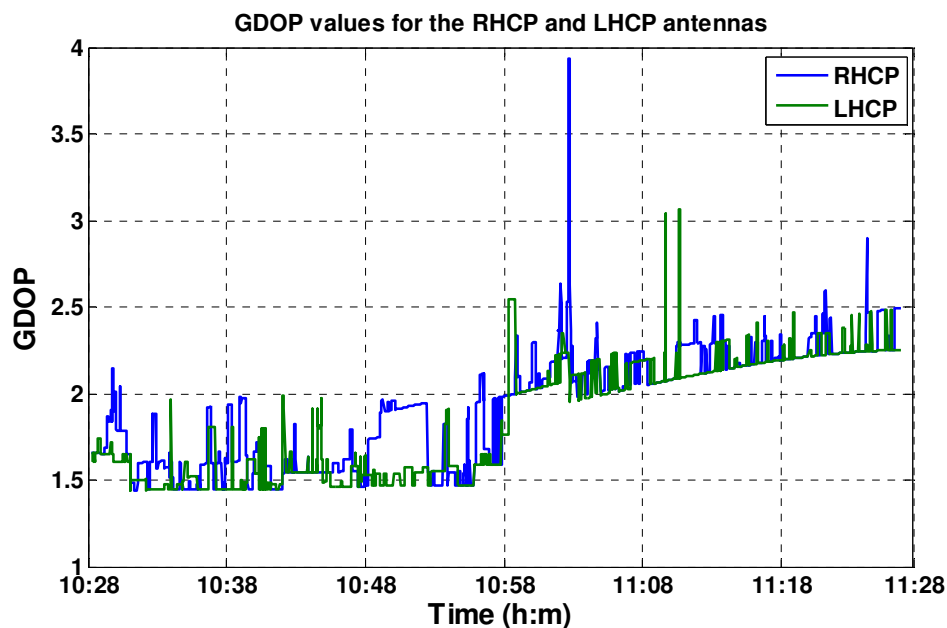


Figure 5.22: DOP values for the RHCP and LHCP antennas

5.4.1.2 RHCP and LHCP position solutions

Horizontal position errors for the RHCP and LHCP antennas are plotted in Figure 5.23 and 5.24, respectively. The RHCP horizontal RMS error is 29.1 m while the LHCP's corresponding value is 31.4 m. Table 5.4 compares the RHCP and LHCP position RMS errors for the easting, northing and vertical directions. The LHCP antenna has a lower DOP (better satellite geometry) but higher northing, easting and vertical errors due to the reasons discussed above.

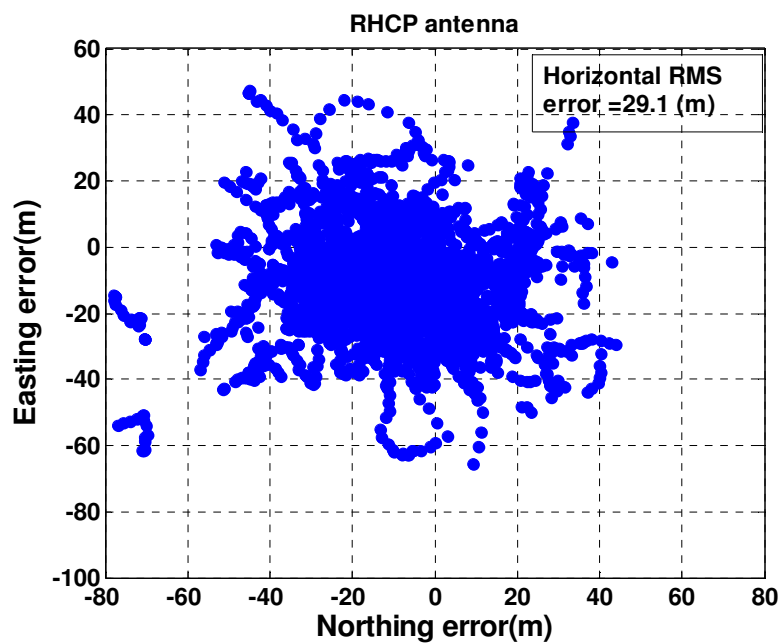


Figure 5.23: RHCP antenna horizontal position errors

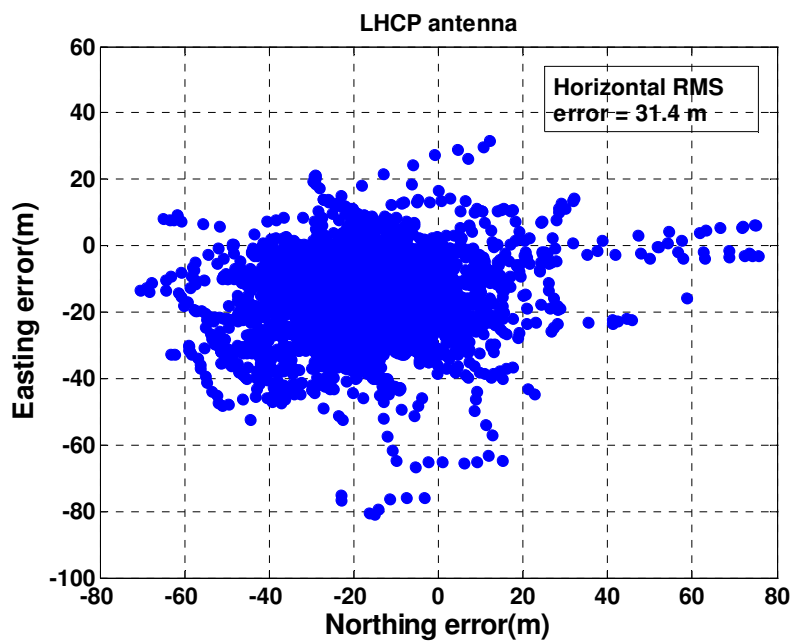


Figure 5.24: LHCP antenna horizontal position errors

Table 5.4: RMS position errors for the RHCP and LHCP antennas

RMS position errors (m)		
	RHCP	LHCP
Northing	22.1	24.2
Easting	18.9	20.1
Vertical	40.2	54.9
3D	49.6	63.3

High sensitivity U-blox receivers with specific tracking technology were used in this test. Their tracking sensitivity in terms of SNR is -160 dBm as specified in the U-blox data sheet (U-blox 2008) and 12 dB-Hz in terms of C/N_0 as was practically verified in a static mode test (Kazemi & O'Driscoll2008). Therefore, they can track signals even if these are corrupted by high level of multipath fading. As was previously discussed, the LHCP antenna receives more multipath power than the RHCP antenna. Since the signals were subjected to high level of multipath fading in this scenario, this multipath power is constructively added to the received power during some portions of the observation time. As was shown in Section 5.4.1, the LHCP C/N_0 level is higher than the RHCP C/N_0 level for low elevation satellites in some periods, which aids the LHCP U-blox receiver to track the signals in the intervals when the RHCP C/N_0 level is below the U-blox tracking sensitivity. However, this improved satellite geometry has not provided a better position solution for the LHCP antenna since there are more multipath errors introduced in the LHCP antenna's pseudorange measurements (Section 5.3). More multipath power is also

rejected in the RHCP antenna because most of the multipath signal is left hand circularly polarized (Section 5.4.1). As a result, the LHCP antenna's position errors are higher than the RHCP corresponding values.

5.5 Summary

All the aforementioned methods in this chapter have been used in order to investigate the effects of different multipath conditions, and antenna's polarization in different signals' characteristics. Chapter 6 provides the conclusions related to the results obtained in this thesis and discusses recommendations for future work.

Chapter Six: Conclusions and Recommendations

6.1 Conclusions

In this research, a Kalman filter approach for multipath parameter estimation (KMP algorithm) was introduced and described in detail. The proposed algorithm was then tested with live GPS data in a real multipath environment and also multipath data collected from an advanced GPS hardware simulator in a more controlled condition. The simulated scenarios investigated KMP performance under different SMR values and multipath relative code delays. The KMP technique resolved multipath components spaced 0.2 and 0.5 chips relative to the LOS component. The RMS error of the technique, which is an effective measure of its performance, is higher in the case where the multipath signal is spaced closer to the LOS component. As expected, the closer multipath signal has more correlated characteristics with the LOS signal and is harder to estimate. The KMP technique also resolved multipath components spaced 0.2 chips with SMR values as high as 12dB. It shows limitations in resolving multipath components with higher SMR values. Multipath signals with an SMR of 20 dB or higher is not resolvable by the KMP technique and is estimated as part of the LOS component. However, the effect of multipath in the positioning domain is a function of many parameters, including the SMR. For large SMR values, multipath effects are typically small.

A specific field experiment involving real data and that included a dual polarized RHCP/LHCP antenna was also designed and carried out for characterizing and analyzing the multipath environment. SMR values obtained from the KMP algorithm, fading patterns, K factors estimated from the signal envelopes and pseudorange multipath errors were measured and estimated for the signals received by both RHCP and LHCP antennas. These multipath parameters extracted from these two data sets were then used for studying the effect of antenna polarization on the level of multipath power absorption in the received signal. The line of sight (LOS), RHCP multipath (MP_{RHCP}) and LHCP multipath (MP_{LHCP}) components were shown to be three common power components in the RHCP and LHCP antennas, but they contribute with different weights to the total received power for the RHCP and LHCP antennas. It was concluded that the LHCP antenna received more multipath power than the RHCP antenna while attenuating the LOS power. This phenomenon was theoretically described in Chapter 2 and practically observed through different multipath parameterization factors shown in Chapters 4 and 5. Power distributions for the signals received by the LHCP antenna have lower K factors than those for the signals received by the RHCP antenna. Similarly, LHCP autocorrelation functions are more corrupted from their ideal patterns than RHCP autocorrelation functions. Consequently, pseudorange multipath errors for the LHCP signals are higher than the corresponding values for the RHCP signals.

For scenarios wherein signals are received following multiple reflections and the LOS signal has undergone some blockage, multipath power is the dominant component in the total received power. The LHCP antenna absorbs more multipath power compared to the

RHCP antenna. Therefore, LHCP C/N_0 can be higher at some epochs than its corresponding value for the RHCP antenna, but more multipath errors are also introduced. In an urban multipath environment, satellites at low elevations are normally subjected to more LOS signal blockage and reflections than high elevation satellites. Hence, high levels of multipath power reception are expected for the low elevation satellites in such environments. For signals received by the antenna with small multipath reflections, multipath power has a negligible contribution to the total received power. Since the LHCP antenna receives the LOS power with a lower gain than the RHCP antenna, its C/N_0 is lower than the corresponding RHCP antenna value in these cases. In an urban multipath environment, satellites at high elevations are normally subjected to negligible LOS signal blockages and reflections. Therefore, the RHCP antenna has a better visibility than the LHCP antenna for the satellites with very high SMRs (negligible level of multipath power reception), and small multipath errors are also introduced in the RHCP's range measurements for these satellites.

In a harsh multipath environment where most signals are subjected to multipath reflections, an LHCP antenna can have better visibility to low elevation satellites (higher C/N_0 but also more faded patterns) during some portions of the observation time. The range measurements obtained using a LHCP antenna are noisier than those obtained with a RHCP antenna. This is equivalent to a better (lower) LHCP DOP (due to greater satellite visibility) but also a higher LHCP UERE (User Equivalent Range Error). Therefore, the LHCP position solution may be more erroneous than the corresponding

RHCP solution. Using an LHCP antenna beside the RHCP antenna can also be helpful to monitor and estimate the instantaneous multipath power level.

6.2 Recommendations for future work

Further research on the KMP technique is required for modeling real environments. A more realistic design may model more extra paths depending on the multipath channel characteristics. Three major issues would be introduced by modeling more extra paths. First, more states would be added to the Kalman state vector, thereby increasing the chance of filter divergence and the computational load. Secondly, an effective technique should be selected in order to determine the correct number of paths and also initialize these extra paths with reasonably accurate amplitude and relative code delay estimates. Thirdly, having additional extra paths would make the separation of the LOS and multipath states more difficult to achieve. Since closely-spaced multipath signal components are highly correlated with the LOS signal components, a more precise multipath modeling which takes into account all the aforementioned issues could be helpful in separating LOS and multipath powers more effectively from each other. For stationary reflector-receiver cases, the fading bandwidth is usually much smaller than 1 Hz and the Doppler difference between the multipath and LOS signals can be absorbed in the multipath phases. In dynamic reflector-receiver scenarios, the fading bandwidth can be considerably higher than 1 Hz and the Doppler difference between multipath and the LOS signal cannot be absorbed in the multipath phases. A more realistic model, especially in dynamic scenarios, would assign an extra state as the Doppler frequency for each path.

The primary-secondary structure proposed herein would use both RHCP and LHCP data and process them simultaneously. The LHCP loop is an open loop which means the LHCP loop does not contain LHCP code and carrier phase estimators. Further research could be performed on the design of a new structure that processes both RHCP and LHCP data simultaneously but in two closed loops. Similar to the primary-secondary structure, some tracking information from one loop could be fed to the other loop. Since the multipath power is higher in the LHCP antenna, multipath power estimation in the LHCP loop might result in more precise results. Therefore, the multipath components estimated from the LHCP tracking loop could then be used in the RHCP loop after LHCP multipath components are correctly converted into RHCP multipath components. There would be major issues for the implementation and performance of this structure. Firstly, the KMP technique is based on the multipath scenarios where the LOS power is the dominant power component in the received signal, which may not be the case for the signal received by the LHCP antenna. Secondly, the parameters to be used in order to convert the multipath components from the LHCP into the RHCP loop are unknown. Estimating these parameters would require extensive multipath environment analysis such as estimating the angle of arrival for the LOS and multipath signals, measuring the reflection coefficients of the reflectors and RHCP/LHCP power patterns.

References

Beaulieu, N.C., A.S. Toms and D.R. Pauluzzi (2000) Comparison of Four SNR Estimators for QPSK Modulations, IEEE Communications Letters, vol.4, pp. 43-45.

Braasch, M.S. (2001) Performance Comparison of Multipath Mitigating Receiver Architectures, IEEE Aerospace Conference, pp. 672-678.

Braasch, M. S. (1996) GPS Multipath Model Validation, Proceedings of the IEEE Position Location and Navigation Symposium, pp. 672-678.

Brown, R.G. and P.Y.C. Hwang (1992) Introduction to Ransom Signals and Applied Kalman Filtering, John Wiley & Sons, Inc., USA.

Cheng, D. (1993) Fundamentals of Engineering: Electromagnetics, Addison-Wesley series in Electrical Engineering, Toronto ON, pp. 154-167.

Cheng, D. (1983) Field and Wave Electromagnetic, Addison-Wesley series in Electrical Engineering, Toronto ON, pp. 230-245.

De Souza, E.M. (2004) Multipath Reduction from GPS Double Differences using Wavelets: How far can we go?, Proceedings of the ION GNSS 2004 (Long Beach, September 21-24), The Institute of Navigation, 8pages.

Dovis, F., M. Pini and P. Mulassano (2004) Turbo DLL: an Innovative Architecture for Multipath Mitigation in GNSS receivers, Proceedings of ION GNSS 2004 (Long Beach, Sept 21), U.S. Institute of Navigation, 12 pages.

Fishler, E. and B.Z. Bobrovsky (1999) Anti-multipath cellular radio location for DS/CDMA systems using a novel EKF sub-chip RAKE tracking loop, Proceedings of IEEE Military Communications Conf. (MILCOM), vol. 2, 1999, pp. 1328–1332.

Fenton, P., B. Falkenberg, T. Ford and A.J. Van Dierendonck (1991) NovAtel's GPS Receiver - the High Performance OEM Sensor of the Future, Proceedings of ION GPS'91 (Albuquerque, Sept 9), U.S. Institute of Navigation, 7 pages.

Grewal, M. S. and A.P. Andrews (2001) Kalman Filtering: Theory and Practice Using MATLAB 2nd Edition, Prentice-Hall.

Heinrichs, G. (2002) Using of RAKE Receiver Architecture for Combining GNSS and CDMA Cellular Wireless Location, Proceedings of IEEE Symposium on Spread-Spectrum Tech., vol. 3, pp. 787-791.

Ibrahim, B.B. and A.H. Aghvami (1994) A PN Code Tracking System for Direct Sequence Spread Spectrum Operation in a Frequency Selective Fading Environment, IEEE, 5 pages.

Izadpanah, A., C. O'Driscoll and G. Lachapelle (2008) GPS Multipath Parameterization using the Extended Kalman Filter and a Dual LHCP/RHCP Antenna, Proceedings of GNSS08 (Savannah, 16-19 Sep., Session C2), U.S. Institute of Navigation, 11 pages.

Iltis, R.A. (1994) An EKF-Based Joint Estimator for Interference, multipath, and Code Delay in a DS Spread-Spectrum Receiver, IEEE Transactions on Communications, Volume 42, Issue 234, Part 2, pp. 1288-1299.

Iltis, R.A. (1991) A Digital DS Spread-Spectrum Receiver with joint Channel and Doppler shift Estimation, IEEE Transactions on Communications, vol. 39, pp. 1255-1266.

Iltis, R.A. (1990) Joint estimation of PN code delay and multipath using the extended Kalman filter, IEEE Transactions on Communications, vol. 38, pp. 1677-1685.

Irsigler, M. and B. Eissfeller (2003) Comparison of Multipath Mitigation Techniques with Consideration of Future Signal Structures, Proceedings of ION/GNSS 2003, U.S. Institute of Navigation, 8 pages.

Jee, G.I., H.S. Kim, Y.J. Lee and C.G. Park (2002) A GPS C/A Code Tracking Loop Based on Extended Kalman Filter with Multipath Mitigation, Proceedings of ION GPS 2002 technical national(San Diego, January28-30), U.S. Institute of Navigation, 9 pages.

Kaplan, E.D. (2006) Understanding GPS: Principles and Applications, Ashtech House Publishers, Norwood.

Kazemi, P.L. and C. O'Driscoll (2008) Comparison of Assisted and Stand-Alone Methods for Increasing Coherent Integration Time for Weak GPS Signal Tracking, Proceedings of GNSS08 (Savannah, 16-19 Sep., Session C4), U.S. Institute of Navigation, 11 pages.

Kim, E., T. Walter and J.D. Powell (2007) Adaptive Carrier Smoothing Using Code and Carrier Divergence, Proceedings of the 2007 National Technical Meeting (San Diego, January 22 - 24), U.S. Institute of Navigation, 9 pages.

Lachapelle G. (2007) Advanced GNSS Theory and Application, ENGO 625 lecture notes, fall 2007.

Lakhzouri, A., E.S. Lohan, R. Hamila and M. Renfors (2003) Extended Kalman Filter Channel Estimation for Line-of-Sight Detection in WCDMA Mobile Positioning, EURASIP Journal on Applied Signal Processing 2003, vol 13, pp. 1268–1278.

Lakhzouri, A., E.S. Lohan, and M. Renfors (2004) Estimation of Closely-spaced paths via Particle Filters for WCDMA, IEEE Transactions on Control, Communications and Signal Processing, pp. 791-794.

Laxton, M.C. and S.L. De Vilbiss (1996) GPS Multipath Mitigation during Code Tracking, Proceedings of the American Control Conference (New Mexico, June 1977), 7 pages.

MacGougan, G.D. (2003) High Sensitivity GPS Performance Analysis in Degraded Signal Environments, M.Sc. Thesis, Department of Geomatics Engineering, University of Calgary, Canada, Published as UCGE Report No. 20176 (Available at <http://plan.geomatics.ucalgary.ca>).

Mattos, P. (1996) Multipath Elimination for the Low-Cost Consumer GPS, Proceedings of ION GPS-96 (Kansas City, September 17-20) U.S. Institute of Navigation, 11 pages.

Manandhar, D., R. Shibasaki, and H. Torimoto (2006a) GPS Reflected Signal Analysis using Software Receiver, Journal of Global Positioning Systems, Vol. 5, No. 1-2:29-34.

Manandhar D., R. Shibasaki and H. Torimoto (2006b) Prototype Software-based Receiver for Remote Sensing Using Reflected GPS Signals, Proceedings of GNSS06 (Fort Worth, 26-29 September), U.S. Institute of Navigation, 13 pages.

Manandhar, D., R. Shibasaki and P. L. Normark (2004) GPS Signal Analysis using LHCP/RHCP Antenna and Software GPS Receiver, Proceedings of ION GPS/GNSS 2004 (Long Beach, September 21-24), U.S. Institute of Navigation, 13 pages.

Manandhar, D. and R. Shibasaki (2003) Prototype Software-based GPS Receiver for Reflected Signal Analysis, IEEE International Geoscience and Remote Sensing Symposium, IGARSS 2005, Seoul, Korea, 10 pages.

Nee, V. (1992) The Multipath Estimating Delay Lock Loop, IEEE Second International Symposium on Spread Spectrum Techniques and Applications, Yokohama, Japan, November 29 - Dec 02, 4pages.

Petovello, M.G., M.E. Cannon, and G. Lachapelle (2000) C3NAVG2™ Operating Manual, Department of Geomatics Engineering, University of Calgary, 31 pages.

Petovello, M., and G. Lachapelle (2006) Comparison of Vector-Based Software Receiver Implementations with Application to Ultra-Tight GPS/INS Integration, Proceedings of GNSS06 (Forth Worth, 26-29 Sep, Session C4), U.S. Institute of Navigation, 10 pages.

Petovello, M.G., C. O'Driscoll, G. Lachapelle, D. Borio and H. Murtaza (2008) Architecture and Benefits of an Advanced GNSS Software Receiver, Proceedings of International Symposium on GPS/GNSS 2008, Tokyo, Japan, 11 pages.

Psiaki, M.L., and H. Jung (2002) Extended Kalman Filter Methods for Tracking Weak GPS Signals, Proceedings of ION GPS 2002, U.S. Institute of Navigation, 15 pages.

Psiaki, M.L. (2001) Smoother-Based GPS Signal Tracking in a Software Receiver, Proceedings of ION GPS 2001, U.S. Institute of Navigation, 13 pages.

Spirent (2006), Signal Generator Hardware User Manual, Spirent Communications.

U-blox, ANTARIS4 Modules SIM, Last modified in January 2008. (http://www.u-blox.com/customersupport/antaris4_doc.html)

Van Nee R (1993) Spread-spectrum code and carrier synchronization errors caused by multipath, IEEE Transactions in Aerospace and Electronic Systems , vol 29, pp. 1359-1366.

Ward, P.W., J.W. Betz and C.J. Hegarty (2006) Understanding GPS Principles and Applications, Artech House, Inc., pp. 153-241.

Wikipedia Polarization, (<http://en.wikipedia.org/wiki/Polarization>), Last accessed June 2008

Yang, C. and A. Porter (2005a) Frequency-Domain Characterization of GPS Multipath for Estimation and Mitigation, Proceedings of ION GNSS 2005 (San Diego, January 24-26), U.S. Institute of Navigation, 12 pages.

Yang C., A. Porter (2005b) Frequency GPS Multipath Estimation and Mitigation via Polarization Sensing Diversity: Parallel Iterative Cross Cancellation, Proceedings of ION GNSS 2005 (San Diego, January 24-26), U.S. Institute of Navigation, 9 pages.